Development of a Decision Support System for the Design and Adjustment of Sailboat Rigging

I. Ortigosa
J. Espinosa

Monograph CIMNE Nº-126, February 2012

Development of a Decision Support System for the Design and Adjustment of Sailboat Rigging

I. Ortigosa
J. Espinosa

Monograph CIMNE Nº-126, February 2012

International Center for Numerical Methods in Engineering
Gran Capitán s/n, 08034 Barcelona, Spain

INTERNATIONAL CENTER FOR NUMERICAL METHODS IN ENGINEERING
Edificio C1, Campus Norte UPC
Gran Capitán s/n
08034 Barcelona, Spain
www.cimne.upc.es

First edition: February 2012

DEVELOPMENT OF A DECISION SUPPORT SYSTEM FOR THE DESIGN AND ADJUSTMENT OF SAILBOAT RIGGING
Monograph CIMNE M126

ISBN: 978-84-939640-2-3

Depósito legal: B-6547-2012

“The most incomprehensible thing about the world is that it is at all comprehensible”

Albert Einstein (1879-1955)

AGRADECIMIENTOS

A la primera persona que debo agradecer esta tesis es a Alejandro Rodríguez de Torres, que fue el primero en animarme a iniciar esta singladura. Alejandro y Daniel Yebra fueron los que pusieron la primera piedra para que yo pudiera estar hoy dónde estoy, muchas gracias a los dos.
A Julio García, mi director, primero por aceptar ser mi director y segundo por toda su ayuda y comprensión. De él he aprendido muchas cosas, a nivel académico y a nivel personal, porque es un gran investigador, pero es mejor persona todavía. Muchas gracias Julio.
A todas las personas de la Facultad de Náutica que me han ayudado, Xavi Martínez de Osés, Antoni Isalgué, Mireia Sala, Montse Margalef y en especial a Marcel·la Castells. Cuando empecé el doctorado ella fue mi compañera y mi modelo a seguir. Gràcies pel teu recolçament en tots aquests anys, saps que per mi no ets una companya de feina, ets una amiga. Gràcies Marcel·la!!!
A todos mis compañeros de CIMNE Cruchi, Jordi, Alberto, Hiram, Susana, Pere Andreu y Mari Carmen. En especial a Roberto López por toda su ayuda desde el principio. Y a Xavi Martinez por su colaboración. A CIMNE, en concreto, a su director Eugenio Oñate por su apoyo.
A Daniel Sá y a Clara García, de Compass.
A todos mis compañeros del NT3, que me acompañan en esas jornadas de trabajo Augusto, Elena, Pablo, Toni, Juan y Esther. A los Water Walkers por esos momentos de desconexión. Y en especial a Borja y Arnel por su ayuda.

A todos mis amigos y amigas que me han acompañado en las etapas buenas y malas de mi vida. En especial a Susana, que ha estado siempre ahí!!!!

A toda mi familia por estar siempre a mi lado. Adri, Pepe, Javi, Antonio, Carmen, Toni, Dani y Jordi. A mis tíos Juaqui y Jordi por 'adoptarme' tantas veces. A mi prima Lorena, por todo lo vivido. A mi abuelo Adrián y a mi abuela Pepa, que ya no está. Su pregunta siempre era "Querida, ¿Cuándo vas a dejar de estudiar?" y mi respuesta " Yaya, yo no voy a dejar de estudiar nunca, ese va a ser mi trabajo!!!". Nunca lo entendió, y la verdad es que yo a veces, tampoco lo entendía. Pero si hoy estoy aquí es gracias a ellos!!

A mi padre por darme la paciencia y a mi madre por darme ese espíritu de lucha. A los dos, porque sois buenos, generosos, trabajadores, justos, sinceros, porque me lo habéis dado todo, en especial todo vuestro amor.
A mi hermano, por enseñarme a ser fuerte. Sin ti no hubiera podido continuar!!!!
Y a la persona que hace que salga el sol cada día en mi vida, Javi.

FIGURE LIST

TABLE LIST

INDEX

1 Introduction

Sailing is the art of controlling a boat with large foils called sails(Wik). A sailor manages the force of the wind on the sails, by adjusting the rigging, in order to control the direction and the speed of the boat. Sailing yachts operate in different wind flow conditions, with wind speed commonly in the range from zero to 20 m/s. Yacht can sail in different headings to true wind velocity and, this true wind velocity is also subjected to changes in atmospheric conditions. Hence, yacht sails have to be adjusted in order to obtain a better yacht performance or control when sailing.

Sails are foils that work by using the airflow set-up by the wind and the motion of the boat. Two or more sails are frequently combined to obtain a smooth flow of air. The performance of a specific sail configuration is obtained by the coupled effect of the airflow set-up around the sails and the response of the structure to the generated forces. The aerodynamic of sails can be divided in three branches: the aerodynamic of upwind sails, reaching sails and running sails. Upwind sails and reaching sails generate lift using the air that flows around them, in the same way as an aircraft wing generates lift. Upwind sails are adopted when sailing at small apparent wind angle (AWA), typically smaller than 35°, where AWA is generally defined as the angle between the yacht course and the undisturbed wind direction at the 10 m reference height above the sea surface. Single mast yachts, namely sloop, adopt a mainsail and a jib or genoa, which are light cambered airfoils designed to work close to the optimum efficiency. The flow is mainly attached and consequently un-viscous code has been adopted with success since sixties to predict aerodynamic global coefficients(Milgram, 1968)(Jackson, 1996). Reaching sails are adopted when sailing at larger AWA, typically from 45 to 160. Sloop modern racing yachts often adopt the mainsail and the asymmetrical spinnaker, which are more cambered airfoils designed to produce the maximum lift, in fact sailing at 90 AWA the lift force component is aligned with the course direction. The flow is attached for more of the half chord of the sail and separation occurs on the trailing edge of the asymmetrical spinnaker. Reaching sail aerodynamics requires the capability to correctly compute the separation edge on the leeward spinnaker surface, hence un-viscous code are not applicable and Navier-Stokes code might be adopted. Running sails are adopted at larger AWA and sloop yachts and generally adopt a mainsail and a symmetrical spinnaker. The flow is mostly separated and sails work as bluff bodies. Separation occurs on the sail perimeters and the drag has to be maximized. In the American's Cup races, the racing curse is around two marks positioned along the wind direction, in such a way that half of the race has to be sailed upwind and half downwind. In this thesis, particular focus has been placed on upwind sails (mainsail and jib or genoa).

The sails are designed and then set to they adopt a shape that will be the most effective in driving the boat. For this purpose, the crew manoeuvre changing the camber, traveller position and sail twist. The fluid-structure interaction of sails and rigging is connected with this manoeuvre of the crew, so it is necessary to consider

all the manoeuvrability variables in the evaluation of a specific sail configuration performance.

Figure 1.1. Sailing Yacht (courtesy of TOTALMAR)

Adjustments to the rigging to achieve the desired amount of camber and sail twist are interrelated. Although the amount of camber is determined in some measure by the cut of the sails, their settings has a significant influence. Mast bend reduces the mainsail camber as the luff curve is matched by the curve of the mast. Mast bend depends directly on the rigging that supports a mast. The mast is mainly held up by wires running fore and aft (stays) or port-starboard (shrouds). The forestay prevents the mast falling backwards and the backstay provides support from the opposite direction, the forestay and backstay stress determine the bending of the mast backwards or forwards. The backstay is an important sail trim control and has a direct effect on the shape of the mainsail. In a masthead rigging, stressing the permanent backstay will directly stress the forestay, particularly for racing, stress is increase in the backstay for sailing upwind, in order to increase forestay stress or bend the mast to improve mainsail shape. Spreaders are used to spread the stressed shrouds to assist in supporting the mast. Above considerations justify the need of considering all the manoeuvre parameters in the evaluation of the sail-rigging behaviour.

The two main objective of this work are:

- To develop a simulation program of the behaviour of upwind sails and rigging, to help the crew to optimize the performance of the sailing yacht in real time. For this purpose, it will be necessary to formulate a fluid-structure interaction algorithm to compute the performance of a particular sail/rigging configuration. Since the crew dynamically trims the rigging and sails, in order to evaluate the performance of the actual configuration, a tool to monitor the rigging and sails will be necessary, too.
- To adjust a monitoring element to quantify in physic values the manoeuvre of the crew. This will be our monitoring tool.

- To reproduce the crew manoeuvre in the simulation program with the data obtained with the monitoring tool. Once the sail/rigging configuration has been adapted 'in real time' to the actual one, the performance of this new configuration can be computed. For this purpose the simulation program and the monitoring tool must communicate among them.

The software to be presented in this thesis, named *Sailing*[1] will be made up of two different inter-connected tools.

- The first will be a Fluid-Structure Interaction (FSI) analysis tool of sails and rigging that is based upon knowledge of the design shape geometry and sail material properties. A structural analysis of the sail and rigging structure and a fluid analysis of the aerodynamic field are combined and iteratively solved to compute the actual flying shape of the sail. For this part, this simulation algorithm integrates two tools: (1) A Fluid Solver (FS), based on the Boundary Element Method (BEM) to calculate the aerodynamic forces for a given sail shape in upwind conditions. (2) A Structural Solver (SS) based on a finite element analysis (FEA) of the structural behaviour of rigging and sails, taking into account the aerodynamic forces and the pre-stresses in the shrouds, stays and sheets given by the sailors. The SS analyses the response of the structure to the aerodynamic forces.
- The second tool will be a flexible sensor network able to monitor different variables of the current rigging configuration. The data obtained by these sensors will be treated to obtain the trim parameters, which will be used as boundary conditions for the previously mentioned FSI tool. The model geometry is adapted as the trim parameters indicate and then the performance of the new configuration can be computed 'in real time'.

The performance analysis will be made for a certain wind condition and a certain structure configuration. If the wind condition changes or the crew changes the structure configuration, a new performance analysis will be made. Due to the difficulties of measuring the boundary conditions with precision dynamically and to reproduce a manoeuvre in real time, only stationary conditions will be analyzed. This is a simplification but admissible, because it can be assumed that at the end of a manoeuvre, the yacht works in a quasi-stationary regime. This final condition will be then analysed in any case as a static problem.

This thesis has been developed within a R+D+i project called DSSAIL[2] partially supported by the 'Ministerio de Industria, Turismo y Comercio'.

The original aspects of this thesis are:

- The communication between the sensors and the FSI algorithm. The sensors capture the trim parameters and these are communicated to the FSI algorithm to adjust the structure to these trim parameters. It is, there is a

[1] A user guide of *Sailing* is presented at Appendage B.
[2] The partners of the project DSSAIL were: Cognit Design, CIMNE, FNB and CompassIS.

consideration 'in real time' of the manoeuvre parameters for the analysis of the fluid structure interaction problem. The trim parameters to be considered are: angle to the wind, foresail sheet's stress and position, mainsail sheet's stress and position and stress at the stays and shrouds.
- The development of a tool to work in real time, which allows establish the coupled behaviour of the flow and the structure.
- The concept of a new kind of wireless and adaptable sensor, suitable to measure the required trim parameters. The concept of quantifying the manoeuvre of the crew is original, since it has not been done before.

The Structural Solver and Fluid Solver had been implemented in C++ and integrated with the pre and postprocessor software GID[3]. The coding of the algorithms didn't start from scratch. *Sailing* was based on a limited implementation previously existing at CIMNE. This basic solver was first revised and validated. The validations proved that its accuracy was quite poor, and it was found that the source code had many bugs. Based on this source code, new computational algorithms, both for the fluid dynamics and for the structural analysis, were programmed and validated within these work.

The presentation will be subdivided into different chapters:

- Chapter 2: Flow Analysis.
  In this chapter, the governing equations will be presented and it will be concluded that potential flow is a good approximation to calculate the forces generated about upwind sails. The existing models will be presented, and two specific models will be selected. Finally, computation of aerodynamic coefficients will be carried out to validate and verify the validity of the method by comparing experimental values or with the values computed with another solver previously validated

- Chapter 3: Structural analysis
  This chapter will be centred in the algorithm implemented to analyse the structure and compute its response to the flow. The method used will be the finite element method (FEM). The chapter starts with the presentation of the finite element model used for each part of the structure, and afterwards the different types of elements will be validated.

- Chapter 4: Fluid-Structure Interaction
  The interaction between the structure and the external flow will be considered by formulating a complete model. This interaction is carried out by an iterative algorithm to be presented in this chapter.

[3] GID is a universal, adaptive and user-friendly pre and postprocessor for numerical simulations in science and engineering. For more information see the web page http://gid.cimne.upc.es

- Chapter 5: Rigging monitoring
  During the sailing, the crew trims the sails varying their position and adjusting the stress of the sheets and stays. The main objective of this chapter is to develop a tool to monitor the rigging and sails.
  At this chapter will be explained the evolution of the monitoring tool developed and the treatment of the data obtained by the sensors to obtain the trim parameters will be presented, too.

- Chapter 6: Integration of monitoring data with the coupled fluid-structure interaction algorithm.
  A flexible sensor has been designed to monitor any rope/cable of the boat rigging. Examples of the application of this element to the different elements of the boat will be presented. The data of each sensor will be communicated with the FSI solver by a TCL interface, which will be introduced in this chapter.

- Chapter 7: Conclusions
  Finally the general conclusions of the thesis will be presented and the possible future work will be presented, too.

2 Flow Analysis

One of the main calculation steps of the computational solver presented at this thesis is the airflow computation around upwind sails. From this point on, this solver will be referred as the 'Fluid Solver' (FS), and will be the main focus of this chapter.

First of all, the governing equations will be presented with different approaches, first considering the viscous effects and then neglecting them. Then it is justified that potential flow is a good approximation to calculate the forces generated about upwind sails. The existing potential flow solvers types will be present, and two specific models of Vortex Lattice Method (VLM) will be selected to implement our FS. Finally, computation of aerodynamic coefficients will be carried out to validate and verify the validity of the method by comparing experimental values or with the values computed with another solver previously validated

2.1 The flow

Sails are thin bodies immersed in a fluid, the air. All Newtonian fluids, like air, must fulfill the following continuity and momentum conservation equations:

$$\frac{\partial \rho}{\partial t} + \boldsymbol{\nabla} \cdot (\rho \boldsymbol{V}) = 0 \tag{2.1}$$

$$\rho\left(\frac{\partial u}{\partial t} + \boldsymbol{V} \cdot \nabla \mathrm{u}\right) = \rho f_x - \frac{\partial p}{\partial x} + \frac{\partial}{\partial x}\left\{\mu\left[2\frac{\partial u}{\partial x} - \frac{2}{3}\nabla \cdot \boldsymbol{V}\right]\right\} + \frac{\partial}{\partial y}\left[\mu\left(\frac{\partial u}{\partial y} + \frac{\partial v}{\partial x}\right)\right] + \frac{\partial}{\partial z}\left[\mu\left(\frac{\partial w}{\partial x} + \frac{\partial u}{\partial z}\right)\right] \tag{2.2}$$

$$\rho\left(\frac{\partial v}{\partial t} + \boldsymbol{V} \cdot \nabla \mathrm{v}\right) = \rho f_y - \frac{\partial p}{\partial y} + \frac{\partial}{\partial y}\left\{\mu\left[2\frac{\partial v}{\partial y} - \frac{2}{3}\nabla \cdot \boldsymbol{V}\right]\right\} + \frac{\partial}{\partial z}\left[\mu\left(\frac{\partial v}{\partial z} + \frac{\partial w}{\partial y}\right)\right] + \frac{\partial}{\partial x}\left[\mu\left(\frac{\partial u}{\partial y} + \frac{\partial v}{\partial x}\right)\right] \tag{2.3}$$

$$\begin{aligned}\rho\left(\frac{\partial w}{\partial t} + \boldsymbol{V} \cdot \nabla \mathrm{w}\right) = \rho f_z - \frac{\partial p}{\partial z} + \frac{\partial}{\partial z}\left\{\mu\left[2\frac{\partial w}{\partial z} - \frac{2}{3}\nabla \cdot \boldsymbol{V}\right]\right\} + \frac{\partial}{\partial x}\left[\mu\left(\frac{\partial w}{\partial x} + \frac{\partial u}{\partial z}\right)\right] \\ + \frac{\partial}{\partial y}\left[\mu\left(\frac{\partial v}{\partial z} + \frac{\partial w}{\partial y}\right)\right]\end{aligned} \tag{2.4}$$

These equations jointly with the energy conservation equation, the state equations and the corresponding boundary and initial conditions, define completely the fluid flow problem.

The number of known exact solutions to the Navier-Stokes equations available is small and restricted to simple problems, due to the fact they are nonlinear partial differential equations. However, in many situations some terms can be neglected so that a simpler equations system can be obtained. To do so, a first step is to obtain the non-dimensionalised version of those equations, which allow comparing the relative magnitude of the terms appearing in the equations.

The reference quantities and the non-dimensional variables will be:

$$L(reference\ length, wing's chord) \qquad V(free - stream\ speed) \qquad T(characteristic\ time, \frac{L}{V})$$

$$p_0(reference\ pressure, free\ stream\ pressure) \qquad f_0(body\ force, g)$$

$$x^* = \frac{x}{L} \qquad y^* = \frac{y}{L} \qquad z^* = \frac{z}{L}$$

$$u^* = \frac{u}{V} \qquad v^* = \frac{v}{V} \qquad w^* = \frac{w}{V}$$

$$t^* = \frac{t}{T} \qquad p^* = \frac{p}{p_0} \qquad \boldsymbol{f}^* = \frac{\boldsymbol{f}}{f_0}$$

The corresponding non-dimensional continuity equation and momentum equations are:

$$\frac{\partial u^*}{\partial x^*} + \frac{\partial v^*}{\partial y^*} + \frac{\partial w^*}{\partial z^*} = 0 \tag{2.5}$$

$$\Omega \frac{\partial u^*}{\partial t^*} + u^* \frac{\partial u^*}{\partial x^*} + v^* \frac{\partial u^*}{\partial y^*} + w^* \frac{\partial u^*}{\partial z^*} = \left(\frac{1}{Fr^2}\right) f_x^* - Eu \frac{\partial p^*}{\partial x^*} + \left(\frac{1}{Re}\right)\left(\frac{\partial^2 u^*}{\partial x^{*2}} + \frac{\partial^2 u^*}{\partial y^{*2}} + \frac{\partial^2 u^*}{\partial z^{*2}}\right) \tag{2.6}$$

$$\Omega \frac{\partial v^*}{\partial t^*} + u^* \frac{\partial v^*}{\partial x^*} + v^* \frac{\partial v^*}{\partial y^*} + w^* \frac{\partial v^*}{\partial z^*} = \left(\frac{1}{Fr^2}\right) f_y^* - Eu \frac{\partial p^*}{\partial y^*} + \left(\frac{1}{Re}\right)\left(\frac{\partial^2 v^*}{\partial x^{*2}} + \frac{\partial^2 v^*}{\partial y^{*2}} + \frac{\partial^2 v^*}{\partial z^{*2}}\right) \tag{2.7}$$

$$\Omega \frac{\partial w^*}{\partial t^*} + u^* \frac{\partial w^*}{\partial x^*} + v^* \frac{\partial w^*}{\partial y^*} + w^* \frac{\partial w^*}{\partial z^*} = \left(\frac{1}{Fr^2}\right) f_w^* - Eu \frac{\partial p^*}{\partial z^*} + \left(\frac{1}{Re}\right)\left(\frac{\partial^2 w^*}{\partial x^{*2}} + \frac{\partial^2 w^*}{\partial y^{*2}} + \frac{\partial^2 w^*}{\partial z^{*2}}\right) \tag{2.8}$$

Being $\Omega = \frac{L}{TV}$ a time constant signifying the importance of time-dependent phenomena. The Froude number, $\frac{V}{\sqrt{Lg}}$, stands for the ratio of the inertial force to gravitational force. Euler number, $Eu = \frac{p_0}{\rho V^2}$, represents the ratio between the pressure and the inertia forces. And Reynolds number, $Re = \frac{\rho VL}{\mu}$, represents the ratio between the inertial and viscous forces.

If the Reynolds number is high, as in the case sailing yacht, the viscous terms become small compared to the other terms. Based on the assumption of high Reynolds number, the viscous terms can be neglected in the region outside the immediate vicinity of a solid surface. Since airflow around sails is a low Mach number flow, it can be considered as incompressible, so then constant properties will be assumed($\rho = constant, and\ \mu = constant$). Therefore, in this outer flow region, the solution can be approximated by solving the incompressible Euler equations:

$$\nabla \cdot \boldsymbol{V} = 0 \tag{2.9}$$

$$\frac{\partial \boldsymbol{V}}{\partial t} + \boldsymbol{V} \cdot \nabla \boldsymbol{V} = \boldsymbol{f} - \frac{\nabla p}{\rho} \tag{2.10}$$

Equation 2.10 is a first order partial differential equation and the solid surface boundary condition requires the specification of only one component of the velocity. Since, the flow is assumed to be un-viscous; there is no physical reason for the tangential velocity component to be zero on a stationary solid surface. Therefore the no-slip boundary condition for the Navier-Stokes equations becomes that only the normal component of velocity must be zero.

A closer investigation of high Reynolds number flows reveals that in a fluid, near the solid boundaries, shear flow derivatives become large and the viscous terms cannot be neglected even for high values of the Reynolds number. So for such flows there are two dominant regions in the flow field:

- The outer flow, where the viscous effects are negligible. A solution for the un-viscous flow in the region provides information about the pressure distribution and the related forces.
- The boundary layer: this is thin layer, near the solid boundaries, where the viscous effects cannot be ignored. Solution of the boundary layer equation will provide information about the shear stress distribution and the friction forces.

Solving a high Reynolds number flow with the assumption of an un-viscous fluid is therefore the first step toward solving the complete physical problem. In a second step, iterations between the un-viscous outer flow and the boundary layer region can be carried out in the search of a more accurate solution.

Furthermore, the vorticity in the high Reynolds number flow-field is confined to the boundary layer and the wake regions where the influence of the viscosity is not negligible and so it is appropriate to assume irrotational as well as un-viscous flow outside these confined regions.

Considering a line integral in a simply connected region along the line C:

$$\int_C \boldsymbol{V} \cdot d\boldsymbol{l} = \int_C udx + vdy + wdz \qquad 2.11$$

It is well known that if the flow is irrotational in the region, then $udx + vdy + wdz$ is an exact differential of a potential field ϕ, that is independent of the integration path C and is a function of the location of the point $P(x, y, z)$:

$$\phi(x, y, z) = \int_{P_0}^{P} udx + vdy + wdz \qquad 2.12$$

Where P_0 is an arbitrary reference point, ϕ is called the velocity potential, and the velocity at each point can be obtained as

$$\boldsymbol{V} = \boldsymbol{\nabla}\phi. \qquad 2.13$$

The substitution into the continuity equation leads to the Laplace's equation:

$$\nabla^2 \phi = 0 \tag{2.14}$$

Therefore, for an irrotational, un-viscous and incompressible flow the velocity field can be obtained from a solution of Laplace's equation for the velocity potential.

2.2 Introduction to Computational Fluid Dynamics

There are two different ways to cope with the stated fluid flow problem. The first one is considering the viscosity of the air, so the equations to solve are the Navier-Stokes equations. And the second ones, is making the assumption of an inviscid fluid, so that we would need to solve the Euler equations.

2.2.1 Viscous flow

Since the nineties, the exponential increase of the available computational resources motivated all the America's Cup challengers to investigate the capability of Navier-Stokes solvers to compute air dynamics problem around sails.

In 1993, Hedges reported in her M.E. thesis (Hedges, 1993) the first downwind Reynolds-averaged Navier-Stokes equations (RANSE) application: she adopted a finite-volume RANS solver named CFDS-FLOW·D with a $k-\varepsilon$ turbulence model as described in Hedges et al. (Hedges, 1996). The second RANS application was performed by Miyata and Lee at the Tokyo University in 1999 on an upwind configuration with an in-house-code and Baldwin-Lomax turbulence model (Miyata, 1999). More recently, Collie performed a large investigation upon turbulence models for sails applications, mainly based on two dimensional (2D) simulations. At Collie et al.(Collie, 2001) the authors wrote a review of the turbulence model to be used in sail flow analysis, reporting comments and a detailed ranking for; $k-\varepsilon$ (ke), $k-\varepsilon$ with low Re correction, $k-\omega$ in the original formulation, $k-\omega$ modified by Wilcox in 1998 (kw), $k-\omega$ shear-stress transport (sst), $k-\tau$, Spallart-Almaras (sa) and algebraic-stress-model. The authors concluded that Spallart-Almaras model performed better in the upwind conditions and the $k-\omega$ shear-stress transport model in downwind conditions. In the Viola et al. work (Viola, 2008(a)) an America's Cup Class are studied in a downwind reaching configuration sailing at 45 AWA with mainsail and asymmetrical spinnaker and a RANS analysis was performed with a very big resolution grid and the computational results was in good agreements with the experimental data.

In the last years, several authors have published numerical/experimental comparisons on upwind configurations: (Yoo, 2006(a)) and (Yoo, 2006(b)), obtained differences between numerical and experimental values less than 83% in lift and 59% drag; (Ciortan, 2007) showed differences lower than 86% in lift and 50% in drag; (Querard, 2007) obtained differences lower than 12% in lift 24% in drag; (Viola, 2008(b)) achieved differences less than 3% in lift with systematic over-estimation and less than 6% in drag.

Richter (Richter, 2003) presented an innovative aero-elastic coupling between the CFD code Fluent (Ansys Inc) and the finite element code Membrain (North Sails Inc) but no experimental comparison was presented. This work demonstrated that considering viscous effects is too time consuming for embedding to the iteration scheme of the membrane static.

The computational cost of considering the viscous effect is the reason to dismiss the study of downwind sails and RANSE models to solve the flow in the study of upwind sails. It is emphasized that at closer apparent wind angles the flow is mainly attached, and therefore non-viscous codes can accurately predict aerodynamic forces.

2.2.2 Inviscid flow

In high Reynolds number flows the effects of viscosity are effectively confined to thin boundary layers and thin wakes. Then the study of the flow around sails can be limited to flows outside these limited regions where the flow is assumed to be inviscid and incompressible[4]. Therefore, in order to develop the governing equations and the tools that will be necessary to solve the equations, it is necessary to study the effects of rotationality and to state its relationship to the effects of viscosity.[5]

Based on the different assumptions there are several methods to solve the equations:

- Potential flow solvers
    - Pure panel methods(Kerwin, 1987)(Johnson, 1980)
    - Vortex lattice methods(Hough, 1973),(DeJarnette, 1976)
- Euler Solvers
    - FDM(Rangogni, 1982), (Hirsch, 1988), (Hirsch, 1990)
    - FEM(Oñate, 2006), (Oñate, 2007)
    - FVM(Hirsch, 1988), (Hirsch, 1990)

The first two add an additional constrain of irrotationality to the flow, being the primary forms of the Boundary Element Method (BEM) for solving the Laplace equation. It is well know that any incompressible and irrotational fluid motion in a single or multiply connected region can be represented by a distribution of elementary solutions[6] over the boundaries of the fluid region (Lamb, 1932). Doing so, the flow field is solved distributing elementary solutions with unknown strength in a manner that will satisfy each individual set of geometrical boundary conditions

The Euler solvers can be considered as a further step towards solving the Navier-Stokes Equations. It is based on the coupled solution of the mass and momentum conservation equations in the absence of viscous effects. In (Sriram, 2003), the three

[4] Considering the fluid as un-viscous and incompressible, will be possible to use any method of numerical integration for differential equations, as the MEF, to solve potential flow problems.

[5] It will be made at appendix A.

[6] The elementary solutions to this potential flow problem are developed in Appendix A

dimensional Euler equations for compressible flow are modified using the idea of artificial compressibility, and discretized on unstructured tetrahedral grids to provide estimates of lift and drag for upwind sails configurations. Convergence acceleration techniques like multi-grid and residual averaging are used along with parallel computing platforms to enable these simulations to be performed in a few minutes. However, the need of parallel computing platforms, make this method not suitable for our purpose, since the aim of this work is to develop an operational tool.

One advantage about using boundary element methods is its relatively easy grid generation and fast calculation when compared to more complex methods such as Navier-Stokes or Euler potential equations solvers.

BEM for calculating the airflow around sails have been developed over many years. Some of the first works in this field was (Milgram, 1968), and these methods are still under continuous development and refinement (Fiddes, 1996).

The first step of a panel method (PM) approach is the selection of the singularity elements (source(Hess, 1964), doublet(Hess, 1972) or vortex(Woodward, 1968)) and the method of discretizing these distributions (zero-order, first-order(Hess, 1981), second-order(Hess, 1981)). Once the basic solution element is selected, the geometry of the model has to be subdivided. In this grid generating process, the element's corner points and collocation points are defined. The collocation points are those where the boundary conditions, such as the zero normal flow on a solid surface, will be enforced. If the solution is approximated by linear elements (both geometry and singularity strength) then it will be possible to define a first order approximation to the surface using a discretization of the geometry into quadrilateral panels, while a second-order approximation will be based on parabolic curved-fitting, and a third-order approximation may use a third-order polynomial curve-fitting. Similarly, the strength of the singularity distribution will be approximated by constant- strength (zero-order), linearly varying (first-order) or by parabolic (second-order) functions. The simplest and most basic three-dimensional element will have a quadrilateral geometry and a constant-strength singularity. When the strength of this constant element is unknown, a panel code using N panels can be constructed to solve for these N constants. It is very important to highlight that the grid discretization does have an effect on the solution. A good grid selection usually will require some preliminary understanding of the fluid dynamic of the problem.

As it was stated, sails are thin lifting surfaces that works at high Reynolds Numbers and relatively low speed flows, hence they can be modelled like thin lifting surfaces with vorticity in an incompressible and inviscid fluid. One of the computational methods commonly used to predict the flow over sails is the Vortex Lattice Method, VLM from now on (Couser, 1998), (Greeley, 1989), (Couser, 1998), (Jackson, 1987). This method is able to predict the flow of an inlet fluid over a number of lifting surfaces. It is relatively fast and suited for computing the flow over combinations of highly cambered, thin lifting surfaces, such a sail.

VLM is capable only of predicting the potential fluid flow over sails, since the effects of fluid viscosity and rotationality are ignored. This is a reasonable approach for predicting upwind sail performance provided that separation is restricted to small areas within the vicinity of the mast or leading edge. Should sails be operated near their maximum lift coefficient, it is possible that separation may occur from the leeward side of the sail, resulting in a much greater drag than the predicted by the potential flow model. In those regions where significant separation does not occur, the skin friction of the sail and the drag of the mast may be approximated by empirical equations and experimental data (Milgram, 1978).

As stated above, VLM is based on solutions to Laplace's Equation, and is subject to the same basic theoretical restrictions that apply to panel methods (PM). Vortex lattice methods are similar to panel methods in the following aspects: singularities are placed on a surface, the non-penetration condition is satisfied at a number of control points, and a system of lineal algebraic equations is to be solved to determine singularity strengths. Vortex lattice method differs from panel methods regarding to: VLM are oriented towards lifting effects and classical formulations ignore thickness, the boundary conditions are applied on a mean surface (not the actual surface), singularities are not distributed over the entire surface, and VLM are oriented towards combinations of thin lifting surfaces.

According to Katz and Plotkin(Katz J. and Plotkin, 2006), the biggest problem of using panel methods or vortex lattice methods for flow analysis is the consideration of potential flow tangential to the surface. This makes the flow to have zero viscous drag and, on big angles of attack, flow will still be tangential to the surface. Therefore any lifting curve obtained with panel method will be a straight line, meaning that a foil, when analyzed with an inviscid panel method, will never have a position where flow will separate and cause a stall.

The first numerical simulation of sails was conducted in the sixties at the Massachusetts Institute of Technology, when Milgram (Milgram, 1968) developed vortex lattice methods and flat wakes to investigate upwind sails. A few years later, in 1971, Gentry investigated the mainsail and jib interaction with a panel method plus boundary layer solutions (Gentry, 1971). This work was reviewed and updated 10 years later by himself (Gentry, 1981) and most of his applications in the America's Cup design were described in Gentry (Gentry, 1988). PM and VLM are still today considered as a fast and reliable tool and with a good accuracy level to foils at small angles of incidence, as reported in references (Katz J. and Plotkin, 2006).

Two of the main requirements for our Fluid Solver are the reduced computational cost and the grid adaptability to the real position of the sails. These needs make VLM the best method for our purpose, hence a this type of solver will be used in this work for the fluid dynamics analysis of an upwind sailing yacht. In the following section, the formulation of the VLM will be presented and two different strategies selected for the calculation of the aerodynamic loads. These strategies are, the method introduced in Klatz and Plotkin (Katz J. and Plotkin, 2006), which is a general method and then the method presented by Fiddes (Fiddes, 1996), which is specially

designed for its application to sails. These are based on the potential flow theory explained in the Appendage A. The two methods had been codified into the solver to calculate the coefficients and the forces generated by a flow around a thin lifting surface. These codes had been validated with experimental values for simple flat planes with different aspect ratios (AR), for a flat plate of AR=2 and for the same plate but cambered, as well as for a variety of sails geometries that are available in the literature. These validations will be analyzed in this work to determine which one is the most accurate method for the purpose of this thesis.

2.3 Vortex lattice Method

VLM is based on surface flow and assumes that flow is potential, the angle of incidence is small, and the body is slender. Then its solution can be approximated by a linear system using a superposition of singularities, positioned at discrete points over the body surface and wake (panels). Sails will be discretized in quadrilateral elements with vorticity, so each element will be a ring of vorticity segments. The vorticity of each element will be calculated with the numerical model. With the vorticity distribution it is possible to compute the jump velocity between the two sides of the sail and the pressure, the aerodynamic coefficients and the air forces over the sails. VLM is based on potential flow solutions and therefore its forte is in solving attached flow-fields. In the case of such attached flow-fields the calculated pressure distribution and the lift should be close to the experimental results, but for the drag force only the lift-induced drag portion is provided by the potential flow solution. An estimation of the viscous drag will be considered assuming it will be equivalent to the viscous drag of a flat plate(Schlichting, 1979).

Our case of study is a very thin surface, the sail, whose thickness effects can be neglected, so then it will be considered as a foil with zero thickness. It is assumed that the foil is moving at a constant speed (steady flow) in an undisturbed fluid. Let's consider a foil frame of reference with Cartesian coordinates, were it is x axis in the direction of foil chord, the y axis along the camber distance, and z along the height of foil, how is showed as follow.

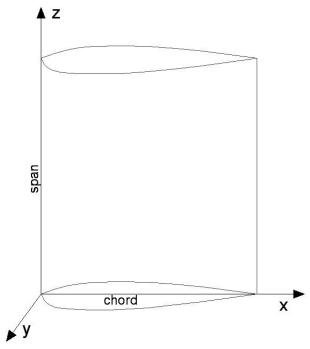

Figure 2.1. Cartesian frame of reference

The free stream velocity $\vec{Q}_\infty$ has components in the three directions $\vec{Q}_\infty = (U_\infty, V_\infty, W_\infty)$, but the approximation $W_\infty = 0$ has been selected, since for our case of

study sails are located in the xz plane and the vertical component of the wind is small and can be neglected . The components of velocity field in the foil Cartesian frame of reference are (u, v, w). And the angle of incidence α is given by the following equation

$$\alpha = \tan^{-1}\frac{V_\infty}{U_\infty} \tag{2.15}$$

As stated at the previous section, VLM is based on solutions to Laplace's Equation:

$$\nabla^2\phi^* = 0 \tag{2.16}$$

$$\phi^* = \phi + \phi_\infty \begin{cases} \phi\ perturbation\ velocity\ potential \\ \phi_\infty = U_\infty x + V_\infty y \quad free - stream\ flow's\ v.potential \end{cases} \tag{2.17}$$

Where ϕ^* is the velocity potential.

In an inviscid flow, the boundary condition to be applied on a body submerged within the fluid with impervious surface is a no penetrability boundary condition. That is to say, the velocity component normal to the body must be zero respect to a body fixed coordinate system. Hence,

$$\begin{gathered} \nabla\phi^* \cdot \vec{n} = 0 \\ \lim_{r\to\infty} \nabla\phi^* = \vec{Q}_\infty \end{gathered} \tag{2.18}$$

In a potential flow, the velocity field in related to the velocity potential by

$$\frac{\partial\phi}{\partial x} = u \qquad \frac{\partial\phi}{\partial y} = v \qquad \frac{\partial\phi}{\partial z} = w \tag{2.19}$$

Applying the principle of superposition we obtain,

$$\phi = \sum_{k=1}^{N} c_k \phi_k \tag{2.20}$$

being ϕ_k an elementary solution. Then equation 2.14 can then be written as

$$\nabla^2\phi = \sum_{k=1}^{N} c_k\, \nabla^2\phi_k = 0 \tag{2.21}$$

Hence, potential flow can be described by a sum of potentials, permitting a discretization of the body surface into singularities (sources, doublets and vortices) that satisfy Laplace equation. Therefore, the problem reduces to finding a singularity distribution that satisfies the no penetrability boundary condition on the body surface. Reminding the fact that due to the difficulty of measuring dynamically the boundary conditions with precision and to reproduce a manoeuvre in real time, only

stationary conditions will be analyzed. So then, once the distribution is found, the velocity $\vec{V}$ can be obtained from the velocity potential, and the corresponding pressure p will-be calculated from the steady-state Bernouilli equation:

$$p_\infty + \frac{\rho}{2} Q_\infty^2 = p + \frac{\rho}{2} V^2 \tag{2.22}$$

The analytical solution for an arbitrary wing shape would be complicated due the difficulty of specifying the boundary condition of not penetrability on complex shapes and by the shape of the wake. The need for a wake model follows immediately from the Helmholtz theorems, those states:

- The strength of a vortex filament is constant along its length.
- A vortex filament cannot start or end in a fluid (it must form a closed path or extend to infinity).
- The fluid that forms a vortex tube continues to form a vortex tube and the strength of the vortex tube remains constant as the tubes moves about (hence vortex elements, such a vortex lines, vortex tubes, vortex surfaces, etc., will remain vortex elements with time).

For the wing profile presented in Figure 2.2 the boundary conditions will be

Figure 2.2 Definitions for wing thickness and upper, lower surface.

$$F(x,y,z) \equiv y - \eta(x,z) = 0 \qquad \vec{n} = \frac{\nabla \mathrm{F}}{|\nabla F|} = \frac{1}{|\nabla F|}\left(-\frac{\partial \eta}{\partial x}, 1, -\frac{\partial \eta}{\partial z}\right) \tag{2.23}$$

$$\begin{gathered} \nabla \phi^* \cdot \vec{n} = \left(\frac{\partial \phi}{\partial x} + U_\infty, \frac{\partial \phi}{\partial y} + V_\infty, \frac{\partial \phi}{\partial z}\right) \cdot \frac{1}{|\nabla F|}\left(-\frac{\partial \eta}{\partial x}, 1, -\frac{\partial \eta}{\partial z}\right) = 0 \rightarrow \\ \rightarrow \frac{\partial \phi}{\partial y} = \frac{\partial \eta}{\partial x}\left(\frac{\partial \phi}{\partial x} + U_\infty\right) + \frac{\partial \phi}{\partial z}\left(\frac{\partial \eta}{\partial z}\right) - V_\infty \end{gathered} \tag{2.24}$$

Above condition can be linearized, by taking some additional assumptions. For a foil shown in Figure 2.2, the small-disturbance approximation can be assumed to be such that:

$$\frac{\left|\partial \phi /_{\partial x}\right|}{Q_\infty}, \frac{\left|\partial \phi /_{\partial y}\right|}{Q_\infty}, \frac{\left|\partial \phi /_{\partial z}\right|}{Q_\infty} \ll 1 \tag{2.25}$$

The foil must have a slender shape, that is to say:

$$\left|\frac{\partial \eta}{\partial x}\right| \ll 1 \qquad \left|\frac{\partial \eta}{\partial z}\right| \ll 1 \tag{2.26}$$

Applying these approximations, the boundary condition on the foil become:

$$\frac{\partial \phi}{\partial y}(x, \eta, z) = Q_\infty \left(\frac{\partial \eta}{\partial x} - \alpha\right) \tag{2.27}$$

Moreover, it is also consistent with the above approximation to also transfer the boundary condition from the wing surface to the plane $x - z$. This is accomplished by a Taylor series expansion of the dependent variable:

$$\frac{\partial \phi}{\partial y}(x, y = \eta, z) = \frac{\partial \phi}{\partial y}(x, 0, z) + \eta \frac{\partial^2 \phi}{\partial y^2}(x, 0, z) + O(\eta^2) \tag{2.28}$$

Along with the small-disturbance approximation, only the first term from the last equation is retained. Then the first order approximation of the boundary condition becomes.

$$\frac{\partial \phi}{\partial y}(x, 0, z) = Q_\infty \left(\frac{\partial \eta}{\partial x} - \alpha\right) \tag{2.29}$$

Since the Laplace equation and the boundary condition have been linearized, it is possible to solve three simpler problems and superimpose the three separate solutions, as shown in Figure 2.3. Note that this decomposition of the solution is valid only if the small-disturbance approximation is applied to the wake model as well.

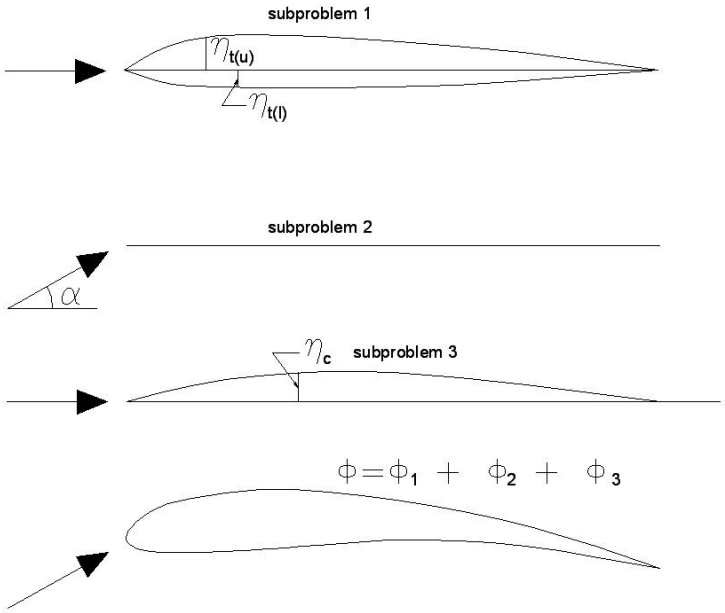

Figure 2.3. Decomposition of the thick cambered wing at angle of attack into simpler problems.

Sub-problem 1: Symmetric wing profile with non-zero thickness at zero angle of attack

Governing equations:

$$\nabla^2\phi_1 = 0$$

$$\frac{\partial\phi_1}{\partial y}(x, 0\pm, z) = \pm Q_\infty \frac{\partial\eta_t}{\partial x}$$

where + is for the upper and – is for the lower surfaces, and $\eta_t = \frac{1}{2}(\eta_u - \eta_l)$. Due to the symmetry of the problem, a source/sink distribution placed at the wing centreline section, can be used to model the flow.

Sub-problem 2: Zero thickness, un-cambered wing at angle of attack.

$$\nabla^2\phi_2 = 0 \qquad \frac{\partial\phi_2}{\partial y}(x, 0\pm, z) = -Q_\infty\alpha \tag{2.30}$$

Sub-problem 3: Zero-thickness, cambered wing at zero angle of attack

$$\nabla^2\phi_3 = 0 \qquad \frac{\partial\phi_3}{\partial y}(x, 0\pm, z) = \frac{\partial\eta_c}{\partial x}Q_\infty \quad \eta_c = \frac{1}{2}(\eta_u + \eta_l) \tag{2.31}$$

The complete solution for the cambered wing with nonzero thickness at an angle of attack is then

$$\phi = \phi_1 + \phi_2 + \phi_3 \tag{2.32}$$

Usually, the two linear problems of angle of attack and cambered are solved together. The resulting problem to be solved in this case, is

$$\nabla^2\phi = 0 \qquad \frac{\partial\phi}{\partial y}(x, 0\pm, z) = Q_\infty\left(\frac{\partial\eta_c}{\partial x} - \alpha\right) \tag{2.33}$$

This problem is anti-symmetric with respect to y direction and can be solved by a doublet distribution or by a vortex distribution. These basic solutions are solutions to Laplace equation and fulfil the boundary condition at infinity, $\lim_{r\to\infty}\nabla\phi^* = \vec{Q}_\infty$.

As stated above, according to the Helmholtz theorem the vortex lines cannot begin and end in the fluid. This means that if the lifting problem is to be modelled with vortex elements they cannot be ended at the wing and must be shed into the flow (Katz J. and Plotkin, 2006). In order not to generate force in the fluid, these free vortex elements must be parallel to the local flow direction, at any point on the wake.

Sails are lifting surfaces that can be considered as zero thickness cambered wing with an angle of attack. Hence, the flow around the sails can be modelled by either a distribution of doublets or by a distribution of vortex in the surface (Milgram, 1968). In any case, the most important variable for this problem is the amount of circulation Γ generated by the sail.

In three-dimensional flows, according to Katz and Plotkin (Katz J. and Plotkin, 2006), if a wing is looked at from the distance, it can be modelled as a vorticity segment generating an amount of circulation. Then when the vortex reaches the surface limits, the vorticity vector turns to be parallel to the local velocity vector and they shed into some length within flow (see Figure 2.4).

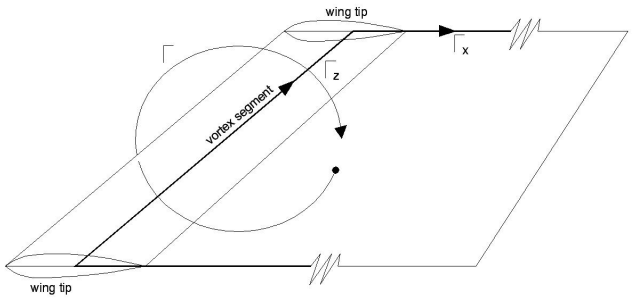

Figure 2.4. Scheme of vortex segment development in a finite wing according to Helmholtz theorem

If a foil is discretized into many span-wise lines of vorticity, these lines will leave the wing at different points along the trailing edge, generating the wake. As wakes cannot generate force in the fluid, the lines coming out of trailing edge should be parallel to the local flow direction at any point and the vortex singularity strength γ_W along this line or, the doublet strength μ_W, must be constant (Katz J. and Plotkin, 2006).

According to Hess (Hess, 1974) and Katz and Plotkin (Katz J. and Plotkin, 2006), the wake modelling is part of the solution and, the disturbed potential equation should take into account the wake vorticity. Then, sails and wake will be discretized into singularity vortex elements.

Therefore, the first step of the numerical solution will be to determine the circulation for each element. Then, once the distribution of circulation is known, it is possible to calculate the pressure distribution, the velocity field and the aerodynamics loads.

2.3.1 The aerodynamic Loads

In order to obtain the aerodynamic loads, the pressure needs to be evaluated by means of the Bernouilli equation. To do so, the velocity at any point in the field is obtained as a combination of the free-stream velocity and the perturbation velocity:

$$\vec{V} = \left(Q_\infty \cos\alpha + \frac{\partial\phi}{\partial x}, Q_\infty \sin\alpha + \frac{\partial\phi}{\partial y}, \frac{\partial\phi}{\partial z}\right) \quad 2.34$$

Substituting $\vec{V}$ into the Bernouilli equation, the difference between the free stream pressure and the perturbed pressure can be obtained.

$$p_\infty - p = \frac{\rho}{2}(V^2 - Q_\infty^2) \quad 2.35$$

And the pressure coefficient C_p is evaluated as

$$C_p \equiv \frac{p - p_\infty}{\frac{1}{2}\rho Q_\infty^2} = 1 - \left(\frac{V}{Q_\infty}\right)^2 \quad 2.36$$

Then aerodynamic loads can be calculated by integrating the pressures over the wing surface.

$$\vec{F} = -\int_{wing} p\vec{n}\, dS \quad 2.37$$

Aerodynamicist frequently refers to the forces in the free stream coordinates and therefore these forces must be transformed accordingly. The lift and drag forces are:

$$\begin{aligned} L &= -F_x \sin\alpha + F_y \cos\alpha \\ D &= F_x \cos\alpha + F_y \sin\alpha \end{aligned} \quad 2.38$$

Usually, the aerodynamic loads are presented in a non-dimensional form. In the case of the force coefficients where F can be either lift, drag, or side force the corresponding coefficients will have the form

$$C_F = \frac{F}{\frac{1}{2}\rho Q_\infty^2 S} \quad 2.39$$

Where S is a reference area (wing planform area for wings).

2.3.2 Discretization

Previously, it has been explained the reasons to select the Vortex Lattice Method to calculate the flow around sails, which can be considered like three-dimensional thin lifting surfaces. The first step of the VLM is to discretize the sails; the discretization selected in this work will be the simplest one, consisting of quadrilateral elements of vorticity where each element will be a ring of vorticity segments. The strength of the singularity distribution can be approximated by constant-strength (zero order), linearly varying (first order) or by parabolic functions (second order). In this thesis the simplest and most basic three dimensional elements will be adopted: vortex ring elements with constant-strength singularity. Then the geometry will be discretized

into N quadrilateral elements with a constant-strength, and to calculate the constant-strength of each element, a solver algorithm will be programmed. The main advantage of using these elements is that they require very little programming effort.

The velocity potential of the singularity elements, also called vortex ring elements, is based on the vortex line solution. The boundary condition that must be satisfied by the solution is the zero normal flow normal to the wing solid surface.

$$\nabla(\phi + \phi_\infty) \cdot \vec{n} = 0 \;\; over \; S \tag{2.40}$$

As stated above, in order to solve this lifting surface problem numerically, the sail must be discretized into elements containing vortex ring singularities, as shown in the following picture.

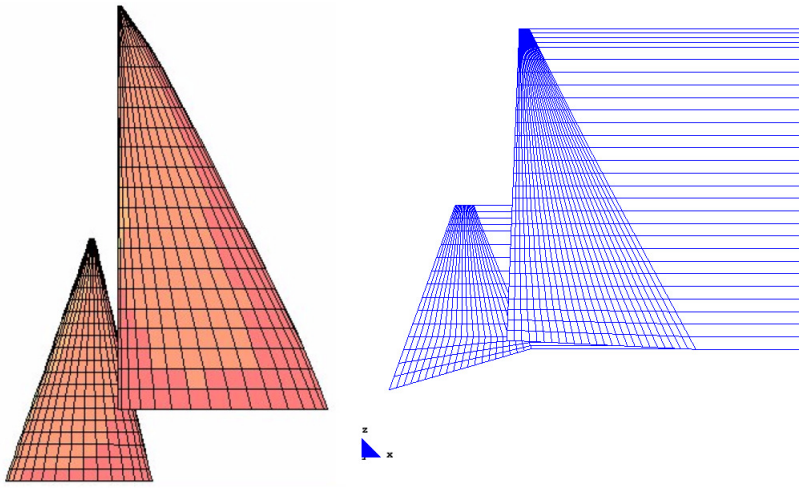

Figure 2.5. Typical vortex lattice panel layout

2.3.3 Choice of singularity elements

The simplest possible discretization adopted by some authors, consist of discretizing uniformly into equal quadrilateral elements. Then the collocation points (CP) are placed at the geometric centre of each element. For two-dimensional flow, several works (James, 1972) showed that if the vortex is located at the quarter-chord point and the collocation point at the three-quarter chord point, for a flat plate the lift coefficient obtained is exact. This result has been extended to three dimensions by discretizing the span into strips of panels and applying the “quarter chord theorem” to each panel on a strip. A modification of this basic approach is to inset the vortex segment nearest the tip by a quarter of the width of the panels (Hough, 1973). However, an inconvenience consequence of this approach is that the vortex lattice does not include the edges of the configuration. Furthermore, although the overall loads on a lifting surface are usually predicted with good accuracy using the classical VLM, the prediction of the detailed load distribution is generally poor.

An important improvement from the simple vortex lattice was developed by Lan (Lan, 1974). He developed his quasi-vortex-lattice method (QVLM), where the element edges and collocation points are distributed along the chord c according to cosines distribution. The paper presented by Lan (Lan, 1974), gives a mathematical justification for this form of the vortex lattice method in two dimensions, based on returning the exact result for the vorticity on a flat plate incidence (which the quarter-chord method cannot). However, the extension to three dimensions is not based on any formal proof of "optimal" locations of vortex strips and control points across the span.

The use of a "cosine" distribution of control points and panel sizes has been traditionally used in lifting surface methods, to concentrate control points and panels near leading and trailing edges (Weber, 1954). These concentrations of elements allow reflect the rapid variation in the solution near the leading edge, and at tips in three dimensions.

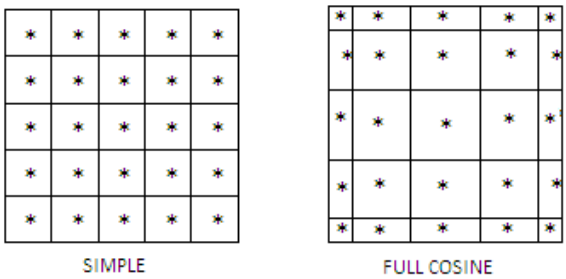

Figure 2.6. Vortex Lattice Method discretization

Although there is no mathematical proof of why the full-cosine lattice discretization should be superior to others, but a careful study by Jackson and Fiddes (Jackson, 1995) has shown that it has some remarkable properties.

In this thesis, the simplest discretization and collocation point distribution will be used. The wing will be divided into vortex ring elements and following the simple model presented by Hess and Smith (Hess, September 1964), the collocation points are approximated as the centre point of element. And following the study of Jackson and Fiddes (Jackson, 1995), it will be analyzed the properties of refining the mesh towards the edges of the surface. The discretization will not follow the full cosine distribution, but the size of the panels near the edges will be smaller in order to reflect the rapid variation in the solution on these locations.

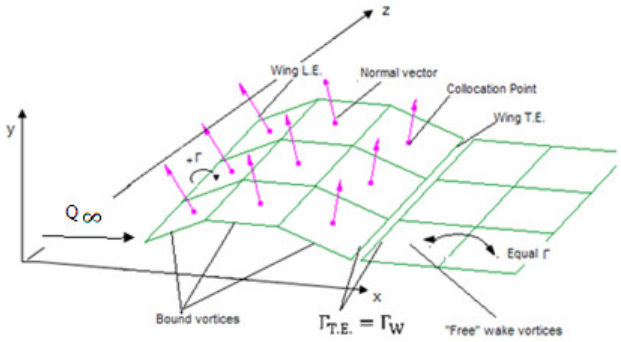

Figure 2.7. Vortex Ring model for a thin lifting surface

2.3.4 Boundary conditions

The desired numerical solution is obtained by enforcing:

- The Kutta condition at each trailing segment. The theoretical form of the Kutta condition states that the velocity shall remain finite along the sharp trailing edge of a lifting surface. For membrane flows, a condition which imposes no trailing edge vorticity is recommended. The condition requires that the lifting surface potential jump at the trailing edge be equal to the potential jump imposed by the wake at the trailing edge. It is, along the wing trailing edges, the trailing vortex of the last ring element row must be cancelled to satisfy the three-dimensional trailing edge condition. For steady-state flow this is done by attempting to align the wake vortex elements parallel to the local streamlines, and their strength is equal to the strength of the shedding panel at the trailing edge Figure 2.7.
- The zero normal velocity boundary condition at control points. The normal velocity component at each point on the surface is a combination of the induced velocity and the free-stream velocity. Therefore, the zero normal flow boundary condition can be presented as

$$\vec{V} \cdot \vec{n} = 0 \quad on\ each\ control\ point \tag{2.41}$$

Division of the velocity vector into the induced and free-stream components yields to

$$(u, v, w) \cdot \vec{n} + (U_\infty, V_\infty, W_\infty) \cdot \vec{n} = 0 \tag{2.42}$$

The first term of the last equation is the velocity induced by the singularity distribution on itself and the second term is the free stream component $\vec{Q}_\infty = (U_\infty, V_\infty, W_\infty)$.

The self-induced part can be represented by a combination of *influence coefficients*, while the free-stream contribution is known and will be transferred to the right-hand side of the boundary condition.

$$(u, v, w) \cdot \vec{n} = -(U_\infty, V_\infty, W_\infty) \cdot \vec{n} \tag{2.43}$$

To establish the self-induced portion of the normal velocity, at each collocation point, consider the velocity induced by all the singularities at each collocation point.

2.3.4.1 Velocity induced by a vortex ring element in a collocation point

The velocity induced on an arbitrary point $P(x,y,z)$, by a quadrilateral vortex ring, can be computed by considering that the vortex consists of four lines.

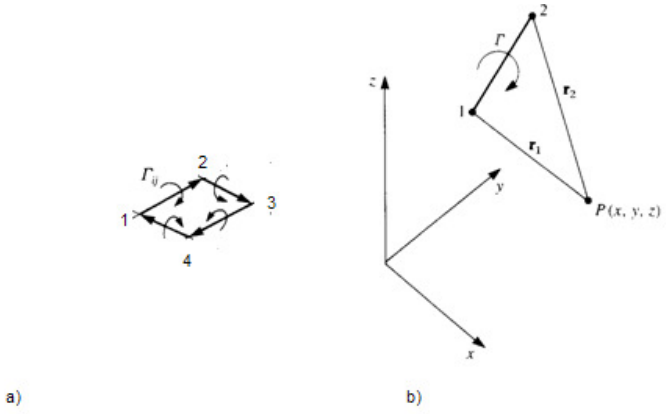

Figure 2.8. a)Vortex ring b) Line of a vortex ring

The velocity induced by each line of the ring is calculated applying the Biot-Savart's law.

$$\vec{V}_{1,2} = \frac{\Gamma}{4\pi} \frac{\vec{r_1} \times \vec{r_2}}{|\vec{r_1} \times \vec{r_2}|^2} \vec{r_0} \cdot \left(\frac{\vec{r_1}}{r_1} - \frac{\vec{r_2}}{r_2} \right) \quad 2.44$$

Where Γ is the strength of the vortex ring.

For computational purposes it can be included in a subroutine to calculate the induced velocity (u,v,w) at a point $P(x,y,z)$ as a function of the vortex line strength and its edges coordinates. For the sake of clarity, the following formulas are given for Γ=1.0.

$$(u,v,w)_{line1} = \vec{V}_{1,2} = \frac{1}{4\pi} \frac{\vec{r_1} \times \vec{r_2}}{|\vec{r_1} \times \vec{r_2}|^2} \vec{r_0} \cdot \left(\frac{\vec{r_1}}{r_1} - \frac{\vec{r_2}}{r_2} \right) \quad 2.45$$

The same procedure is applied to the other lines of the ring.

$$\begin{aligned} (u,v,w)_{line2} &= \vec{V}_{2,3} = \frac{1}{4\pi} \frac{\vec{r_2} \times \vec{r_3}}{|\vec{r_2} \times \vec{r_3}|^2} \vec{r_0} \cdot \left(\frac{\vec{r_2}}{r_2} - \frac{\vec{r_3}}{r_3} \right) \\ (u,v,w)_{line3} &= \vec{V}_{3,4} = \frac{1}{4\pi} \frac{\vec{r_3} \times \vec{r_4}}{|\vec{r_3} \times \vec{r_4}|^2} \vec{r_0} \cdot \left(\frac{\vec{r_3}}{r_3} - \frac{\vec{r_4}}{r_4} \right) \\ (u,v,w)_{line4} &= \vec{V}_{4,1} = \frac{1}{4\pi} \frac{\vec{r_4} \times \vec{r_1}}{|\vec{r_4} \times \vec{r_1}|^2} \vec{r_0} \cdot \left(\frac{\vec{r_4}}{r_4} - \frac{\vec{r_1}}{r_1} \right) \end{aligned} \quad 2.46$$

The induced velocity generated by the vortex ring at $P(x, y, z)$ is, therefore

$$(u, v, w) = (u, v, w)_{line1} + (u, v, w)_{line2} + (u, v, w)_{line3} + (u, v, w)_{line4} \quad 2.47$$

The calculation of this velocity is implemented within the computer program in a subroutine.

A unit strength vortex is used in the process of evaluating the influence coefficient. The influence coefficient of the i vortex at the j collocation point a_{ij} is:

$$a_{ij} = (u, v, w)_{ij} \cdot \vec{n}_j \quad 2.48$$

When a particular vortex ring (k) is at the trailing edge, a "free wake" vortex ring with the same strength is added to cancel the spanwise starting vortex line. Therefore, when the influence of such trailing-edge panel vortex is calculated, the contribution of the element wake that contains this segment must be added.

At this point, it will be calculated the velocity induced only by the trailing vortex segments, that is, the vortex lines parallel to the free stream. The influence of the trailing segments of a vortex ring on a point is:

$$(u, v, w)_{trailing\ segments} = (u, v, w)_{line2} + (u, v, w)_{line4} = (u, v, w)^* \quad 2.49$$

Using a unit strength vortex in the process of evaluating the influence coefficient for the velocity induced by the trailing vortex segments, the influence coefficient of the i vortex at the j collocation point b_{ij} is:

$$b_{ij} = (u, v, w)^*_{ij} \cdot \vec{n}_j \quad 2.50$$

2.3.5 Right hand side (RHS) calculation

The RHS vector is computed by scanning each of the collocation points of the wing.

$$RHS_k = -\vec{Q}_\infty \cdot \vec{n}_k \quad 2.51$$

2.3.6 Solve linear system of equations

Once the computations of the influence coefficients and the right-hand side vector are completed, the boundary condition of zero normal velocity on each of the collocation points will result in the following set of algebraic equations:

$$\begin{pmatrix} a_{11} & \cdots & a_{1m} \\ \vdots & \ddots & \vdots \\ a_{m1} & \cdots & a_{mm} \end{pmatrix} \begin{pmatrix} \Gamma_1 \\ \vdots \\ \Gamma_m \end{pmatrix} = \begin{pmatrix} RHS_1 \\ \vdots \\ RHS_m \end{pmatrix} \quad 2.52$$

Where m is the total number of ring element used. The solution of this set of equations results in the vector $(\Gamma_1, \Gamma_2, \ldots, \Gamma_m)$. A preconditioned bi-conjugate

gradient method (BiCG) is used to solve the system of linear equations. Once the circulation of each singularity element is known, it is possible to calculate the total velocity of the flow, pressures and the loads.

2.3.7 Secondary Computations: Pressures, Loads, Velocities.

At this point two different ways of loads calculations (one presented in Katz and Plotkin(Katz J. and Plotkin, 2006) and the second presented by Fiddes and Gaydon (Fiddes, 1996)) will be presented in the following sections.

2.3.7.1 Calculation method presented by Katz and Plotkin

In the method presented by Katz and Plotkin (Katz J. and Plotkin, 2006), the lift of each bound vortex segment is obtained by using the Kutta-Joukowski theorem, which states:

"The resultant aerodynamic force in an incompressible, inviscid, irrotational flow in an unbounded fluid is of magnitude $\rho Q_\infty \Gamma$ per unit width, and acts in a direction normal to the free stream.

$$\vec{F} = \rho \vec{Q}_\infty \times \vec{\Gamma} \tag{2.53}$$

Where $\vec{F}$ is the aerodynamic force per unit width and acts in the direction determined by the vector product."

So the lift of each mesh element can be obtained by:

$$\begin{cases} \Delta L_k = \rho Q_\infty \Gamma_k \Delta z_k & if\ the\ panel\ is\ at\ the\ leading\ edge \\ \Delta L_k = \rho Q_\infty (\Gamma_k - \Gamma_{k-1}) \Delta z_k & if\ the\ panel\ is\ not\ at\ the\ leading\ edg \end{cases} \tag{2.54}$$

Where the index $k-1$ indicates the vortex ring which share the side one of the element scanned with it. And Δz_k is de width of the panel k in the z direction, it is perpendicular to the free stream.

The pressure difference across a vortex ring element is

$$\Delta p_k = \frac{\Delta L_k}{\Delta S_k} \tag{2.55}$$

where ΔS_k is the element area.

The induced-drag computation is somewhat more complex.

$$\begin{cases} \Delta D_m = -\rho w_{ind.m} \Gamma_m \Delta z_m & if\ the\ vortex\ ring\ element\ is\ at\ the\ leading\ edge \\ \Delta D_m = -\rho w_{ind,} (\Gamma_m - \Gamma_{m-1}) \Delta z_m & if\ thevortex\ ring\ element\ is\ not\ at\ the\ leading\ edge \end{cases}$$

The induced downwash, $w_{ind,m}$ at each collocation point m, is computed by summing up the velocity induced by all the trailing vortex segments.

$$\begin{pmatrix} w_{ind,1} \\ \vdots \\ w_{ind,m} \end{pmatrix} = \begin{pmatrix} b_{11} & \cdots & b_{1m} \\ \vdots & \ddots & \vdots \\ b_{m1} & \cdots & b_{mm} \end{pmatrix} \begin{pmatrix} \Gamma_1 \\ \vdots \\ \Gamma_m \end{pmatrix} \quad 2.56$$

The total lift and drag can also be calculated by summing the individual vortex ring element contributions.

$$D = \sum_{i=0}^{m} \Delta D_i \quad 2.57$$

$$L = \sum_{i=1}^{m} \Delta L_i \quad 2.58$$

2.3.7.2 Calculation method presented by Fiddes and Gaydon

Fiddes and Gaydon (Fiddes, 1996) presented an alternative interpretation and implementation of the vortex lattice method initially studied by Jackson and Fiddes (Jackson, 1995). In his model the sail surface carrying the continuous distribution of doublicity is discretized into a set of vortex ring elements, each one carrying a locally constant value of doublicity (Γ) at the collocation point, where the boundary condition of tangential flow is applied. With this discretization, the integral giving the velocity induced by the continuous distribution of doublicity is replaced by the line integral around the panel edges. The Biot-Savart law is used to evaluate the velocity induced by a line vortex lying along the edge of a panel, with circulation equal to the difference in doublicity of the vortex ring elements having that edge in common. An implicit Kutta condition is used to determine the doublicity distribution in the wake, where the doublicity of a wake strip is set equal to the doublicity of the sail vortex ring element abutting the wake strip, removing the line vortex at the junction of the surface and wake.

The total normal velocity, induced plus onset components, is set to zero according to the surface boundary condition and this determines the doublicity at the collocation point. Until this point, the model presented by Fiddes and Gaydon (Fiddes, 1996) is the same that the presented by Katz and Plotkin (Katz J. and Plotkin, 2006), so that the calculation of the circulation of each vortex ring element can be done using the method presented before. The difference between the two methods lies in the calculation of the pressures and the forces.

In the Fiddes and Gaydon method (Fiddes, 1996), the velocity induced by the doublicity distribution at the collocation point is split in two components- one normal $(u_{n,ind})$ to the surface and the other $(u_{m,ind}, u_{l,ind})$ in the tangent plane of the surface at the collocation point. The free stream is transformed to the coordinates of the vortex ring element $\vec{Q}_\infty = (q_{m,\infty}, q_{l,\infty}, q_{n,\infty})$.

The tangential velocity induced by the vortex lattice at a collocation point is regarded as being the mean induced velocity at that point. To obtain the actual velocities on either side of the sail at the collocation point, half of the velocity jump is added to the mean velocity to give the upper surface velocity, and half of the velocity jump is subtracted to give the lower surface velocity.

In order to obtain the velocity jump along the direction s, which is $\frac{\partial \Delta\phi}{\partial s}$, a simple finite difference approximation is used. As the mean velocity is available at the collocation point, the velocity jump is also evaluated there. To evaluate the derivative of the doublicity at the collocation point, the computed doublicity at the collocation points is interpolated to give values at the panel vertices. For a free edge that is not shedding a wake, the doublicity is zero along the edge, so no extrapolation is required. For a wake shedding edge a simple linear or quadratic extrapolation is used. For the internal panel vertices, a simple averaging of the values of doublicity at the surrounding collocation points is used.

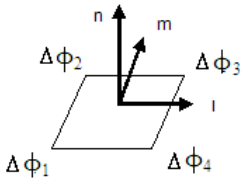

Figure 2.9. Panel coordinates

Once the doublicity distribution has been re-distributed from the collocation points to the vortex ring vertices, the gradient of the doublicity over the surface at collocation point is approximated by a simple finite difference across the vertices of the vortex ring element. This is combined with the mean tangential velocity previously computed by the vortex lattice to give the velocities on each side of the sail.

$$\vec{V}_{up} = \left(q_{m,\infty} + u_{m,ind} + \frac{1}{2}\frac{\partial \Delta\phi}{\partial m}, q_{l,\infty} + u_{l,ind} + \frac{1}{2}\frac{\partial \Delta\phi}{\partial l}, 0\right)$$
$$\vec{V}_{down} = \left(q_{m,\infty} + u_{m,ind} - \frac{1}{2}\frac{\partial \Delta\phi}{\partial m}, q_{l,\infty} + u_{l,ind} - \frac{1}{2}\frac{\partial \Delta\phi}{\partial l}, 0\right) \quad 2.59$$

The method relies on an accurate estimate of the doublicity distribution on the sail. This critically depends on how the sail is discretized into vortex ring elements and where the collocation points lie. Fiddes and Gaydon (Fiddes, 1996) analyzed the following panelling schemes:

1. Cosine vertices, panel centre collocation
2. Cosine collocation, but at panel centroids
3. Full cosine
4. Constant span-wise and chord-wise panel sizes

They found that the full cosine distribution gave the most accurate results for a given number of vortex ring elements. Here it will be tested the constant span-wise and chord-wise elements size distribution, as well as a distribution with smaller elements towards the edges.

With the velocities of the two sides of the sail, it is possible to calculate pressures, their dimensionless coefficients, and loads.

$$p_{up} = p_\infty - \frac{1}{2}\left(V_{up}^2 - Q_\infty^2\right) \quad 2.60 \qquad p_{down} = p_\infty - \frac{1}{2}\left(V_{down}^2 - Q_\infty^2\right) \quad 2.61$$

$$C_{pup} = 1 - \left(\frac{V_{up}}{Q_\infty}\right)^2 \quad 2.62 \qquad C_{pdown} = 1 - \left(\frac{V_{down}}{Q_\infty}\right)^2 \quad 2.63$$

In case the wing is assumed to be thin, the pressure difference across the wing Δp and the resulting force are evaluated as:

$$\Delta p = p_{down} - p_{up} \quad 2.64$$

$$\vec{F} = -\int_{wing} \Delta p \cdot \vec{n}\, dS \quad 2.65$$

$$D = F_x cos\alpha + F_y sin\alpha \quad 2.66$$

$$L = F_y cos\alpha - F_x sin\alpha \quad 2.67$$

2.4 Validation studies

In the following, we are going to make some studies to validate the VLM implemented in our program *Sailing.* This VLM has been implemented in C++ using a set of existent libraries and the resulted code has been integrated with the pre/post-process system GID[7].

It has been explained before, that in this work two methods to calculate the pressures and loads have been implemented: (1) the method presented at the reference of Katz and Plotkin (Katz J. and Plotkin, 2006), which will be named as 'Katz&Plotkin method'; and (2) the method presented at the reference of Fiddes and Gaydon(Fiddes, 1996) which will be named as 'Fiddes&Gaydon method'.

Now, it is necessary to establish which of these formulations is the most accurate. To do so, we are going to study accuracy versus the number of vortex ring elements using homogeneous grids. Once the number of elements required for accurate results has been obtained, a non-homogeneous grid with smaller elements towards

[7] A user guide of the resulting software is presented in Appendix B.

the edges will be tested. It was already proved by Fiddes and Gaydon (Fiddes, 1996) that this type of grids have good properties.

Results will be obtained using two different methods; first the calculation done using 'Katz&Plotkin method' and the calculation done using the 'Fiddes&Gaydon method'. Then the results will be compared with calculations of other solvers and/or experimental data presented in the literature:

- Validation Case 1: Comparison of $\frac{C_l}{\alpha}$ against experimental results obtained for flat plates with different aspect ratios provided Jones and Cohen(Jones, 1960).
- Validation Case 2: Comparison of C_l and C_d against experimental results obtained for flat plate and cambered plate with an aspect ratio of 5 provided in Marchaj (Marchaj, 2003).
- Validation Case 3: Comparison of lift and drag coefficients with experimental and numerical results presented in Yoo (Yoo, 2006).
- Validation Case 4: Comparison of lift and drag coefficients, and total force over the sail with numerical results obtained by Couser (Couser, 1998).
- Validation Case 5: Comparison of lift and drag coefficients with experimental and RANSE results presented in Fiddes and Gaydon (Fiddes, 1996).

Due to lack of detailed information about the geometries used in the above mentioned works, the geometries used in some of the validations cases will not be exact. These geometries will be approximated by geometries generated using the program SailCut(Lainè) . To do so, the overall dimensions for the real geometries, provided in the above mentioned works, will be used. On the other hand, exactly the same wind conditions for each corresponding validation case will be used.

2.4.1 Validation Case 1

In this validation case, a planar wing plan-form with no camber and bounded by straight lines as leading, trailing and side edges will be analyzed. For this test, the geometry analysed with the fluid solver is exactly the same used for the experimental analyses. The slope of the lift curve C_{l_α} versus the aspect ratio (AR) is calculated by the different implementations used in this thesis. Then the results are compared with those presented by Jones and Cohen (Jones, 1960).

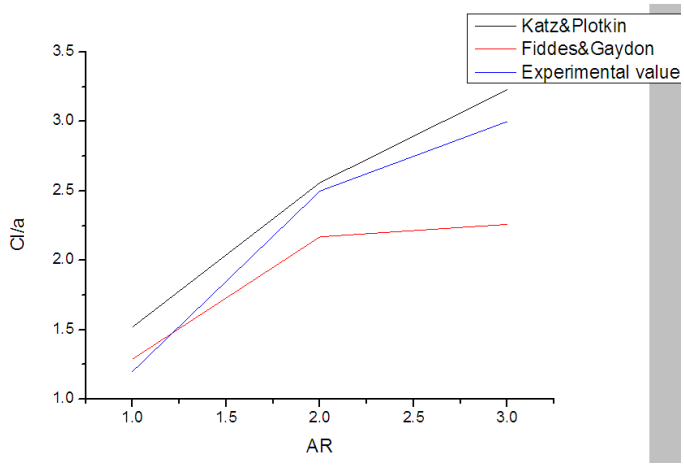

Figure 2.10.Effect of aspect ratio on the lift coefficient slope of un-tapered planar wings

AR	Accuracy of Katz&Plotkin method	Accuracy of Fiddes&Gaydon method
1	73%	92%
2	98%	87%
3	92%	75%

Table 2-1. Accuracy of the two methods

Looking at Table 2-1 it can be observed that the most accurate results are obtained by the method presented by Katz and Plotkin (Katz J. and Plotkin, 2006). In this table we can see the low accuracy of the Fiddes and Gaydon method for a flat plate of AR=3. This low accuracy can be connected to the fact that geometry is a flat plate. The Fiddes and Gaydon method is specially designed for its application to sails, and sails are thin and cambered foils. Therefore, the absence of camber could be the reason of the poor accuracy in this case.

2.4.2 Validation Case 2

We want to study sails that are thin cambered airfoils, so it is necessary to study the accuracy of the two methods implemented in our solver with a flat plate and with a cambered plate.

Now we are going to compare our results with the experimental data available at one of the books of C.A. Marchaj (Marchaj, 2003). The data are the aerodynamic coefficients C_l and $C_d$for a flat foil and for a foil having a camber of 1/10, for different angles of incidence. The areas in both cases were the same and AR=5.

In the next figure are shown the experimental data and the results obtained with our solvers.

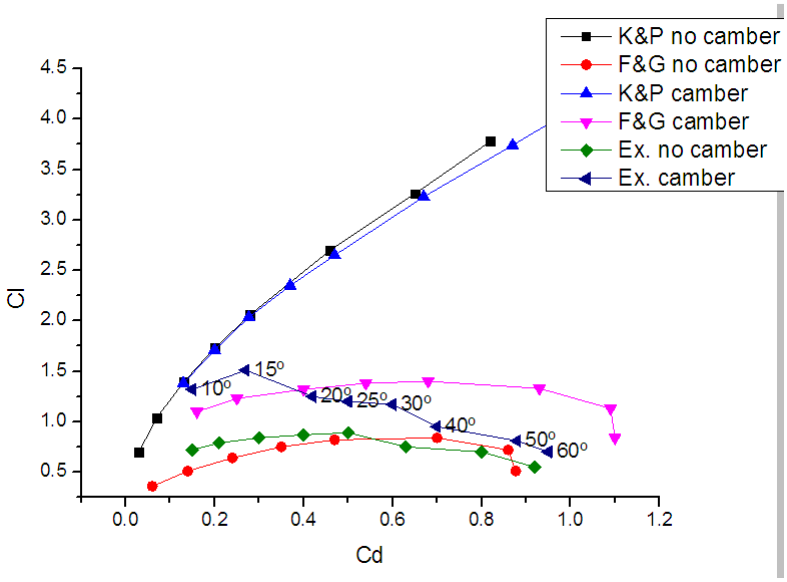

Figure 2.11. Polar diagrams for two rectangular foils-one cambered and one flat. AR=5

Now, it is proven the good accuracy of the Fiddes and Gaydon method for different angles of incidence and for cambered foils.

It is important to emphasize the fact that or program is thought to be used for upwind conditions, therefore the angles of incidences must be smaller of 35°. Apparent wind angles of 50° and 60° are too large to be considered as close hauled sailing. For these angles, it is usual the flow is not attached to the sail, and the approximation of potential flow is not correct.

2.4.3 Validation Case 3

Figure 2.12 shows the sail system of a 30 feet sloop developed by Kordi(Yoo, 2006). The principal dimensions of the main sail are $P = 11.9m$, $E = 4.0m$ and $A_M = 23.8m^2$. The principal dimensions of the jib sail are $J = 3.9m$, $I = 11.0m$ and $A_F = 21.5m^2$. The incident angle of apparent wind is set to $20°$ with respect to the centre line of the boat, and the speed of wind assumed is $20\ knots$.

The experiments were carried out in the wind tunnels of the Chungnam National University of Korea and the results of the aerodynamic coefficients were $C_l = 1.4$ and $C_d = 0.3$. Then the same geometry was tested using the RANSE code WAVIS considering turbulent flows. The aerodynamic coefficients resulting from the WAVIS calculations were $C_l = 1.2$ and $C_d = 0.22$. Therefore this viscous code achieves an accuracy of the 86% for the lift and 73% for the drag.

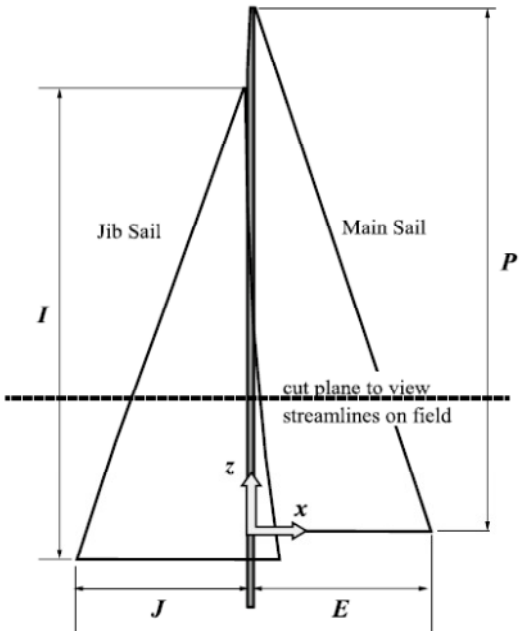

Figure 2.12. Schematic view of sail system

First we carried out our calculations using a homogeneous element size and with control points located at the centre of each element. A convergence study varying the element size to test accuracy of the method has been carried out. The results are shown in the following pictures.

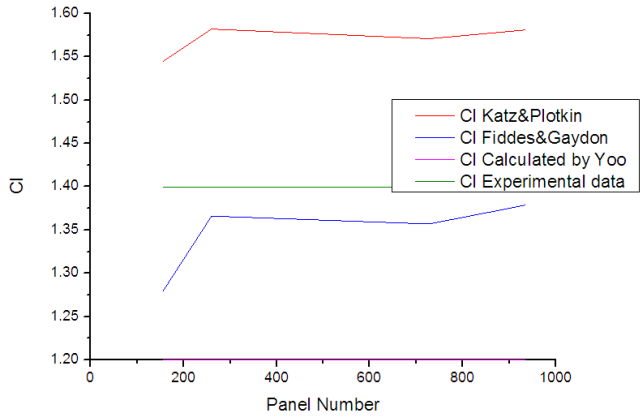

Figure 2.13. Calculations of Cl varying the number of elements

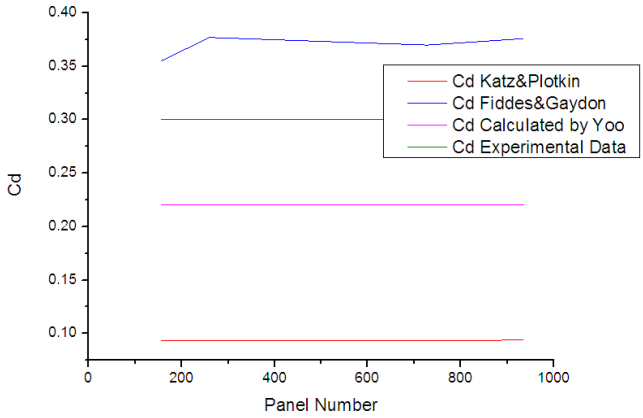

Figure 2.14. Calculations of Cd varying the number of elements

Looking at Figure 2.13 and Figure 2.14, we can observe that convergence is reached when the number of elements used is around 260 elements. The following table shows the accuracy, measured as $(1 - \text{relative error})$, between our different calculations and the experimental data.

Number of Elements	Katz&Plotkin		Fiddes&Gaydon	
	C_l	C_d	C_l	C_d
156	90%	31%	91%	82%
260	87%	31%	98%	74%
728	88%	31%	97%	77%
936	87%	31%	98%	75%

Table 2-2. Accuracy of the two methods programmed at the FS.

The results obtained by using the 'Fiddes&Gaydon method' are more accurate, and using a grid of 260 elements, the results are already quite accurate.

Since the method presented by Fiddes and Gaydon (Fiddes, 1996) uses a smaller grid towards the edges of the sails, a non-homogeneous grid with this characteristic, has been tested too. This grid has 260 elements with smaller elements towards the edges as suggested by Fiddes and Gaydon (Fiddes, 1996).

Table 2-3 compares the accuracy of the different methods using an homogeneous grid and non-homogeneous grid.

Number of Elements	Homogeneous grid				Non-homogeneous grid			
	Katz & Plotkin		Fiddes & Gaydon		Katz & Plotkin		Fiddes & Gaydon	
	C_l	C_d	C_l	C_d	C_l	C_d	C_l	C_d
260	87%	31%	98%	74%	88%	82%	99%	82%

Table 2-3. Difference of accuracy using a homogeneous grid and non-homogeneous grid

As can be seen, the accuracy in this case has been improved. Still, the 'Fiddes&Gaydon method' is more accurate, and this accuracy is obtained with a few

number of elements. The need of few elements to obtain enough accuracy for practical purposes, allows a faster calculation.

It is important to emphasize the fact, that the accuracy of the 'Fiddes&Gaydon method' implemented in our FS is better both in the case of an homogeneous grid (98%, 75%) and a non-homogeneous grid (99%,82%) than the accuracy of WAVIS (86%,73%). It is important by the fact that WAVIS is a RANSE code, so then it is more complex and computationally more expensive than our FS. This is a good proof than our FS is a good approximation.

2.4.4 Validation Case 4

Couser (Couser, 1998) developed a computational model and applied it to obtain the upwind performance of the International Mirror Class dinghy. In this study the sail forces were computed using a vortex lattice model only capable of predicting the potential fluid flow around sails, so that the effects of fluid viscosity are ignored. The skin friction of the sails and the drag of the mast were approximated by empirical equations and experimental data provided by (Milgram, 1978).

LOA	3.3m
Beam	1.4m
Draft	0.1m, board raised
Mast Height	4.9m, mast and gaff from deck
Mast Length	3.3m
Gaff Length	2.8m
Boom Length	2.3m
Sail Area	6.5m^2
Main	4.6m^2
Jib	1.9m^2

Table 2-4. International Mirror Class dinghy dimensions

Figure 2.15. International Mirror Class dinghy

The results obtained by Couser will be compared with the results obtained using the methods implemented in this thesis. Aerodynamic coefficients will be calculated varying the number of elements and using homogeneous grid to test the

convergence and accuracy of the implemented methods. The obtained results are presented in the following pictures.

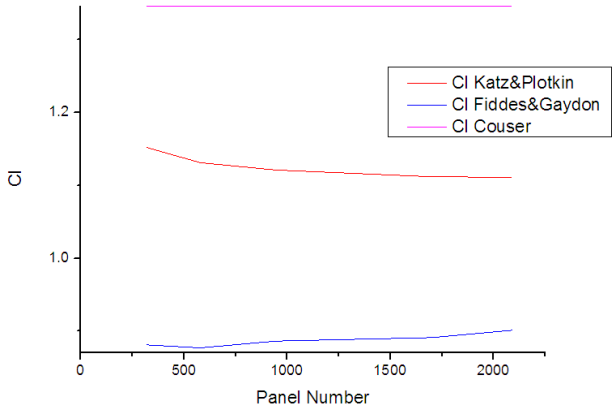

Figure 2.16. Calculations of Cl varying the number of elements

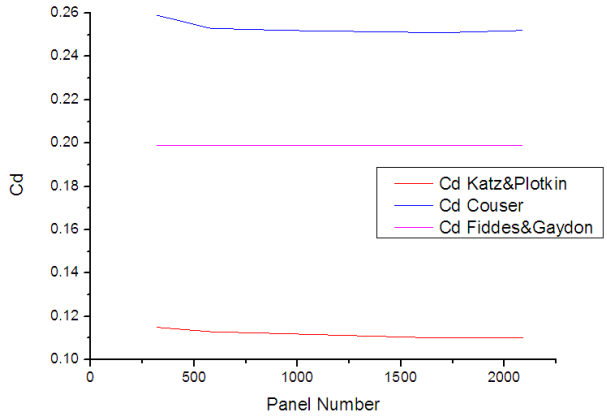

Figure 2.17. Calculations of Cd varying the number of elements

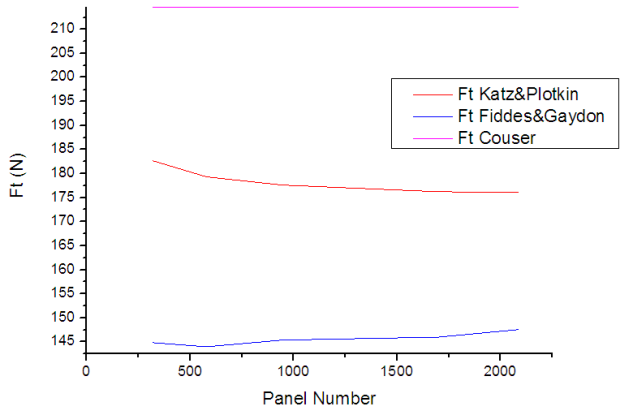

Figure 2.18. Calculations of the total force varying the number of elements

Table 2-5 shows the accuracy of each calculation respect to the results obtained by Couser. It can be observed that the accuracy doesn't depend excessively on the number of elements used since little change is appreciated when increasing the number of elements over 945.

Number of Elements	Katz&Plotkin		Fiddes&Gaydon	
	C_l	C_d	C_l	C_d
320	86%	58%	65%	70%
580	84%	57%	65%	73%
945	83%	56%	66%	73%
1700	83%	55%	66%	74%
2090	83%	55%	67%	73%

Table 2-5. Accuracy of the two methods

Numerical simulations were carried out fixing the number of elements to 945 but using a non-homogeneous grid with smaller elements towards the edge. Table 2-6 compares the results obtained with the homogeneous and non-homogeneous grids.

Number of Elements	Homogeneous grid				Non-homogeneous grid			
	Katz&Plotkin		Fiddes&Gaydon		Katz&Plotkin		Fiddes&Gaydon	
	C_l	C_d	C_l	C_d	C_l	C_d	C_l	C_d
945	83%	56%	66%	73%	83%	95%	70%	95%

Table 2-6.Difference of accuracy using a homogeneous grid and non-homogeneous grid

In the non-homogeneous case, while the lift coefficient and the total force are more accurate using 'Katz&Plotkin method', the calculation of the drag coefficient is more accurate using 'Fiddes&Gaydon method'. Moreover, the accuracy of the lift coefficient of the 'Katz&Plotkin method' is independent of the element's size near the edges, and the 'Fiddes&Gaydon method' provides better results with smaller elements near the edges for the two coefficients.

We must point out that in this validation case, our results have been compared to numerical results obtained provided by (Couser, 1998), and no comparison with experimental results have been made.

2.4.5 Validation Case 5

Now we will compare our FS with the original VLM of Fiddes and Gaydon(Fiddes, 1996). The original implementation by Fiddes and Gaydon allows for vortex shedding from the foot and leach of the sail, and is capable of calculating the subsequent roll-up. A recursive sub-panelling and vortex merging method was used to give stable wake roll-up calculations. A simple, strip-based, integral boundary layer method was used to give some estimate of the profile drag levels on the sails. It included a special treatment of leading-edge bubbles for sails without mast, and a simple treatment on the initial boundary layer development downstream of the mast.

Results for a 2/5 th scale model Finn rig are compared with the experimental results presented by Marchaj (Marchaj, 1969)[8]. The model had a luff of 2.29m with a sail area of 1.68 m^2, and was tested in the 3.6m by 4.6m working section of the tunnel test of Southampton. Two cases were tested, listened in Table 2-7.

	Wind Speed (m/s)	Boom Incidence (degrees)	Boom setting	Mean Camber	Mean twist (degrees)
CASE 1	7.9	25	Up	2.7	14.8
CASE 2	7.9	25	Horizontal	9.5	6.3

Table 2-7. Tested cases

The experimental results of the two cases are showed following.

	C_L	C_D
CASE 1	1.012	0.295
CASE 2	1.260	0.386

Table 2-8. Lift and drad coefficients from tests

For the CASE 1, Fiddes and Gaydon investigated the effect of the number of elements on the predicted lift and drag using a reflection plane to represent the sea surface, except in a case indicated “no fs”. All the results of the Fiddes and Gaydon calculations are showed in the next table.

Panelling	C_L	C_L accuracy	C_D	C_D accuracy
12x12	1.147	87%	0.209	71%
16x16	1.138	87%	0.2074	70%
16x16(no fs)	1.092	92%	0.206	70%
20x20	1.139	87%	0.2088	71%
24x24	1.141	87%	0.2095	71%

Table 2-9. Results of the Fiddes and Gaydon calulations of the CASE 1

Looking their results, we can see the little dependence of the accuracy on the number of elements. The most accuracy calculation is which does not consider the image of the sail. Being based on this fact, all our calculation will not consider the reflection plane.

For the CASE 2, they did not investigate the effect of the number of elements on the predicted lift and drag. Their resulting lift and drag coefficients are shown in the following table.

Panelling	C_L	C_L accuracy	C_D	C_D accuracy
24x24	1.564	76%	0.270	69%

Table 2-10. Results of the Fiddes and Gaydon calculations of CASE 2

In the following, the methods implemented in this thesis are going to be compared with the experimental results, considering that our geometry could be slightly

[8] This references has not been found, so then the geometry has been created using the data presented in the reference of Fiddes and Gaydon.

different than the original geometry, due to the lack of information in the literature. Anyhow, we will compare our results with the experimental results of the two cases to prove that our results are within a reasonable error range.

The effect of the number of elements on the predicted lift and drag has been investigated and following will be presented the lift coefficients and the drag coefficients for the different homogeneous meshes and for the different methods implemented in our solver.

Number of Elements	Katz&Plotkin		Fiddes&Gaydon	
	C_l	C_d	C_l	C_d
210	1.135	0.126	0.821	0.213
288	1.127	0.124	0.826	0.211
720	1.113	0.121	0.840	0.200
1080	1.110	0.120	0.857	0.205

Table 2-11. Results for the different homogeneous meshes and for the different methods implemented

Now, these results will be compared with the experimental results of the two cases.

Number of elements	Katz&Plotkin				Fiddes&Gaydon			
	CASE 1		CASE 2		CASE 1		CASE 2	
	C_l	C_d	C_l	C_d	C_l	C_d	C_l	C_d
210	88%	43%	90%	32%	81%	72%	65%	54%
288	89%	42%	89%	31%	82%	72%	66%	54%
720	90%	41%	88%	31%	83%	68%	67%	51%
1080	90%	41%	88%	30%	85%	70%	68%	53%

Table 2-12. Results of our solver for an homogeneous grid

Table 2-12 shows the accuracy of each method compared with the experimental results. Looking at Table 2-12, it is observed that 'Katz&Plotkin method' is quite independent of the element numbers while the 'Fiddes&Gaydon method' shows little dependence. Moreover, the 'Katz&Plotkin method' gives better results for the lift while the 'Fiddes&Gaydon method' gives better results for the drag when using the uniform mesh.

Since now, our results have been for a homogeneous grid. But, as in the previous validation cases, the simulations have been carried out first with a homogeneous grid varying the element's number, and secondly the number of elements will be fixed and the grid will be refined towards the edges. Using an inhomogeneous grid of 1080 elements, the results of the coefficients using the 'Katz&Plotkin' method are $C_L = 1.118$ and $C_{Di} = 0.182$, and the results of the coefficients using the 'Fiddes&Gaydon' method are $C_L = 0.944$ and $C_{Di} = 0.194$ Therefore, now we can compare these results with the experimental results of the two cases.

Number of Elements	CASE 1				CASE 2			
	Katz&Plotkin		Fiddes&Gaydon		Katz&Plotkin		Fiddes&Gaydon	
	C_l	C_d	C_l	C_d	C_l	C_d	C_l	C_d
1080	90%	62%	93%	66%	89%	46%	75%	53%

Table 2-13. Results of our solvers for a non homogeneous grid

We can see that all our calculations are into a range of accuracy considering that our geometry is not the same that the tested geometry.

It is important to stand out in the fact that our 'Fiddes&Gaydon method' and 'Katz&Plotkin method' are accurate as the original implementation by Fiddes and Gaydon (Fiddes, 1996) for the lift coefficient. But for the drag coefficient our method is less accurate than the original implementation by Fiddes and Gaydon. This fact is a result of that our implemented methods don't consider neither the integral boundary layer method, neither the initial boundary layer development downstream of the mast.

Fiddes and Gaydon estimated the mast drag considering it as a circular cylinder with a drag coefficient of 1.2 and they used a strip boundary layer calculation to estimate the profile drag of the sail for the CASE 1. This gave them a drag coefficient contribution from the mast of 0.067 and 0.017 from the sail. The drag contribution of the mast represents the 23% of the total drag and the contribution of the boundary layer of the sail represents the 5.9% of the total drag coefficient. The contribution of the mast is bigger than the contribution of the sail.

It is well known, the influence of a foresail on the mainsail. In the book of Marchaj (Marchaj, 2003) are showed the flows for an isolated mainsail and for a mainsail joined with a foresail. These results clearly demonstrate to what extent the foresail stabilizes the flow over the leeward side of the mainsail against unwanted separated flow, particularly just abaft the mast. It does this by reducing the flow speed over the forward-lee part, but the contribution of t of the mainsail. This in turn delays or prevents flow separation which usually commences from the mast. Therefore could be a good approximation do not consider the drag introduced by the mast when analyzing a complete sail rigging.

Therefore, if we deduct the 23% of the experimental drag for disregarding the effect of the mast, it has a value of $C_D = 0.223$ for the CASE 1 and $C_D = 0.297$ for the CASE 2. And now we can compare our results with these experimental values that do not consider the mast.

Number of Elements	CASE 1				CASE 2			
	Katz&Plotkin		Fiddes&Gaydon		Katz&Plotkin		Fiddes&Gaydon	
	C_l	C_d	C_l	C_d	C_l	C_d	C_l	C_d
1080	90%	82%	93%	87%	89%	61%	75%	65%

Table 2-14.Accuracy of our method compared with the experimental results, deducting the effect of the mast

Now, it is proved the good accuracy for the drag coefficient.

2.5 Conclusions

The Vortex Lattice Method has been selected in this thesis to compute the flow over sails. Two different methods, which differ in the computation of the pressures and loads, have been selected: the method presented by Katz and Plotkin (Katz J. and Plotkin, 2006) (Katz&Plotkin method') and the method presented by Fiddes and

Gaydon (Fiddes, 1996) ('Fiddes&Gaydon method'). These methods provide results in good agreement with experimental results and with other solvers based on different methods and approaches. Generally, in the case of a homogeneous grid the 'Katz&Plotkin method' is more accurate for calculating the lift coefficient. However the 'Fiddes&Gadon method' is more accurate for calculation the drag coefficient in both cases, with a homogeneous grid and non-homogeneous grid and it gives a better detailed load distribution, especially near the edges. So then the method selected to be used in *Sailing* is the 'Fiddes&Gaydon method'.

The 'Katz&Plotkin method' and 'Fiddes&Gaydon method' are considered simple methods in the sense that they do not consider neither the roll up of the wake, nor boundary layer, nor the effect of the sea surface, nor the effect of the mast. However, in spite of their simplicity, they provide quite close results to those based on more sophisticated and also computationally more expensive algorithms.

Since having a low calculation time is a mandatory requirement for a program designed for real time operation during navigation, the use of these 'simple methods' is a good choice for this type of operational applications.

3 Structural analysis

One goal in this thesis is to study the response of the sail and the rigging to the flow. The first step is to compute the aerodynamic loads and the second step is to compute the response of the structure to these loads. In the previous chapter the FS developed to compute the aerodynamic loads has been introduced, and now we are going to present the algorithm implemented to analyse the structure and compute its response. This step will be named as 'structural step' and the part of the program to solve the response of the structure will be named 'FEA solver'. The method to be used will be the well known Finite Element Method, FEM, from now on(Oñate, 2009)(Zienkiewicz, 1982).

In this chapter, it will be explained first the FEM model used for each part of the structure, and afterwards the 'FEA solver' will be validated for the different types of elements.

3.1 Introduction

Sails can be studied as flexible membranes (Taylor, 2001). A membrane is essentially a thin shell with non flexural stiffness, consequently a membrane do not resist any compression at all. In such a theory only the in plane stresses are included.

Membranes need supporting structures. The main sail is supported by the mast, the boom and battens (if has any). These supporting structures are, in modern racing yachts, slender in order to keep flow disturbance to a minimum and, they have a certain degree of flexibility to allow shape adjustment. The flexibility of the rigging allows trimming the sail, and the change in the shape of the sails affects the airflow, which in turn changes the forces acting on the rigging. So it is necessary to consider the coupled effect of every element of the rigging structure with the fluid dynamics of the sails to be able to predict the behaviour of a sailing yacht.

The sailing yacht rigging structure mainly consists of main sail, jib, a mast, spreaders, forward stay, back stay, shrouds, main sheet and jib sheet.

Regarding the numerical modelling of the different elements, the main sheet, jib sheet, forward stay, back stay and shrouds, can be modelled as cables, so they only resist axial traction forces. On the other hand, the mast and spreaders are rigid structures, these can cope not only axial forces, but also bending moments. Therefore they must be analysed using beam theory (Oñate, 2009)(Cook, 2002). As stated above, the behaviour of sails leads to large displacement analysis of very thin structures leading to the classical models of membranes, where flexion stresses are negligible. Due to large displacements, these models are geometrically nonlinear, and since strains in modern sails remain low, constitutive laws of the material can be consider as linear, and stress in the structure as linear functions of the local strains.

Geometrically nonlinear membranes have been extensively studied with theoretical models (Antman, 1995) and numerical implementations (Zienkiewicz, 1977), but they require important computational efforts. And we must keep in mind that one of the objectives of this work is the real-time simulation of sails response to incident flow. So then, complex nonlinear membranes models are considered too expensive in CPU time, to be used for that purpose. Therefore, a simplified model will be used in this work.

The structural part of the simulation tool to be implemented in this work is based on a Finite Element Analysis with different types of finite elements to define each part of the structure:

- It is assumed that sails can be accurately modelled as membranes (Arcaro, 2004(a)). Triangular elements of three nodes will be used to discretize sails.
- Ropes or cables of the structure (shrouds, sheets and stays) only resist traction axial forces. Since cables are pre-stressed, they can be modelled with bar elements, because they never will be subject to compression forces. Furthermore, dividing the cable into several articulated bar elements (truss), it is possible to reproduce the behaviour of the cable. Therefore these elements will be named as cable elements instead of bar elements. Discretization will be done using elements of two nodes with three degrees of freedom per node (Arcaro, 2004(b)).
- The rest of the elements of the structure (mast, spreaders and boom) resist axial and transversal forces, and bending moments, so they will be modelled as beam elements. These structures will be discretized into 3D beam elements (Cook, 1995), which resist axial force, transverse shear force in each two directions, bending about each principal axis of the cross section, and torsion about the longitudinal axis of the member. So, a two nodes bar element with six degrees of freedom per node will be used.

The solution procedure includes the generation of the structure model, by means of all the presented elements, imposition of boundary or support conditions and the solution of the equations to obtain nodal quantities by imposing the minimization of the potential energy.

Considering a conservative mechanical system, it has an energy potential. That is, one can express the energy content of the system in terms of its configuration, without reference to whatever strain history or path way have led to that configuration. Potential energy, also called total potential energy E_{TOT}, includes (a) the strain energy of elastic distorsion $\phi(\boldsymbol{x})$, and (b) the potential possessed by applied loads Ω, by virtue of they having the capacity to do work if displaced. Reminding that the structures will be analyzed after each configuration change done by the crew, the resulting configuration will be considered in stationary state. So then, the equilibrium configuration will be defined by the principle of stationary potential energy:

Among all admissible configurations of a conservative system, those that satisfy the equations of equilibrium make the potential energy stationary with respect to small admissible variations of displacements.

At the problem studied, the air flow applies external loads on the structure, causing the displacement and strain of the different elements. Given the nodal displacements vector $\boldsymbol{x}$ and the nodal flow forces $\boldsymbol{f}$, the potential possessed by applied loads can be written $\Omega = -\boldsymbol{f}^T\boldsymbol{x}$.

The strain energy $\phi(\boldsymbol{x})$ is calculated of different manner, depending of the finite element analysed (membrane, cable or beam).

The total potential energy will be:

$$E_{TOT} = \sum_{elements} \phi(\boldsymbol{x}) - \boldsymbol{f}^T\boldsymbol{x} \qquad 3.1$$

And thus the equilibrium configuration is found from the stationary value of the total potential energy:

$$\frac{\partial E_{TOT}}{\partial \boldsymbol{x}} = \sum_{elements} \nabla\phi\,(\boldsymbol{x}) - \boldsymbol{f} = 0 \qquad 3.2$$

To solve the equilibrium condition it is necessary to calculate the gradient of the internal potential energy of each element. In the following sections, the method used to calculate it for each type of element that configures our structure (cables, beams and membranes) will be presented. Then, the iterative procedure to obtain the equilibrium configuration will be introduced. Finally, the different elements implemented will be validated.

3.2 Structural modelling of sails

Numerical analysis of sails as flexible membranes started with the two-dimensional theory (Jackson, 1983)(Nielsen, 1963)(Thwaites, 1961)(Grennhalgh S., 1984). From these analysis results the understanding of some basic features of sails. But from the structural point of view, a sail for this special case degenerates to a cable. And a cable can only support lateral loads if it is fixed at both ends. The leading edge for a sail is indeed fixed at the mast or the forestay, but the trailing edge is free. Thus a two-dimensional sail model is a non-realistic one. A three-dimensional aerodynamic theory of sails was first presented by Milgram in 1968 (Milgram, 1968) and Jackson introduced a more sophisticated model in 1985 (Jackson, 1985).

The algorithm implemented in this work, for the calculation of the strain of the sail is based on two publications by Arcaro (Arcaro, 2004(a)) and (Arcaro, 2004(b)). It assumes homogeneous and isotropic linear elastic material. The method used is based on non-linear FEM paradigm, however it can be enhanced to orthotropic materials with minor modifications. The assumption of isotropic material is a notable

restriction for today spinnaker designs, however for the sole purpose of calculating the flying shape of the sail, this simplification has been accepted.

The sails will be discretized with 3D isotropic membrane finite elements. It consists of a total Lagrangian description of a linear elastic material, and can be used to calculate the Green strain tensor. The approach presented by Arcaro recovers the basic idea of minimizing the total potential energy to find equilibrium. As the total potential energy is a nonlinear function of the nodal displacements, a quasi-Newton method is used to find its minimum. The reasons to select this method are the different advantages that it presents:

- It is not necessary to derive an expression for the stiffness matrix.
- It is not necessary to solve any system of equations.
- It permits a simple static analysis instead of a pseudo-dynamic analysis, such as dynamic relaxation with kinetic damping as described by Barnes(Barnes, 1999).

Sails will be discretized with triangular membrane elements, as described in the following.

The reference system, xy plane, is located in the plane of the element. The geometry of a triangular membrane is defined by the nodes i=1,2,3, edge lengths opposite to the node λ_l, the angles at the nodes α_i and the unity vectors parallel to the edges $\hat{u}_i = \{cos\theta_i, sin\theta_i\}^T$, where θ_i is the angle between the x axes and the edge i of the triangular element.

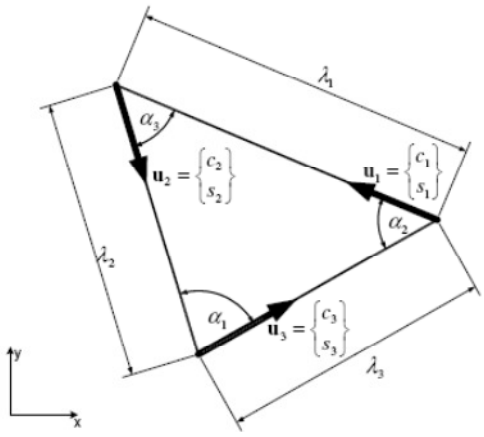

Figure 3.1. Triangular membrane element

Assuming small strains of the sail, Green strain definition can be used. It is emphasized that this is not an important restriction for the sail model. Since the materials used in practice for the sails are quite stiff, and therefore small strain approach seems to be reasonable. Furthermore, for any iteration, the elements will be updated in a Lagrangian way, following the calculated sails displacements. Then, at the end of the fluid-structure iteration process, large displacements of the sails can be achieved.

The strain ε in the arbitrary direction $\hat{u}_i$ is calculated from:

$$\varepsilon_i = cos^2\theta_i\varepsilon_{xx} + sin^2\theta_i\varepsilon_{yy} + 2cos\theta_i sin\theta_i\varepsilon_{xy} \tag{3.3}$$

Being θ_i the angle between the x axis and the direction of each side of the triangle, $\hat{u}_i$.

The indexes of the orthogonal strains show direction of strain and direction of stress causing strain in the x-y plane. For the vector of strains along the three edges of the triangle, the following expression holds:

$$\boldsymbol{\varepsilon} = \boldsymbol{C}\bar{\boldsymbol{\varepsilon}}$$

$$\begin{pmatrix}\varepsilon_1\\ \varepsilon_2\\ \varepsilon_3\end{pmatrix} = \begin{pmatrix}\cos^2\theta_1 & \sin^2\theta_1 & \sqrt{2}\cos\theta_1\sin\theta_1\\ \cos^2\theta_2 & \sin^2\theta_2 & \sqrt{2}\cos\theta_2\sin\theta_2\\ \cos^2\theta_3 & \sin^2\theta_3 & \sqrt{2}\cos\theta_3\sin\theta_3\end{pmatrix}\begin{pmatrix}\varepsilon_{xx}\\ \varepsilon_{yy}\\ \sqrt{2}\varepsilon_{xy}\end{pmatrix} \tag{3.4}$$

Being $\boldsymbol{C}$ the rotation matrix.

Considering a linear elastic material and plane stress strains, the stress-strain laws can be simplified(Timoshenko, 1959) to:

$$\bar{\boldsymbol{\sigma}} = \bar{\boldsymbol{H}}\bar{\boldsymbol{\varepsilon}} \rightarrow \begin{pmatrix}\sigma_{xx}\\ \sigma_{yy}\\ \sqrt{2}\sigma_{xy}\end{pmatrix} = \frac{E}{1-\nu^2}\begin{pmatrix}1 & \nu & 0\\ \nu & 1 & 0\\ 0 & 0 & 1-\nu\end{pmatrix}\begin{pmatrix}\varepsilon_{xx}\\ \varepsilon_{yy}\\ \sqrt{2}\varepsilon_{xy}\end{pmatrix} \tag{3.5}$$

Where $\boldsymbol{H}$ is the so called stiffness matrix.

The strain energy density for a linearly elastic body can be written as

$$\phi = \frac{1}{2}\bar{\boldsymbol{\varepsilon}}^T\bar{\boldsymbol{\sigma}} = \frac{1}{2}\bar{\boldsymbol{\varepsilon}}^T\bar{\boldsymbol{H}}\bar{\boldsymbol{\varepsilon}} = \frac{1}{2}\boldsymbol{\varepsilon}^T(\boldsymbol{C}^{-1})^T\bar{\boldsymbol{H}}\boldsymbol{C}^{-1}\boldsymbol{\varepsilon} = \frac{1}{2}\boldsymbol{\varepsilon}^T((\boldsymbol{C}^{-1})^T\bar{\boldsymbol{H}}\boldsymbol{C}^{-1})\boldsymbol{\varepsilon} = \frac{1}{2}\boldsymbol{\varepsilon}^T\boldsymbol{H}\boldsymbol{\varepsilon} \tag{3.6}$$

$$\boldsymbol{H} = \frac{E}{1-\nu}\boldsymbol{A}^{-1}(\boldsymbol{I} + \nu\boldsymbol{B}\boldsymbol{A}^{-1}) \tag{3.7}$$

$$\boldsymbol{A} = \boldsymbol{C}\boldsymbol{C}^T = \begin{pmatrix}1 & \cos^2\alpha_3 & \cos^2\alpha_2\\ \cos^2\alpha_3 & 1 & \cos^2\alpha_1\\ \cos^2\alpha_2 & \cos^2\alpha_1 & 1\end{pmatrix} \tag{3.8}$$

$$\boldsymbol{B} = \begin{pmatrix}0 & \sin^2\alpha_3 & \sin^2\alpha_2\\ \sin^2\alpha_3 & 0 & \sin^2\alpha_1\\ \sin^2\alpha_2 & \sin^2\alpha_1 & 0\end{pmatrix} \tag{3.9}$$

Let V be the undeformed volume of the element, the potential strain energy can be written as

$$\phi = \int_V \phi\, dV = \frac{1}{2}\int_V \boldsymbol{\varepsilon}^T\boldsymbol{H}\boldsymbol{\varepsilon}\, dV \tag{3.10}$$

For an arbitrary displacement component x_i, the derivative of the potential strain energy is:

$$\frac{\partial \phi}{\partial x_i} = \int_V \boldsymbol{H\varepsilon} \frac{\partial \boldsymbol{\varepsilon}}{\partial x_i} \, dV \tag{3.11}$$

The following expressions can be derived from planar calculus and under the assumption of small displacements. The nodes of the triangle are denoted $i = 1,2,3$ according to (Arcaro, 2004(a))and the nodal displacements vectors are numbered according to its node numbers.

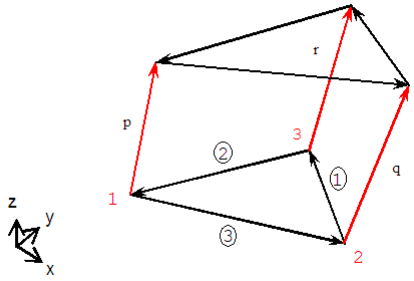

Figure 3.2. Nodal displacements

To write the directional strain for a side of the triangle, we will consider a vector $\hat{u}$, unitary and parallel to the undeformed side, λ is the undeformed length of the side and $\vec{p}$ and $\vec{q}$ are the nodal displacements vectors.

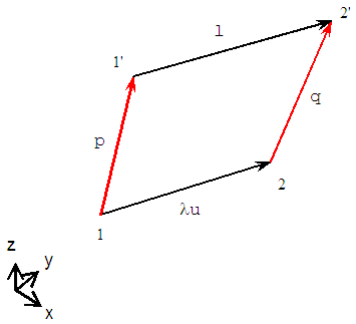

Figure 3.3. Side displacement

$$\left.\begin{aligned} \vec{l}_i &= \lambda \hat{u}_i + \vec{q}_i - \vec{p}_i \\ \vec{z}_i &= \frac{\vec{q}_i - \vec{p}_i}{\lambda_i} \end{aligned}\right\} \vec{l}_i = \lambda_i(\vec{u}_i + \vec{z}_i) \tag{3.12}$$

$$\begin{aligned} \left|\vec{l}\right|_i^2 = \boldsymbol{\lambda_i^2}(\vec{\boldsymbol{u}}_i + \vec{\boldsymbol{z}}_i)^2 = \boldsymbol{\lambda_i^2}(\vec{\boldsymbol{u}}_i \cdot \vec{\boldsymbol{u}}_i + \vec{\boldsymbol{z}}_i \cdot \vec{\boldsymbol{z}}_i + \mathbf{2}\vec{\boldsymbol{u}}_i \cdot \vec{\boldsymbol{z}}_i) = \boldsymbol{\lambda_i^2}(\mathbf{1} + \vec{\boldsymbol{z}}_i \cdot \vec{\boldsymbol{z}}_i + \mathbf{2}\vec{\boldsymbol{u}}_i \cdot \vec{\boldsymbol{z}}_i) \\ = \boldsymbol{\lambda_i^2}(\mathbf{1} + \boldsymbol{\delta_i}) \end{aligned} \tag{3.13}$$

$$\boldsymbol{\delta_i} = \mathbf{2}\vec{\boldsymbol{u}}_i \cdot \vec{\boldsymbol{z}}_i + \vec{\boldsymbol{z}}_i \cdot \vec{\boldsymbol{z}}_i \tag{3.14}$$

The Green strain along the side of the element and its derivatives with respect to the nodal displacements can be written as follows:

$$\varepsilon_i = \frac{\left|\vec{l}\right|_i^2 - \lambda_i^2}{2\lambda_i^2} = \frac{\delta_i}{2} \tag{3.15}$$

$$\frac{\partial \varepsilon_i}{\partial p_i} = -\frac{1}{\lambda_i}(\vec{u}_i + \vec{z}_i) \tag{3.16}$$

$$\frac{\partial \varepsilon_i}{\partial q_i} = +\frac{1}{\lambda_i}(\vec{u}_i + \vec{z}_i) \tag{3.17}$$

The displacements vectors at the nodes are $\vec{x}^1 = (x_1^1, x_2^1, x_3^1), \vec{x}^2 = (x_1^2, x_2^2, x_3^2)$ and $\vec{x}^3 = (x_1^3, x_2^3, x_3^3)$. And the gradient of the strain components

$$\nabla\varepsilon_i = \left\{\frac{\partial \varepsilon_i}{\partial x_1^1}, \frac{\partial \varepsilon_i}{\partial x_2^1}, \frac{\partial \varepsilon_i}{\partial x_3^1}, \frac{\partial \varepsilon_i}{\partial x_1^2}, \frac{\partial \varepsilon_i}{\partial x_2^2}, \frac{\partial \varepsilon_i}{\partial x_3^2}, \frac{\partial \varepsilon_i}{\partial x_1^3}, \frac{\partial \varepsilon_i}{\partial x_2^3}, \frac{\partial \varepsilon_i}{\partial x_3^3}\right\} \tag{3.18}$$

For each side of the triangular element the gradient of the strain will be:

Side 1:

$$\vec{z}_1 = \frac{\vec{x}^3 - \vec{x}^2}{\lambda_1} \qquad \delta_1 = 2\hat{u}_1 \cdot \vec{z}_1 + |\vec{z}_1|^2 \qquad \varepsilon_1 = \frac{\delta_1}{2} \tag{3.19}$$

$$\nabla\varepsilon_1 = \frac{1}{\lambda_1}\begin{pmatrix} 0 \\ 0 \\ 0 \\ -(u_1^1 - z_1^1) \\ -(u_2^1 - z_2^1) \\ -(u_3^1 - z_3^1) \\ +(u_1^1 - z_1^1) \\ +(u_2^1 - z_2^1) \\ +(u_3^1 - z_3^1) \end{pmatrix} \tag{3.20}$$

Side 2:

$$\vec{z}_2 = \frac{\vec{x}^1 - \vec{x}^3}{\lambda_2} \qquad \delta_2 = 2\hat{u}_2 \cdot \vec{z}_2 + |\vec{z}_2|^2 \qquad \varepsilon_2 = \frac{\delta_2}{2} \tag{3.21}$$

$$\nabla\varepsilon_2 = \frac{1}{\lambda_2}\begin{pmatrix} +(u_1^2 - z_1^2) \\ +(u_2^2 - z_2^2) \\ +(u_3^2 - z_3^2) \\ 0 \\ 0 \\ 0 \\ -(u_1^2 - z_1^2) \\ -(u_2^2 - z_2^2) \\ -(u_3^2 - z_3^2) \end{pmatrix} \tag{3.22}$$

Side 3:

$$\vec{z}_3 = \frac{\vec{x}^2 - \vec{x}^1}{\lambda_3} \qquad \delta_3 = 2\hat{u}_3 \cdot \vec{z}_3 + |\vec{z}_3|^2 \qquad \varepsilon_3 = \frac{\delta_3}{2} \tag{3.23}$$

$$\nabla\varepsilon_3 = \frac{1}{\lambda_3}\begin{pmatrix} -(u_1^3 - z_1^3) \\ -(u_2^3 - z_2^3) \\ -(u_3^3 - z_3^3) \\ +(u_1^3 - z_1^3) \\ +(u_2^3 - z_2^3) \\ +(u_3^3 - z_3^3) \\ 0 \\ 0 \\ 0 \end{pmatrix} \tag{3.24}$$

Now it is possible to calculate the derivative of the strain energy with respect to an arbitrary displacement component x_i.

$$\frac{\partial\phi}{\partial x_i} = \int_V \boldsymbol{H\varepsilon}\frac{\partial\boldsymbol{\varepsilon}}{\partial x_i}\, dV \tag{3.25}$$

Once calculated the gradient of the potential strain energy it is necessary to solve the equilibrium condition. This procedure will be exposed at the section 3.5 of this chapter.

Finally, it is possible to write the main stresses for an element as follows:

$$\boldsymbol{\varepsilon} = \boldsymbol{C}\bar{\boldsymbol{\varepsilon}}$$

$$\begin{pmatrix}\varepsilon_1\\ \varepsilon_2\\ \varepsilon_3\end{pmatrix} = \begin{pmatrix}\cos^2\theta_1 & \sin^2\theta_1 & \sqrt{2}\cos\theta_1\sin\theta_1\\ \cos^2\theta_2 & \sin^2\theta_2 & \sqrt{2}\cos\theta_2\sin\theta_2\\ \cos^2\theta_3 & \sin^2\theta_3 & \sqrt{2}\cos\theta_3\sin\theta_3\end{pmatrix}\begin{pmatrix}\varepsilon_{xx}\\ \varepsilon_{yy}\\ \sqrt{2}\varepsilon_{xy}\end{pmatrix} \tag{3.26}$$

$$\bar{\boldsymbol{\sigma}} = \bar{\boldsymbol{H}}\bar{\boldsymbol{\varepsilon}} \rightarrow \begin{pmatrix}\sigma_{\boldsymbol{xx}}\\ \sigma_{\boldsymbol{yy}}\\ \sqrt{2}\sigma_{\boldsymbol{xy}}\end{pmatrix} = \frac{E}{1-\nu^2}\begin{pmatrix}1 & \nu & 0\\ \nu & 1 & 0\\ 0 & 0 & 1-\nu\end{pmatrix}\begin{pmatrix}\varepsilon_{xx}\\ \varepsilon_{yy}\\ \sqrt{2}\varepsilon_{xy}\end{pmatrix} \tag{3.27}$$

$$\bar{\boldsymbol{\sigma}} = \boldsymbol{C}^T\boldsymbol{\sigma} \rightarrow \begin{pmatrix}\sigma_{\boldsymbol{xx}}\\ \sigma_{\boldsymbol{yy}}\\ \sigma_{\boldsymbol{xy}}\end{pmatrix} = \boldsymbol{C}^{\boldsymbol{T}}\begin{pmatrix}\sigma_{\mathbf{1}}\\ \sigma_{\mathbf{2}}\\ \sigma_{\mathbf{3}}\end{pmatrix} \tag{3.28}$$

$$\begin{aligned}\Delta = &\left(\sigma_{\boldsymbol{xx}} - \sigma_{\boldsymbol{yy}}\right)^2 + 4\sigma_{xy}^2\\ &= \sigma_1^2 + \sigma_2^2 + \sigma_3^2 + 4\sigma_1\sigma_2\left(cos^2\alpha_3 - \frac{1}{2}\right) + 4\sigma_1\sigma_3\left(cos^2\alpha_2 - \frac{1}{2}\right)\\ &+ 4\sigma_2\sigma_3\left(cos^2\alpha_1 - \frac{1}{2}\right)\end{aligned} \tag{3.29}$$

$$\sigma' = \frac{\left(\sigma_{xx} + \sigma_{yy}\right) \mp \sqrt{\Delta}}{2} = \frac{\sigma_1 + \sigma_2 + \sigma_3 \mp \sqrt{\Delta}}{2} \tag{3.30}$$

3.3 Structural modelling of cables

In the rigging of a sailboat there are many ropes and cables: the main sheet, the jib sheet, the forward stay, the back stay and the shrouds. All these elements can be modelled using bar finite elements. These elements can only transmit axial forces, it means that the nodes of bar elements only have translational degrees of freedom. Therefore it is possible to discretize a cable with a set of articulated bar elements, the truss resulting of this junction of bar elements will be a cable that only transmit traction forces.

The model implemented in this work was presented by Arcaro(Arcaro, 2004(b)). It includes a total Lagrangian description using the standard strain definition and assumes an elastic material.

The cables are discretized with linear elements of two nodes, where the strain is assumed constant along the element and the material is considered to be homogeneous and isotropic.

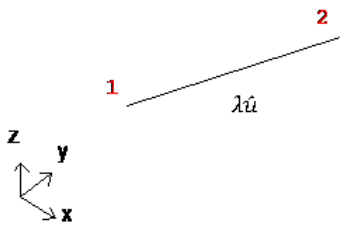

Figure 3.4. Bar element

The $\lambda\hat{u}$ vector represents the cable element in a configuration with zero nodal displacements, where $\hat{u}$ corresponds to a unity vector describing the direction of the element and the scalar λ represents the distance between the two nodes of the element in this configuration. For the deformed element, the vector $\boldsymbol{l}$ represents the element in its deformed configuration, and the vectors $\boldsymbol{p}$ and $\boldsymbol{q}$ represents the nodal displacement vectors.

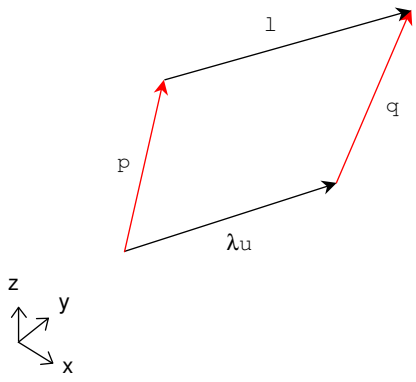

Figure 3.5. Deformed cable element

The deformed length can be found relating these vectors:

$$\lambda \boldsymbol{u} + \boldsymbol{q} - \boldsymbol{l} - \boldsymbol{p} = 0 \rightarrow \boldsymbol{l} = \lambda \boldsymbol{u} + \boldsymbol{q} - \boldsymbol{p} \quad 3.31$$

$$\boldsymbol{z} = \frac{\boldsymbol{q} - \boldsymbol{p}}{\lambda} \rightarrow \boldsymbol{l} = \lambda(\boldsymbol{u} + \boldsymbol{z}) \quad 3.32$$

$$\delta = 2\boldsymbol{u}^T\boldsymbol{z} + \boldsymbol{z}^T\boldsymbol{z} \quad 3.33$$

$$\|\boldsymbol{l}\| = \lambda\sqrt{1 + \delta} \quad 3.34$$

The cables used in our structure will be pre-stressed, result of the stress applied by the ship crew to trim the sail. This action of the crew results in a cable strain. The potential strain energy and its gradient $\nabla\phi(\vec{x})$ can be calculated as is shown in the following.

Imposing a constant stress σ_0 in a cable element, and considering a linear stress strain relationship, the potential strain energy and its gradient can be written as follows, being A the area of the cable.

$$\phi = A\sigma_0\lambda\sqrt{1 + \delta} \quad 3.35$$

$$\frac{\partial\phi}{\partial p_i} = -A\sigma_0\frac{l_i}{\|\boldsymbol{l}\|} \quad 3.36$$

$$\frac{\partial\phi}{\partial q_i} = +A\sigma_0\frac{l_i}{\|\boldsymbol{l}\|} \quad 3.37$$

The gradient can be interpreted as internal forces, with constant modulus, acting on the nodes of the element.

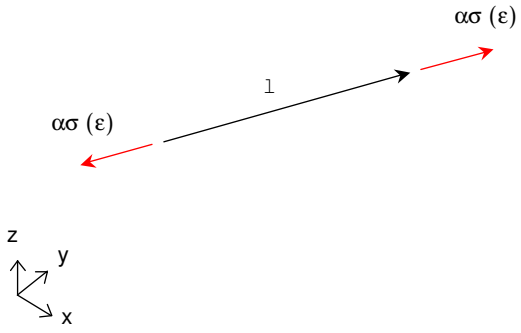

Figure 3.6. Internal forces

3.4 Structural modelling of beams

The rigging of a sailboat is basically composed of the mast, spreaders and the boom. As explained above, these elements will be modelled using beam element.

A beam element used is a two node element with six degrees of freedom at each node. The three dimensional beam element resists axial force, transverse shear force in each one of two normal directions, bending in each principal axis of the cross section, and torque in the longitudinal axis of the member. The displacements and rotations produced by the different actions are represented in the following figure:

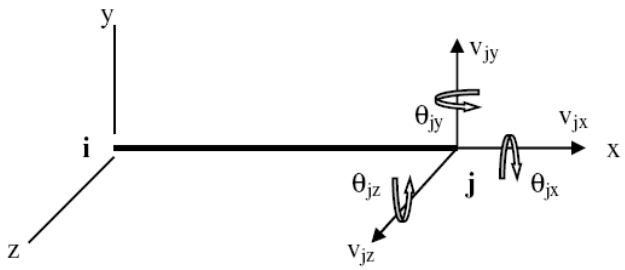

Figure 3.7. Beam element with six degrees of freedom at each node

The strain energy of a beam can be written as:

$$\phi = \frac{1}{2} \sum_{\boldsymbol{elements}} \boldsymbol{x}^T \boldsymbol{k} \boldsymbol{x} \tag{3.38}$$

Where $\boldsymbol{x}$ is the vector of nodal displacements, translations and rotations in the reference system of the element. And $\boldsymbol{k}$ is the element stiffness matrix for a two nodes beam element with six degrees of freedom. $\boldsymbol{k}$ is derived by combining the stiffness constants of a beam under pure bending, a truss element, and a torsion bar:

$$k = \begin{pmatrix} \frac{AE}{L} & 0 & 0 & 0 & 0 & 0 & -\frac{AE}{L} & 0 & 0 & 0 & 0 & 0 \\ 0 & \frac{12EI_z}{L^3} & 0 & 0 & 0 & \frac{6EI_z}{L^2} & 0 & -\frac{12EI_z}{L^3} & 0 & 0 & 0 & \frac{6EI_z}{L^2} \\ 0 & 0 & \frac{12EI_y}{L^3} & 0 & -\frac{6EI_y}{L^2} & 0 & 0 & 0 & -\frac{12EI_y}{L^3} & 0 & -\frac{6EI_y}{L^2} & 0 \\ 0 & 0 & 0 & \frac{GJ}{L} & 0 & 0 & 0 & 0 & 0 & -\frac{GJ}{L} & 0 & 0 \\ 0 & 0 & -\frac{6EI_y}{L^2} & 0 & \frac{4EI_y}{L} & 0 & 0 & 0 & \frac{6EI_y}{L^2} & 0 & \frac{2EI_y}{L} & 0 \\ 0 & \frac{6EI_z}{L^2} & 0 & 0 & 0 & \frac{4EI_z}{L} & 0 & -\frac{6EI_z}{L^2} & 0 & 0 & 0 & \frac{2EI_z}{L} \\ -\frac{AE}{L} & 0 & 0 & 0 & 0 & 0 & \frac{AE}{L} & 0 & 0 & 0 & 0 & 0 \\ 0 & -\frac{12EI_z}{L^3} & 0 & 0 & 0 & -\frac{6EI_z}{L^2} & 0 & \frac{12EI_z}{L^3} & 0 & 0 & 0 & -\frac{6EI_z}{L^2} \\ 0 & 0 & -\frac{12EI_y}{L^3} & 0 & \frac{6EI_y}{L^2} & 0 & 0 & 0 & \frac{12EI_y}{L^3} & 0 & \frac{6EI_y}{L^2} & 0 \\ 0 & 0 & 0 & -\frac{GJ}{L} & 0 & 0 & 0 & 0 & 0 & \frac{GJ}{L} & 0 & 0 \\ 0 & 0 & -\frac{6EI_y}{L^2} & 0 & \frac{2EI_y}{L} & 0 & 0 & 0 & \frac{6EI_y}{L^2} & 0 & \frac{4EI_y}{L} & 0 \\ 0 & \frac{6EI_z}{L^2} & 0 & 0 & 0 & \frac{2EI_z}{L} & 0 & -\frac{6EI_z}{L^2} & 0 & 0 & 0 & \frac{4EI_z}{L} \end{pmatrix} \tag{3.39}$$

$$\boldsymbol{x} = \begin{pmatrix} v_{1x} \\ v_{1y} \\ v_{1z} \\ \theta_{1x} \\ \theta_{1y} \\ \theta_{1z} \\ v_{2x} \\ v_{2y} \\ v_{2z} \\ \theta_{2x} \\ \theta_{2y} \\ \theta_{2z} \end{pmatrix} \quad 3.40$$

The equilibrium configuration must satisfy the minimum potential energy condition.

$$\frac{\partial \phi}{\partial \boldsymbol{x}} = \sum_{elements} \boldsymbol{k} \cdot \boldsymbol{x} - \boldsymbol{f} = \boldsymbol{0} \quad 3.41$$

In the rigging of a sailboat, we can model the mast, the boom and spreaders with beam elements. However, the joint of the boom to the mast allows the boom to rotate around the mast, this joint is similar to a hinge, so then it is necessary to release or disconnect this degree of freedom.

In the absence of a release, beam elements are rigidly connected to one another at a shared node, so it is necessary be able to release degrees of freedom between two beam elements. The method to release the degrees of freedom at a joint is presented in the reference (Cook, 2002) and is explained in the following section.

3.4.1 Release of a degree of freedom

A release is a lack of complete connection between nodes that would be usually fully connected. The mast and the boom are connected at node A, with a hinge, as the boom is able to rotate around the mast

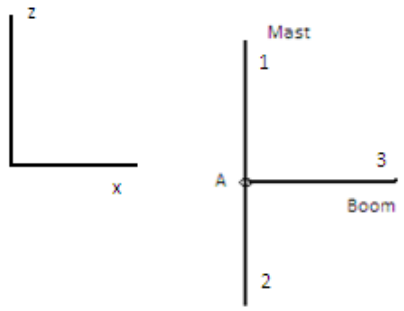

Figure 3.8. Release Implementation

Elements 1 and 2 share the same nodal rotation θ_{iz}, but element 3 does not share the same nodal rotation θ_{iz}, as this would imply a rigid connection rather than a hinge.

One possible way to treat the hinge in A is to define two separate nodes at A, one in the mast and one in the boom, although they have the exact same location. Thus there is a total of twelve degrees of freedom at A. Afterwards, the translational degree of freedom of the two nodes are coupled by means of a constrain technique.

Another procedure to model the hinge is to condense θ_{iz} in A in the element 3, then fill the row and column just condensed with zeros so that the boom does not contribute to the rotational stiffness of the structure.

The algorithm presented in the reference (Cook, 2002) to produce the condensed stiffness matrix has been adapted to introduce the capability of release a degree of freedom in the software presented at this work.

3.5 Equilibrium configuration

The flow applys external loads on the structure, and these loads cause the displacements of the nodes. Nodes move until achieve a stable equilibrium configuration. The stable equilibrium configuration of the structure is calculated from the minimum condition of the total potential energy. For the vector of the nodal displacements $\boldsymbol{x}$ and the vector of the flow forces action on the nodes $\boldsymbol{f}$ obtained from the solution of the fluid flow, and the internal potential energy $\phi(\boldsymbol{x})$, the total potential energy is:

$$E_{TOT} = \sum_{elements} \phi(\boldsymbol{x}) - \boldsymbol{f}^T \boldsymbol{x} \qquad 3.42$$

And thus the equilibrium condition is

$$\sum_{elements} \nabla\phi\,(\boldsymbol{x}) - \boldsymbol{f} = 0 \qquad 3.43$$

For the equilibrium condition it is necessary calculate the gradient of the potential strain energy of each element. In previous sections it has been explained the procedure to calculate this gradient for each type of finite element used (cables, beams and membrane elements). These gradients are expressed in terms of the nodal displacements and rotations, defining the system of equations to be solved every iteration step.

This non-linear system of equations is solved in this work by using a Quasi Newton iterative procedure. The computer code implemented uses the limited memory BFGS to tackle large scale problems as described by Nocedal and Wright (Nocedal, 1999). It also employs a line search procedure as described by Gill and Murray (Gill, 1974).

3.5.1 Quasi Newton Algorithm

Considering $h(x)$ the function to be minimized, the Quasi Newton Algorithm can be written as follows:

Given starting point $\boldsymbol{x}_0$*, convergence tolerance* $\varepsilon > 0$.

Inverse Hessian approximation $\boldsymbol{H}_0 = \boldsymbol{I}$

$k = 0$

While $\|\nabla h_k\| > \varepsilon$

Compute search direction

$$p_k = -\boldsymbol{H}_k \nabla h_k$$

Set $x_{k+1} = x_k + \alpha_k p_k$*, where* α_k *is computed from a line search procedure to satisfy the Wolfe*[9] *condition.*

Define $s_k = x_{k+1} - x_k$, $y_k = \nabla h_{k+1} - \nabla h_k$ *and* $\rho_k = \frac{1}{y_k^T s_k}$

Compute $\boldsymbol{H}_k = (\boldsymbol{I} - \rho_k s_k y_k^T)(\boldsymbol{I} - \rho_k s_k y_k^T) + \rho_k s_k s_k^T$

$k \to k + 1$

end (while)

The stopping criteria of the iterative algorithm will be $\varepsilon = mtol$[10] $\cdot \nabla h_0$, following some references (Andrei, 2008) (Nocedal, 1999), where the limited memory BFGS is used to minimize a function. It is important to consider that the FEA structural solver must interact with the flow solver. Therefore the FEA iterative procedure has to be embedded into the global iteration. So, following Graf and Renzsch (Graf, 2006) , who used the same minimization scheme to find the equilibrium configuration of a spinnaker, the equilibrium configuration Eq. 3.43 can be solved to a small residual. Different numerical tests (Graf, 2006) have shown that it is sufficient for practical cases to decrease the residual by one order of magnitude per global iteration, so then would be sufficient to take $\varepsilon = 0.1 \cdot \nabla h_0$.

---

[9] The sufficient decrease and curvature conditions are known collectively as the Wolfe conditions

$h(x_k + \alpha_k p_k) \leq h(x_k) + c_1 \alpha \nabla h_k^T p_k; \nabla h(x_k + \alpha_k p_k)^T p_k \geq c_2 \nabla f_k^T p_k; 0 < c_1 < c_2 < 1$

For more information to consult Chapter 3 in (Nocedal, 1999).

[10] This parameter must be indicated by the user. All the required indications are in appendix B in the GUI

3.5.2 Iteration scheme

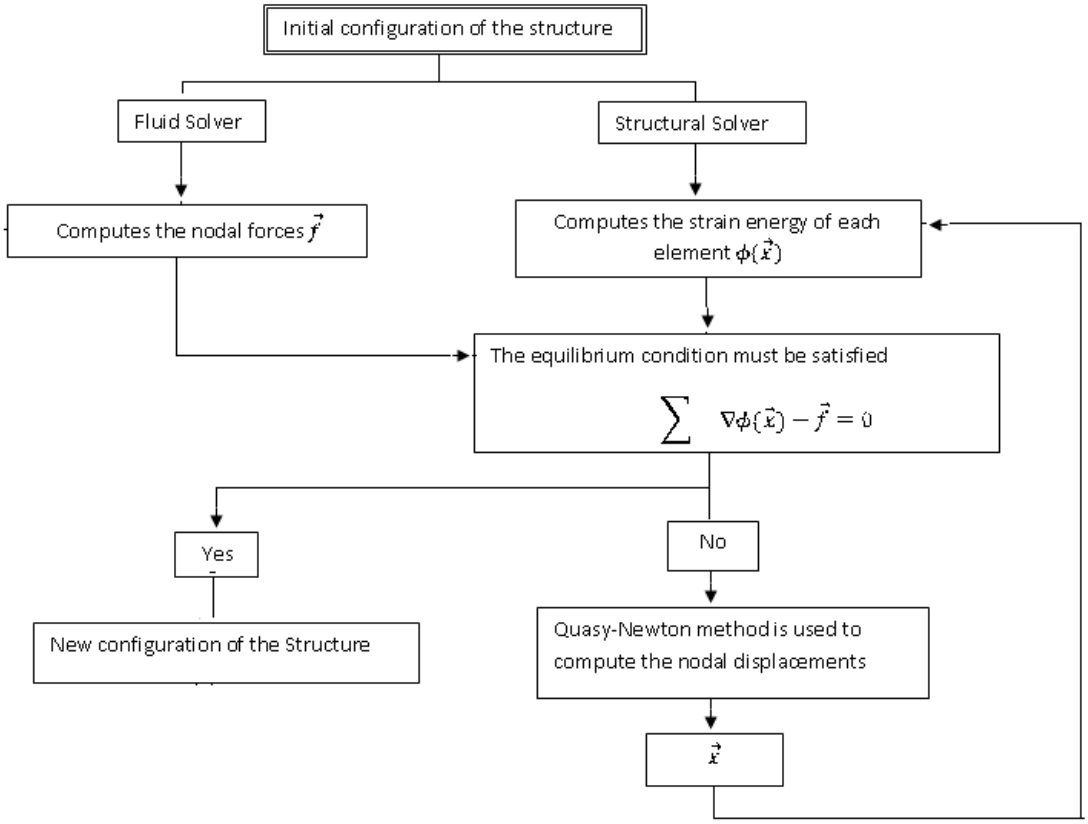

Figure 3.9. Iterative procedure for the structural step

3.6 Validation examples

Each type of finite element used to model the different elements of our structure is validated in this section. Simple problems are calculated with the 'FEA solver' implemented in this work. The obtained results are compared with analytical data when available, or with results obtained from the commercial FEA program RamSeries[11].

3.6.1 Validation of the membrane element

3.6.1.1 Hencky's Problem

The studied case considers the deformation of an initially flat, circular membrane with fixed edges and loaded with a constant pressure.

The results obtained with the membrane model implemented in this work, are presented in the following figure.

The geometric and mechanical properties of the membrane are:

[11] RamSeries is a three-dimensional structural analysis environment based on the Finite Element Method. (see http://www.compassis.com for further information)

$$R = 0.1425m \quad E \cdot t = 311488\frac{N}{m} \quad \nu = 0.34 \quad P = 100kPa$$

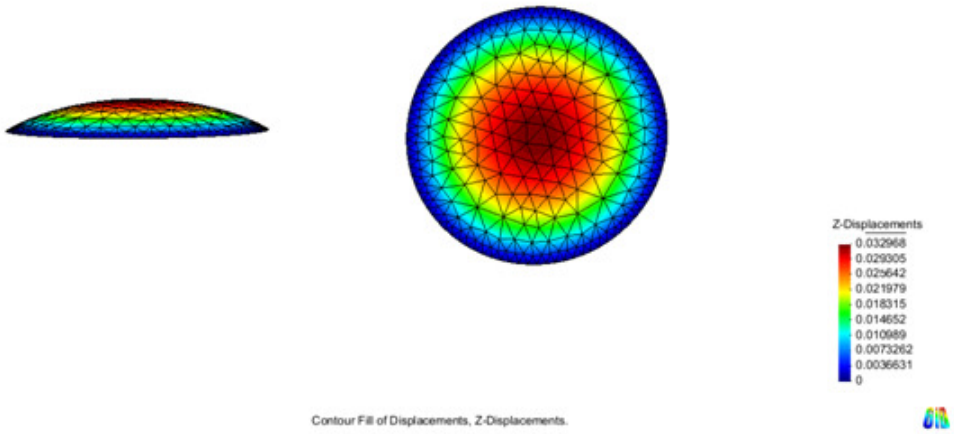

Figure 3.10. Membrane deformation

The maximum deformation of the membrane is found in the centre and is of 0.0330m. This value agrees with the maximum deformation obtained by Pauletti **(Pauletti, 2005)**, that was 0.0331m.

3.6.1.2 Membrane under self weight

This problem finds the equilibrium position of a membrane under self weight. The membrane has a "V" shape initial configuration.

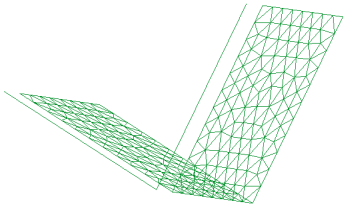

Figure 3.11. Membrane in V

The top edges are fixed in all the directions and the lateral edges have restricted the movement in the transverse direction. The material properties are: $E = 5.01e6\ N/m^2$, $t = 0.001m$, $\rho = 100kg/m^3$, $\nu = 0$, $A = 70.7106m^2$, so the total weight of the membrane is 69.36 N.

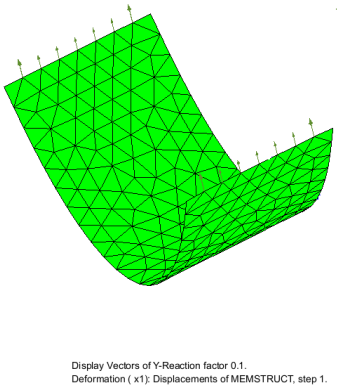

Figure 3.12. Deformed membrane

The sum of the reactions in the nodes of the top edges is exactly the weight of the membrane, as expected.

3.6.2 Validation of the structural model for cables

3.6.2.1 Cable loaded with punctual load

This example consists in the simulation of a cable of length L with a punctual load in its centre. In the equilibrium, the length of the cable will change. The maximum vertical displacement u will be found at the centre and the new length should be $\sqrt{L^2 + 4u^2}$.

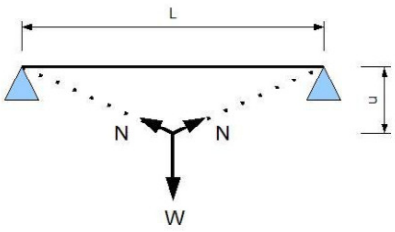

Figure 3.13.Cable with ends fixed

The stress in the cable is $N(u) = \frac{EA}{L}\left(\sqrt{L^2 + 4u^2} - \mathrm{L}\right)$, and the sum of the vertical reactions at the support that have to equilibrate the external force W is $f(u) = 4\frac{EA}{L}\left(1 - \frac{L}{\sqrt{L^2+4u^2}}\right) \cdot u.$

Considering a cable length of $L = 1m$, with an area $A = 0.001\, m^2$, a Young modulus of $E = 5.0e6\, N/m^2$ and a given vertical displacement of $u = 0.3m$,the analytical solution gives $f(0.3) = 855.04N$ and $N(0.3) = 830.95N$.

For the validation with the implemented solver, a punctual load of 855.04 N is applied in the centre of the cable, which has been discretized into twenty bar

elements. The axial force obtained is $N = 830.77N$ and the displacement of the center is $u = 0.29985m$.

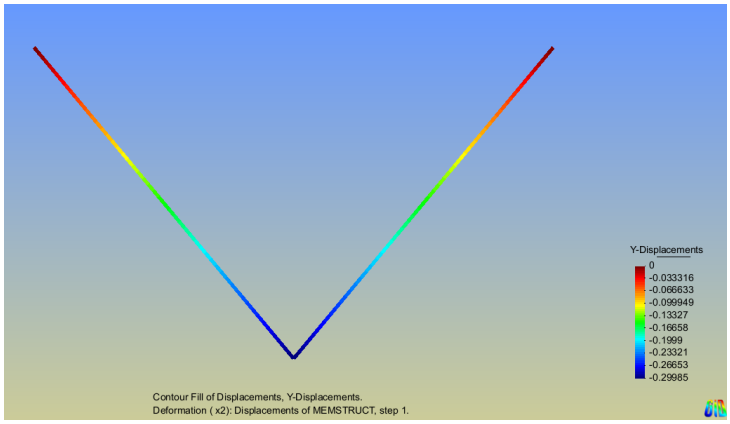

Figure 3.14. Displacement for a cable with a punctual load in the center.

3.6.2.2 Cable loaded with its self weight

A cable with ends fixed has been loaded with its own, its weight. Initially the cable has V form, and the expected deformation is a U form and the reactions in ends must be equal to the weight of the cable.

The properties of the material are $E = 5.01e6\frac{N}{m^2}$ and $\rho = \frac{100kg}{m^3}$. The length of the cable $L = 14.1421m$ and the area of the cable $A = 0.0005m^2$. Considering the density of the material and the dimensions of the cable, the weight of the cable is $P = 69.36N$.

The cable has been discretized into twenty-two bar elements.

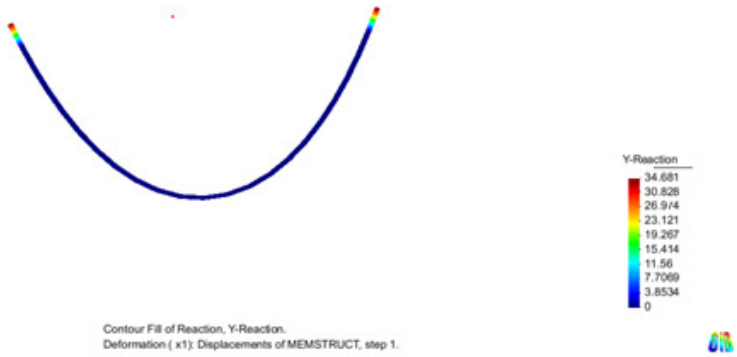

Figure 3.15. Deformed cable with distributed load

The reactions in each end are 34.681N, and the total reaction is $R = 2 \cdot 34.681 = 69.372N$, therefore the results are the expected.

3.6.3 Validations of beam element

3.6.3.1 Vertical loaded cantilever

The implementation made of the beam elements has been validated with the simulation of a cantilever vertical loaded with a horizontal load. The beam cross section is shown in the following figure. The problem has the following parameters as total length $L = 14\,m$, $A = 21.36cm^2$, $I_x = 5.8 \cdot 10^{-6}m^4$, $I_y = 1.35 \cdot 10^{-5}m^4$, $J = 1.9 \cdot 10^{-5}m^4$, $G = 3.946 \cdot 10^{10}N/m^2$ and $E = 1.105 \cdot 10^{11}N/m^2$.

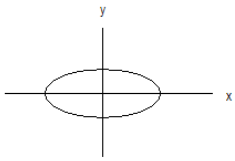

Figure 3.16. Beam section

The lowest node has restricted translations and rotations in all the directions, and the top node has a punctual load of 500 N applied in the x directions.

It is possible calculate the displacement of the top node with the analytical expression $Y_{max.} = \frac{F \cdot L^3}{3EI_y} = \frac{500 \cdot 14^3}{3 \cdot 1.105 \cdot 10^{11} \cdot 1.35 \cdot 10^{-5}} = 30.7cm$.

The results obtained with the implementation of this work are shown below.

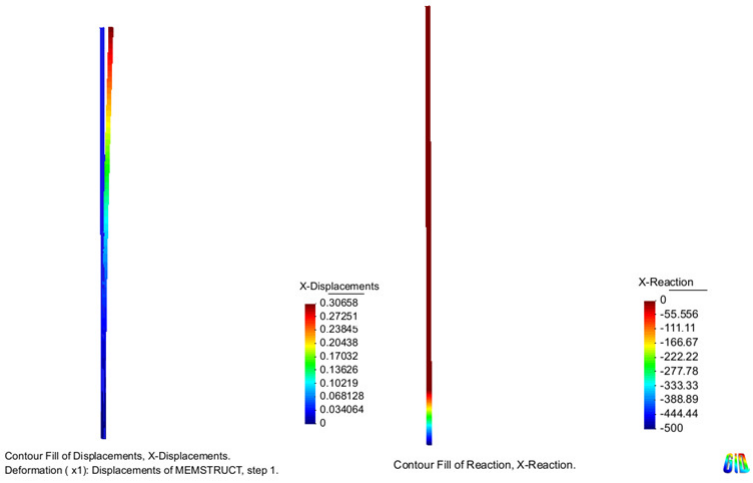

Figure 3.17. Results for a projecting beam with a punctual load

The displacement of the top node with the implemented model is $30.6cm$ and the reaction is $R = -500N$, which are the expected results.

3.6.3.2 Validation of a hinge joint

To validate the procedure used to simulate the hinge between elements, the results obtained with the developed code have been compared with the results provided by the commercial solver RamSeries.

The structure used to perform this comparison is the one shown in the Figure 3.18

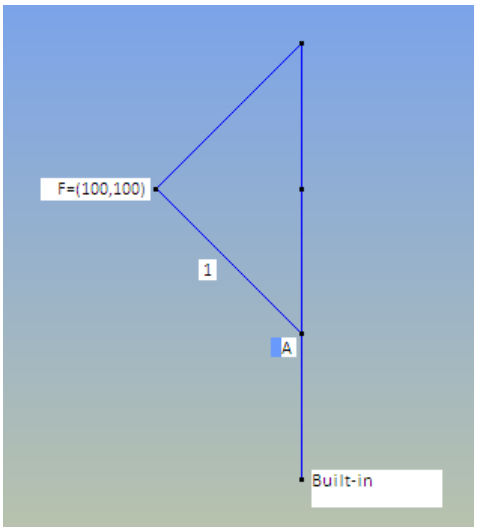

Figure 3.18. Element with a hinge at node A. Element 1 has the rotational d.o.f. released of the vertical element.

The beam element 1 has the rotational degree of freedom released in the node in contact with the vertical element (A). The node of the structure base has the displacements and the rotations restricted to zero. There is a force applied to the indicated node.

In the following, the results of the calculation are presented.

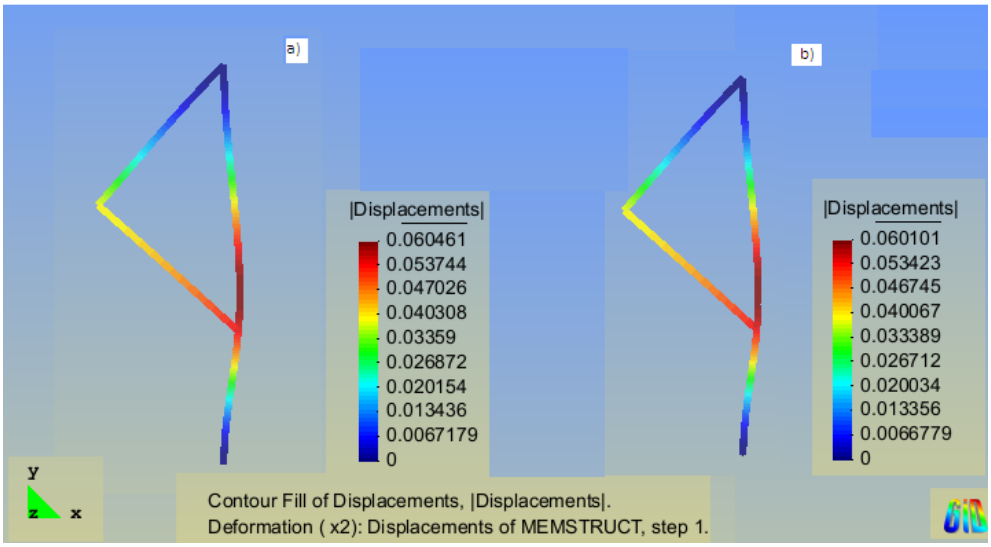

Figure 3.19. a) This work's result b) RamSeries's result

Figure 3.19 shows that the results of the two solvers are practically equal. Therefore, considering that RamSeries is a validated code, we can affirm that our hinge implementation can be considered as validated.

3.7 Conclusions

Three types of structural elements have been implemented, cables, beams and membranes, to simulate the different parts of our structure, sails and rigging.

The minimization of the potential energy is solved by a BFGS to compute the equilibrium state of the structure submitted to the aerodynamic loads.

The structural model implemented in this work has been validated with different examples, obtained satisfactory results. So, It is possible to conclude that with this 'FEA solver' will be able to compute the response of the sails and rigging to the wind action.

4 Fluid-Structure Interaction

A complete modelling of sail's steady equilibrium involves a fluid/structure analysis. The presence of the sail modifies the flow, whilst the latter applies aerodynamic forces on the sail and modifies its geometry.

The consideration of the external flow has been made at the second chapter, and the Fluid Solver to compute this flow has been explained. The analysis of the mechanical model for the sails and the rigging has been made at the third chapter, and the Structural Solver to compute the response of the structure to external actions has been explained. This chapter will analyse the integration of those algorithms to develop a coupled fluid-structure solver. Fluid Solver and Structural Solver use a different grid for modelling the sails, so the relation and interaction between the two grids will be first presented. The iterative scheme developed for this purpose will be presented. The application examples of the algorithm will be introduced in the following chapters.

4.1 Introduction

The nature of the fluid-structure interaction method we envisage is iterative: starting from an initial geometry, the flow forces are calculated using the Fluid Solver. From the flow forces, sail deflections are calculated. The flow simulation is repeated with deflected geometry, and the structural calculation is repeated in turn with modifies flow forces.

The structural solver of the algorithm is based on the finite element method (FEM) and the flow is calculated by solving the potential flow equations using a Vortex Lattice Method (VLM) approach. Jackson (Jackson, 1985), Schoop (Schoop, 1990), Muttin (Muttin, 1991), Fukasawa and Katori (Fukasawa, 1993) dealt with the numerical problem by coupling the finite element method with a Vortex Lattice Method. Schoop and Bessert (Schoop, 2001) mention that one of the reasons for the poor convergence of the FEM-VLM is the fact of using the same discretization scheme for the FEM and VLM. For that reason, in this work, different discretization schemes have been selected for FEM and VLM solvers.

The first step is the adjustment of the geometry to the trim parameters. In order to communicate the fluid-structure interaction with the trim parameters in real time, a TCL interface has been implemented into the coupled solver.

4.2 Meshes and their interaction

The selected VLM, to compute the flow loads in the sails, uses quadrilateral elements. And the selected FEM, to compute the response of the sails to the flow loads, uses triangular elements. In order to fulfil the requirement of both methods, a structured mesh of quadrilateral elements will be generated and these

quadrilateral[12] elements will be split, internally by the program, in triangular elements. This procedure allows that the two meshes have coincident nodes, in order to facilitate the data transfer between the two meshes.

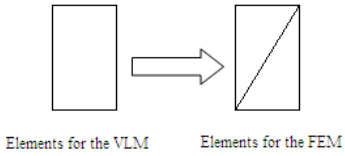

Figure 4.1. Mesh for the Fluid Solver and mesh for the Structural Solver

This fluid-structure interaction method developed is iterative: starting from an initial geometry, the flow forces are calculated, then sail displacements are evaluated from the flow forces, and the flow simulation is repeated with the updated geometry and the structural calculation is repeated in turn with the updated flow forces, until convergence is achieved. So then, the grid is modified every fluid-structure iteration. Lagrangian advance techniques are used to fit the sail grid surface used for the flow simulation from the deformed sail. The Lagrangian updating of the grid is done automatically by the algorithm as hidden procedure for the user.

The grid updating is inserted into the iterative scheme as follows:

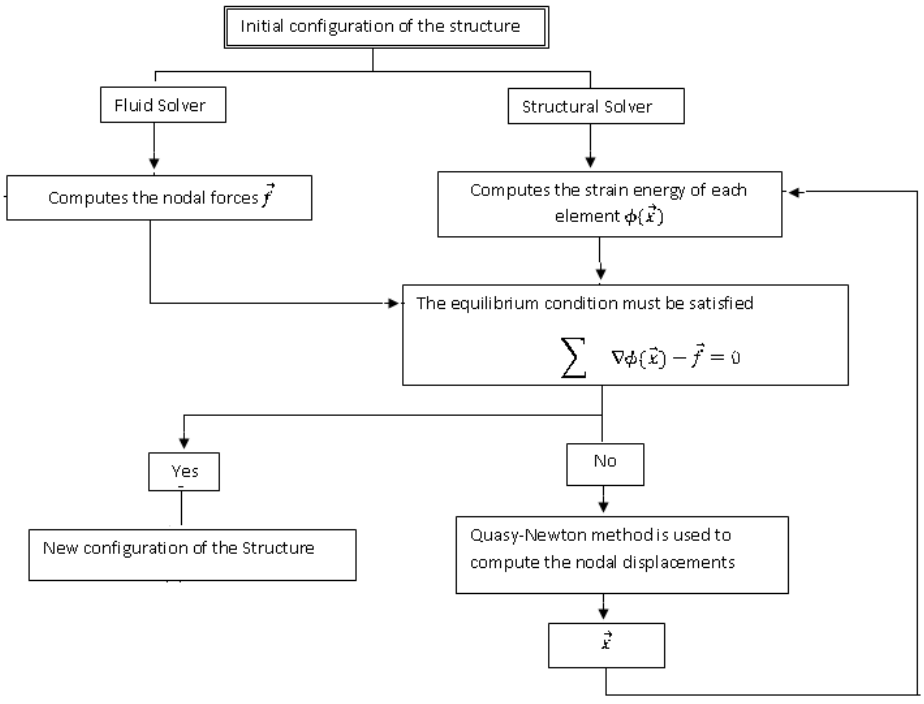

Figure 4.2. Introduction in the iterative process of a morphing grid step

[12] The structured mesh of quadrilateral elements will be generated by the user of *Sailing*. This procedure is explained in the GUI (Appendix B).

4.3 The iterative process

As stated in the previous sections, a complete modelling of sail's steady equilibrium involves a fluid/structure analysis. The nature of the fluid-structure interaction method we envisage is iterative: starting from an initial geometry the flow forces and then, rigging and sails displacements are calculated. The flow simulation is repeated with the updated geometry, the structural calculation is repeated in turn with modifies flow forces, and the iteration process is repeated until convergence is achieved.

The interaction method presented by Renzsch et al. (Renzsch, 2008) has been followed in this work and, an embedded iteration scheme is used to achieve convergence of the iterative procedure of the potential flow solution process as well as the solution of the non-linear system of equations to calculate equilibrium in the structural code:

- The potential flow calculation is carried out assuming fully rigid sails.
- Flow forces are applied to the vertices of the structure.
- The displacement of the sail surface is calculated every iteration step, for a given set of forces.
- The shape of the sail is updated every iteration step.
- This procedure is repeated until the convergence criteria are achieved.

The first step of the calculation is the application of the trim parameters to the basic structure, as initial loads and boundary conditions. These parameters can be modified during execution by using a TCL[13] interface. The interface can be connected with a network of sensors located at the rigging, to obtain the trim parameters in real time. Both the communication interface and the network of sensors will be explained in the next chapters.

Once the trim parameters had been applied to the basic structure, an explicit embedded algorithm is executed to couple the Fluid Solver and the Structural Solver. The external flow is computed by taking into account the configuration of the sail (aerodynamic step). Once the flow field is given the new configuration of the sail is computed (structural step). This leads to a new external flow, due to the updated geometry of the sail and so on; the sequence of aerodynamic/structural steps is repeated until the stopping condition is satisfied.

If the difference between the nodal forces computed at each Fluid Solver iteration is less than a tolerance, enough to consider than the change in the geometry will be small comparing with the previous step, then the stopping criteria will be satisfied. Being k and $k+1$ two consecutive iterations between the Fluid Solver and the Structural Solver, the stopping criteria will be:

[13] TCL (Tool Command Language) is a very powerful dynamic programming language. For further details see http://www.tcl.tk/

$$\forall\, node\ \frac{|\vec{f}_{k+1} - \vec{f}_k|}{\vec{f}_k} < tol$$

Figure 4.3. Stopping criteria

Different numerical tests have shown that a tolerance of 0.1 has a minus influence on the result. In practice, the majority of the nodes has a much smaller change ($1{\cdot}10^{-5}$-$1{\cdot}10^{-8}$). The error norm is usually defined by the nodes of the top of the mainsail, where the results of two consecutive iterations differs more than at the rest of sail's nodes.

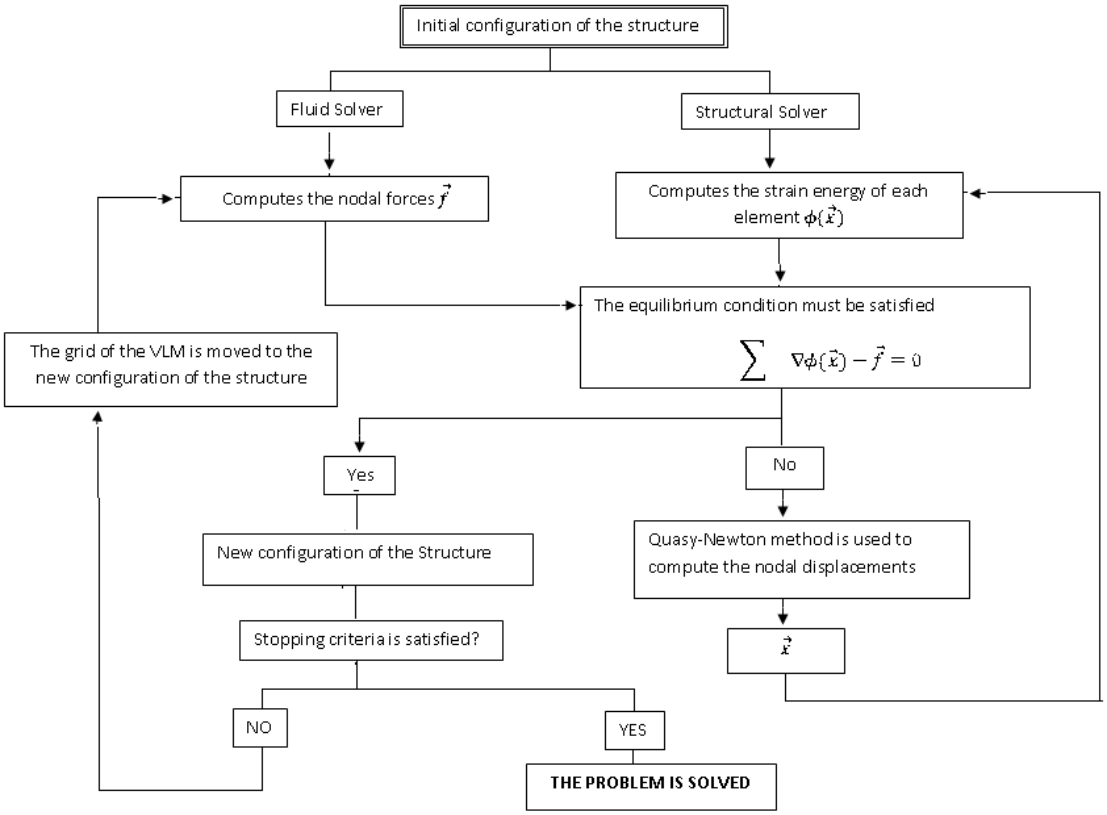

Figure 4.4. Calculation process

4.4 Conclusions

Up to this point the flow solver, the structural solver and the fluid/structure interaction algorithm have been presented. In order to fulfil the requirement of both methods, a structured mesh of quadrilateral elements is used and these quadrilateral[14] elements are split in triangular elements. The iteration scheme requires data transfer between the Fluid Solver and Structural Solver, with a updating geometry at each iteration step. The iteration process is repeated until convergence is achieved.

[14] The structured mesh of quadrilateral elements will be generated by the user of *Sailing*. This procedure is explained in the GUI (Appendix B).

5 Rigging Monitoring

Up to this point, we have a developed a FSI solver (*Sailing)*, to compute the performance of a sails and rigging configuration. Sailing, the crew trims the sails varying their position and adjusting the stress of the sheets and stays. For each adjustment, an execution of *Sailing* for the updated configuration, will result in an evaluation of the performance configuration. However, it is necessary to know the boundary conditions for the new configuration.

The main objective of this chapter is to develop a hardware/software tool to monitor the rigging, able to communicate in real time with the FSI solver. This tool will allow us finding the boundary conditions, which define the new configuration of the structure. Once known the new configuration it will be possible to compute the performance of this certain trim.

5.1 Introduction

The lift and drag coefficients can either be calculated experimentally or computationally for a given configuration of sails. When the configuration changes, because they have been trimmed, the new coefficients have to be evaluated in this new configuration.

Several authors (Jackson, 1996)(Graf, 2006)(Hazen, 1980)(Kerwin, 1978) (Krebber, 2006) introduce trim parameters into the lift and drag's formulas to consider the changes in load distribution due to geometry changes. These models consider the geometry changes brought about by the sailors that can be modelled by parameters: twist, camber and flat

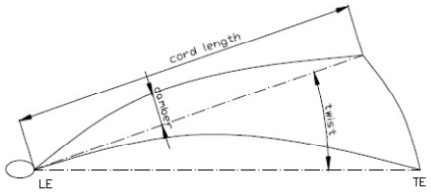

Figure 5.1. Camber and Twist

$$C_l = C_L^{max} \cdot f \cdot r^2 \cdot (1 - T) \qquad 5.1$$
$$r \equiv reef \quad r \in [0,1]$$
$$f \equiv flat \quad f \in [0,1]$$
$$T \equiv twist$$

For simplicity only the geometry of the sail was varied, even though with different sail shape all other variables like heel, boat speed and wind usually change as well.

Our goal in this work is to virtually trim the numerical model used for the FSI analysis, like the real geometry (sails and rigging) is adjusted. This will allow us

computing the lift and drag coefficients for each new configuration, with the already presented FSI solver.

The lines used to control the trim of the sails are called sheets. Since the force of the wind on the sails is often greater than the strength of the crew, it is often necessary for the sheets to have a built-in mechanical advantage. This is where the various blocks, winches and tackles come onto the scene in various configurations, to ease the work of the crew. The traveler is a device that allows changing the position where the sheet block connects to the boat. While the sheet helps the sailor to obtain the best possible sail shape, the traveler helps to set the sail at the optimum angle to the wind.

The most basic control of sails consists of setting its angle relative to the wind change, the traveler's position (twist) and finer controls adjust the overall shape of the sail (camber), varying the stress in the sheet. Therefore, it is possible to obtain the trim parameters monitoring the rigging. With these trim parameters it is possible to update the geometry, and then to compute the performance of this new configuration with the coupled fluid-structure analysis algorithm presented in the previous chapters.

As stated above, the solution of the structural calculation and the potential flow calculation depends on the adjustments of the trim parameters. The initial values of these parameters are defined in the GUI[15], but these can be adjusted in real time with the actual values during the navigation[16]. The trimming parameters that will be considered within this work are: angle to the wind, load at back stay, load at forward stay, load at shrouds, load and angle at main sheet and load and angle at jib sheet.

The monitoring system we envisage in this thesis is wireless, low-intrusive and easily adaptable to any yacht configuration. Currently such a wireless system for rigging monitoring is not available. The main references, showing the latest technology for monitoring yacht rigging and sails are the following:

- BMW Oracle Racing (ORA11) won the 33rd America's Cup yacht race. "From the drag-resistant hull to its 23-story wing sail, the BMW Oracle USA trimaran is a technological marvel". During the test runs, Oracle's team collected performance data from 250 sensors throughout the trimaran hull. With Oracle database technology the crew could compare the incremental improvements in the performance from the first day of sailing to the very last day.
  The system is a modular, integrated system where all the relevant data- from the atmospheric conditions, such as wind data via the current sailing situation, as well as the activities of the yacht-men, to the effect of all these factors on the yacht and its components- is collected directly and simultaneously within a single system. The sensors of the system used by

[15] GUI is presented at Appendix B.
[16] The updating process of the trim parameters will be presented in the next chapter.

BMW Oracle Racing are bundled and connected to a local measuring module. Significantly fewer cables are needed. The need of wires and the fact that all the sensors are defined in the design phase, and inserted in the building phase, are serious limitations for the general application of this technology[17]. A fiber optic sensor was installed into full scale hull International America's Cup Class yacht.(Murayama, 2003). The equipment of the IACC yachts with these sensing fibers is done during the construction. Rossetti et al. (Rossetti, 2011) presented a capacitive differential pressure transducer, suitable to be implemented in a wireless sensor network for wind sail monitoring. The network is aimed at sensing the pressure field acting on the surface of a sail by means of instrumented battens, providing the real-time differential pressure map over the sail surface. Each batten is constructed to house a number of wireless nodes within which a pressure sensing unit is integrated, providing independent pressure measurements.

Looking at the monitoring technology presented above, we can conclude that none of those monitoring technologies fulfil our requirements, although some of the above mentioned works could complement our work.

The development process of the tool for monitoring the rigging was developed in three different phases.

- First phase: Our first idea was to monitor the elements of the rigging by using strain gauges. Some of the key data for us are the loads in the cables and ropes of the yacht. Considering the low-intrusive requirement of the sensor system to be developed, it was thought to install the strain gauges in the block, to measure the load in the rope joined to the block.
  Following this idea, some experimental tests were carried out at LTE[18] premises, to verify:
  - The strains produced at the block are measurable. Once measured these strains, it is expected these strains to have a lineal relation with the stress at the rope. It is noted that we also want to relate these strains with other variable, the angle at the rope.
  - The use of wireless sensor networks. The test was carried out with wired sensors and with wireless sensors, to verify the reliability of the wireless system.

[17] For further information you can see the Oracle Web Page http://www.oracle.com/us/corporate/newsletter/database-insider/apr-10-bmw-184175.html
[18] Laboratori de Tecnologia d'Estructures. Universitat Politècnica de Catalunya

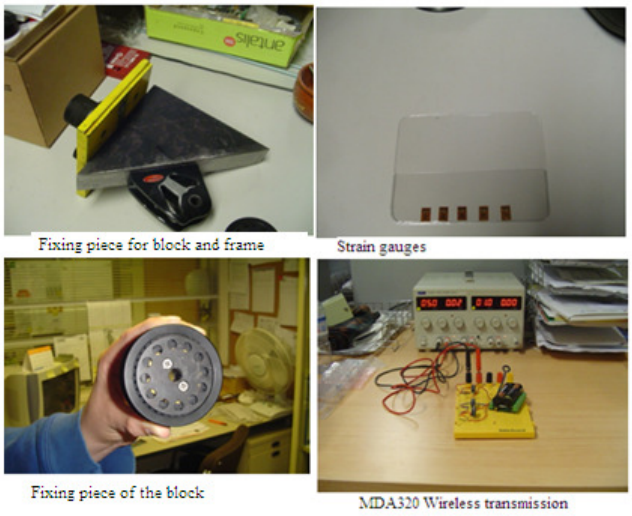

Figure 5.2. Details of the test

The frame of the block was sensorized by three strain gauges, each one oriented lengthwise, transversely and diagonally.

Figure 5.3. Strain gauges

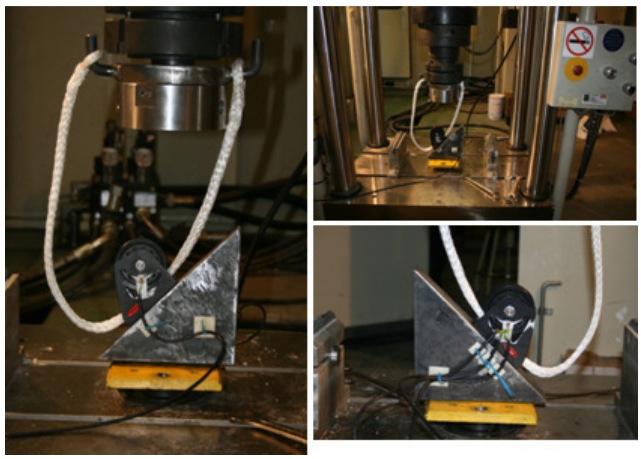

Figure 5.4. Test

Tests consisted of two complete load cycles from 0 to 20kN on the block, where the wired and wireless instrumentation was connected. The results of the two instrumentations were very similar.

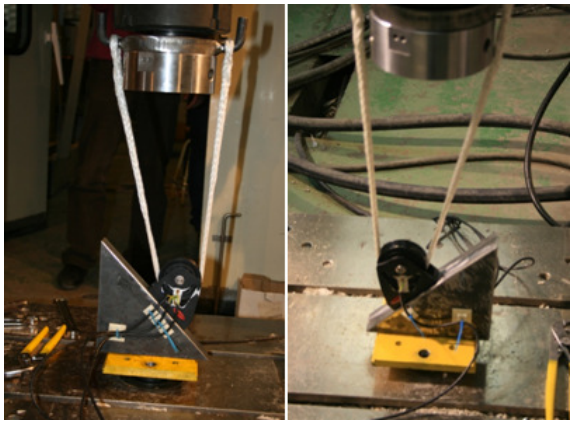

Figure 5.5. Load in the block

The data directly obtained from the sensors are the block's strains, and the data required for our purposes are the load and the angle at the rope. So it is necessary to find the relation between the strain and the load and angle at the rope. The measured relation is shown in the following figure.

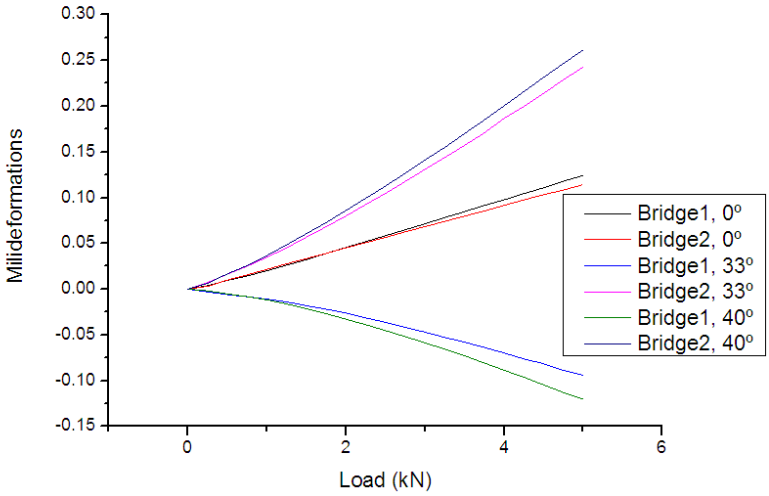

Figure 5.6. Relation between block's strain and load and angle of the sheet

We expected to prove the linear relation between the longitudinal strain of the gauges and the load applied at the rope, and we can see that the results of the test don't show an exact linear relation between those variables (Ortigosa, 2009(a)). This effect is attributed to deficiencies with the way to fix the block to the wedge in the experiment, since the different tests show that the structure was working in the elastic range.

Regarding the design of the device, it will be necessary to add a watertight compartment to install the electronic system for the measurement and the

transmission of data, and the battery. In Figure 5.7 is shown a block designed for this purpose with a watertight compartment.

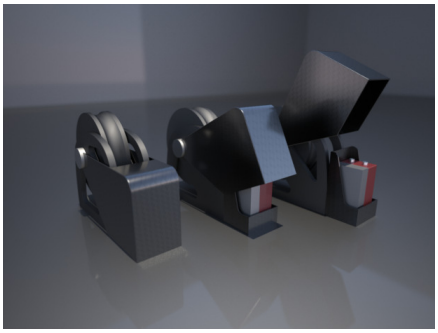

Figure 5.7. Design of a block with a watertight compartment

With this test was proved the possibility to evaluate the required parameters (force and angle on the rope) by monitoring an element where the cable is joined. Therefore, it will be starting point for the development of the tool to monitor the rigging.

- Second phase: During this phase we were centred in some of the most important element for trimming the sails, the main traveler. With the main traveler, it is possible to control the load and angle of the main sheet and angle to the wind. To obtain these parameters will be necessary to get the traveler's position and the main sheet's stress. So, the starting point to obtain these trim parameters is to monitor the main traveler.

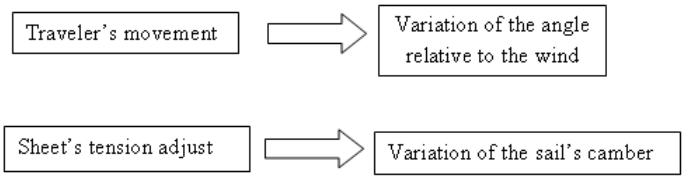

Figure 5.8. How to obtain the trim parameters

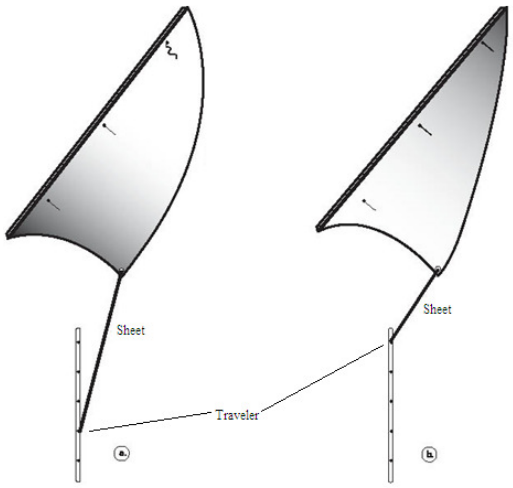

Figure 5.9. Trimming the sails

The idea developed in this phase of the work was to arrange the sensor to the traveler's block, in order to measure indirectly the sheet's stress, the angle of the sheet and the position of the traveler. The data measured by these strain gauges will be the block's strains and these data will be treated to obtain the main sheet's stress and angle. The position of the traveler is obtained afterwards from the angle of the main sheet.
It is expected that the strain of the main traveler's block will be related linearly with the main sheet's stress, but the relationship with the angle of the main sheet can be more complex. Different experimental tests have been carried out: first to ensure that the strains of the main traveler's block will be easily measurable, and second to study how the strain data is actually related to stress and angle of the main sheet.

- Third phase: The element developed during this phase is a low intrusive and easily adaptable to any yacht configuration. Furthermore, it can be adapted to measure the stress in any rope or cable of the boat. This element can be easily adaptable to any other fixing element of the rigging.

In the test described in the first phase, the direct relation between the strain and angle of the rope and the strain of the block was proved. But the strains must to be treated in order to obtain the desired trim parameters. The selected transformation algorithm for this purpose is the so-called Artificial Neural Networks (ANN), which will be introduced in the next section.

5.2 Neural Networks

Neural Networks or Artificial Neural Networks are one technique used in artificial intelligence that can be considered an extension of the conventional techniques of statistical models of recognition, offering satisfactory results in this field.

ANN offer a powerful general structure to represent nonlinear relationships between multiple input variables and several output variables, where the form of adjustment is governed by a number of adjustable parameters. The process of setting these parameters is called learning or training. Generally, ANN models represent nonlinear functions of many variables by overlapping functions of a single variable, called hidden functions. The hidden functions are adapted to the input data as a part of the training process. The number of such functions only grows with the complexity of the problem, and not with the size of the problem. The number of free parameters in these models, for a given number of hidden functions, typically grows just linearly or quadratically with the dimension of input space. Compared to the dependence of the polynomials regression is clear that the neural network model is much simpler to the adjustment of parameters.

ANN offer advantages for approximation of functions in spaces of multiple dimensions, the price to be paid for this advantage is that the procedure for determining the adjustment of the hidden functions is a nonlinear optimization

problem, which is computationally intensive and poses a number of additional complications such as the presence of multiple minimums in the error function.

In this work a multilayer perceptron neural network will be used, whose basic unit or hidden function (neurons) is called perceptron.

To develop the ANN applied to our problem, an open source Neural Network C++ Library developed at CIMNE by the researcher R. Lopez (Lopez, 2008) will be used (Ortigosa, 2009(b))(Ortigosa, 2007).

5.2.1 The artificial neuron, the perceptron

In 1962, F. Rosemblatt devised a computer model based on the functioning of human neurons. Human neurons are divided into three distinct parts, dendrites, nucleus or soma and axon. The dendrites transmit the potential of neurons adjacent to the soma. The soma is carried out the integration of all information obtained in the dendrites. The axon transmits the message to other neurons resulting from the integration, through an electrochemical signal.

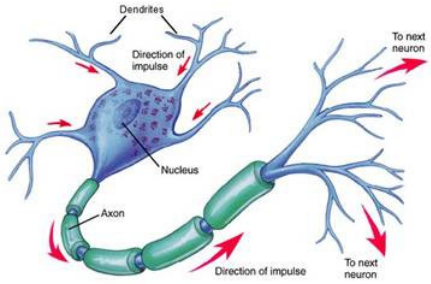

Figure 5.10. Neuronal Structure

Based on this neuronal structure F. Rosemblatt designed the perceptron model, which represents human neuron.

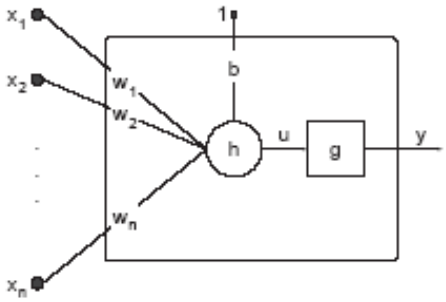

Figure 5.11. Perceptron neuron model

The perceptron receives input signals, processes the information received and transforms it into an output signal. In the process of transforming information involves three basic elements:

- A set of free parameters, consisting of a synaptic weight vector $(w_1,...,w_n)$ and a tendency, or bias $\boldsymbol{b}$.
- A combination function that combines the input signals with the free parameters, resulting in a net output signal $\boldsymbol{u}$.

$$u = h(x;b,w) = b + \sum_{t=1}^{n} w_t \cdot x_t \tag{5.2}$$

- An activation function, that taking as an argument the net output signal results in the output signal.

$$y = g(u) \tag{5.3}$$

The activation functions used in this work are the sigmoidal activation function Figure 5.12 and the linear activation function Figure 5.13.

$$g(u) = \tanh(u) \tag{5.4}$$

$$g(u) = u \tag{5.5}$$

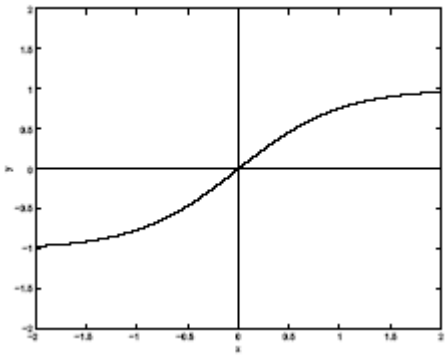

Figure 5.12. Sigmoidal activation function

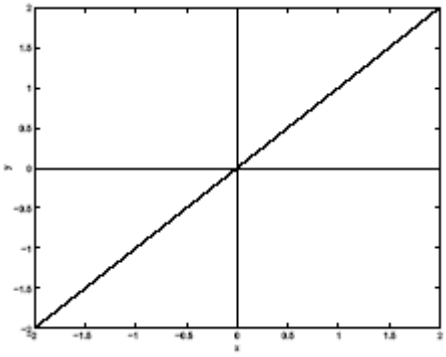

Figure 5.13. Linear activation function

5.2.2 Multilayer Perceptron

Neurons can be combined to form a Neural Network. The network architecture refers to the number of neurons, their position and their connections. The multilayer perceptron model consists of a set of sensor nodes that constitute the input layer,

one or more layers of hidden neurons and a set of neurons that constitute the output layer. The neural network used in this work is the multilayer perceptron with a single layer of hidden neurons.

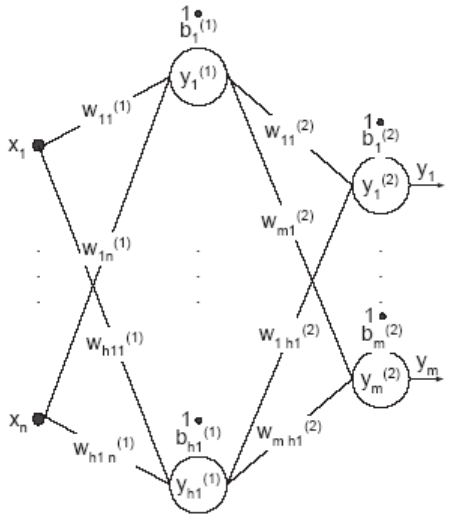

Figure 5.14.Multilayer perceptron with two layers of perceptrons, the hidden layer and output layer.

The network showed at Figure 5.14 consists of one hidden layer with n inputs, m outputs and h_l neurons. Each neuron performs the above process with the perceptron model, combining the different entries with the free parameters.

$$y_j^{(1)} = \sum_{i=1}^{n} w_{ji}^{(1)} \cdot x_i + w_{j0}^{(1)} \qquad 5.6$$

Where the superindex (1) refers to the firsts layer of neurons, the hidden layer.

If we add the trend as the weight of the variable $x_0 = 1$, we can write the net output as

$$y_j^{(1)} = \sum_{i=0}^{n} w_{ji}^{(1)} \cdot x_i \qquad 5.7$$

The output of each neuron is obtained by applying the net output as an argument to the activation function, which for the hidden neurons is of sigmoidal type.

The output of the network is obtained by transforming the activation of neurons in the hidden layer, using a second layer for processing each of the output variables by a perceptron with a linear activation function. A combination of the hidden functions given by the hidden neurons is done in the output perceptron.

$$y_k^{(2)} = \sum_{j=1}^{h_1} w_{kj}^{(2)} \cdot z_j + w_{k0}^{(2)} \qquad 5.8$$

$$y_k^{(2)} = \sum_{j=0}^{h_1} w_{kj}^{(2)} \cdot z_j$$

The activation of the output k is obtained transforming this combination using the linear activation function $y_k = g(y_k^{(2)}) = y_k^{(2)}$.

The number of layers of the network refers to the number of layers of hidden neurons contained in the network. We will work with a network with two layers of neurons, being one the hidden layer and the other the output layer, but having just a single layer of hidden neurons we will say that it is an ANN of one layer of neurons.

The process to generate the neural network requires a learning task, based on the definition of an appropriate error function, which is minimized by varying the weights and network trends. In our case, the definition of the error E^n is given by:

$$E^n = \frac{1}{2} \cdot \sum_{k=1}^{c} (y_k(x_i, \ldots, x_d; w) - t_k)^2 \qquad 5.9$$

Where t_k are the target values.

To minimize the error it is possible to use different mathematical methods, such as gradient descent method or the quasi-Newton method. The solution process seeks to minimize this error, and is called training or learning of the network. In our case this minimization is performed using an algorithm based on the quasi-Newton method.

An important consideration is the adjustment of the ANN architecture to prevent under-fitting or over-fitting. In standard polynomial approximation, the optimum setting is achieved with an appropriate polynomial's degree to our data. While in ANN the quality of the approximation is controlled by setting the number of free parameters. The free parameters increase with the number of neurons and with the number of layers of network. We will just consider in this work an ANN with one hidden layer, so we will try to determine the number of neurons in the hidden layer required to obtain an optimal fit.

The phenomenon of under-fitting can be found when we try to adjust the data using a too simple ANN architecture (too few neurons in the hidden layer).

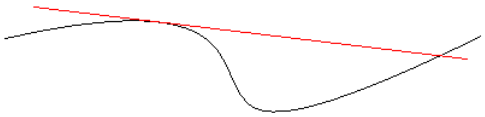

Figure 5.15. Insuficient adjustment of a function, under-fitting
(original function in black, approximation in red).

While if we try to adjust the data using a too complicated ANN architecture, the over-fitting phenomena can be found.

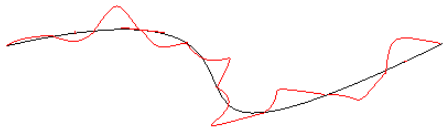

Figure 5.16.Example of over-fitting of a function
(original function in black, approximation in red).

In order to identify the optimum ANN architecture, different configurations must be trained. In a validation exercise, the optimal ANN will be that offering a minor error in the prediction of a set of control data.

5.2.3 Optimal network architecture

As it was stated before, we will work with an ANN of a single hidden layer of neurons, so the optimal architecture is determined by the number of neurons at the hidden layer.

To determine the optimal architecture, networks with different number of neurons are trained. Once the network is trained, validation data will be used to verify the error between network output and the output of the validation data. The optimal architecture or the optimal number of neurons is the one with a minimum error in the validation process. If the number of neurons is too small for the complexity of the problem we will have under-fitting. If the number of neurons is too high for the complexity of our problem we will have over-fitting.

5.3 Evolution of the main traveler's sensor design

It has been introduced before, that the process of development of the monitoring tool was divided in three phases. During the first phase, we proved the relation between the strain of a block and the load and angle of the cable joined to this block. Furthermore, a method for the treatment of the data, ANN, allowing to obtain the trim parameters from the strain measured in the block, has been presented in the previous section.

From now we will focus our work in obtaining three of the most important trim parameters: load in the main sheet, angle in the main sheet and angle to the wind. This is the goal of the second phase of the process of development of the monitoring tool: design of a sensorized main.

As stated before, the monitoring system we envisage in this work must be, wireless, low-intrusive and easily adaptable to any yacht configuration. Furthermore, additional requirements, like water-proof characteristics for the electronics compartment have to be considered

The evolution of the design was defined by the sensor system selected. Initially the MicroStrain (Mic) Wireless Sensing system was evaluated, but finally it was dismissed by excessive dimensions, reduced reliability and by limitations of battery's life. The second and definitive sensor system was based on Libelium's WaspMote (Was) platform.

A new design of main traveler block was thought to add the wireless transmission data system in the main traveler block. The dimensions of the block are defined by the dimensions of the wireless sensor node MicroStrain's V-Link® that must be inserted inside. The following picture shows the resulting design:

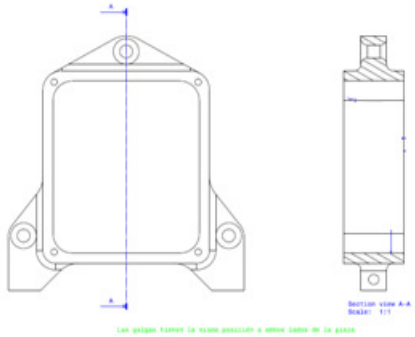

Figure 5.17. Block of the main traveler

Dimensions of this preliminary design of the block are: 10 cm of height, 11 cm of length and 3 cm of thickness.

A experimental test with the new design was carried out by the same Laboratory, LTE[19]. The data were acquired using the V-Link Wireless Voltage Node by MicroStrain (Mic11) that is presented in Appendix C.

In parallel to the experimental tests, the design was simulated computationally with RamSeries, to prove that the experimental results could be reproduces by FEM analysis.

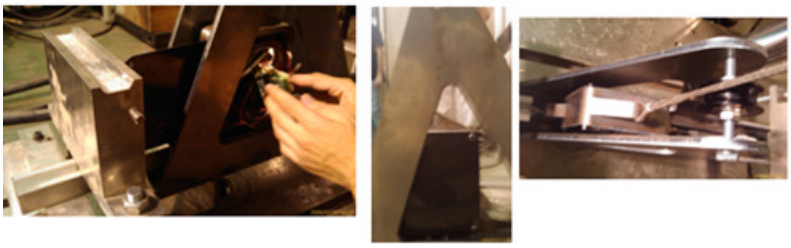

Figure 5.18. Second experimental test

[19] Laboratori de Tecnologia d'Estructures. UPC. Working team: Tomàs García Vicente, Carlos Hurtado Gómez and Jordi Lafuente Navarro.

For the experimental test, the design was sensorized with eight strain gauges, distributed making two full Wheatstone bridges. One full bridge was fitted at each side of the block as shown in the following picture.

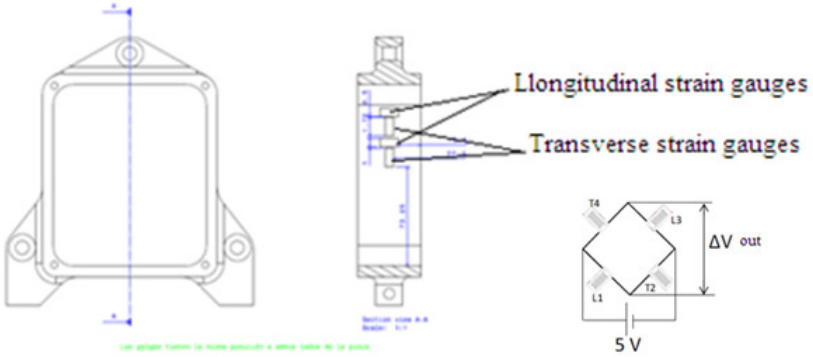

Figure 5.19. Connections of the strain gauge to full bridge

The technical specifications of the strain gauges are:

- Nominal resistance: $120\Omega \mp 0.35\%$
- Active grid length: $6\ mm$
- Gauge factor, K: $2.08 \mp 0.1\%$
- Transversal sensibility: -0.1%
- Material: $80\%\ Ni + 20\%\ Cr\ \ (\nu = 0.03)$

The bridge is excited with $V_{ext} = 5V$ and the output of the full bridge ΔV_{out} is related with the longitudinal strain of the block (understanding the longitudinal strain like the strain in the height direction of the block).

$$\Delta V_{\text{out}} = \frac{1+\nu}{2} K V_{ext} \varepsilon \qquad 5.10$$

The variation of the load makes change the output of the full bridge, so it is possible to relate the longitudinal strains on each side of the block with the load's change and angle's change of the rope. The load was changed of 0 to 5kN with increases of 0.25kN, and the data was taken for angles of 0º, 13º, 29º and 33º.

The same test was carried out with the structural analysis solver (RamSeries), using a 3D linear elastic solid model.

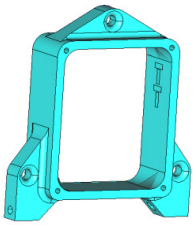

Figure 5.20. 3D geometry of the CAE model

To simulate correctly the operation of the block, the CAE model is completed with the following boundary conditions:

- The $\boldsymbol{z}$ and $\boldsymbol{y}$ displacement are restricted at the surfaces of the block in contact with the traveller's fixings.

Figure 5.21. Surfaces with z and y displacements restricted

- The $\boldsymbol{x}$ displacement is restricted at the surfaces of the block in contact with the port tack sheet and starboard sheet.

Figure 5.22. Surfaces with x displacement restricted

- A distributed load is applied at the surface in contact with the sheet, that joins the boom with the traveler.

Figure 5.23. Surface with a distributed load

Strain gauges are also defined in the model as shown in the following picture.

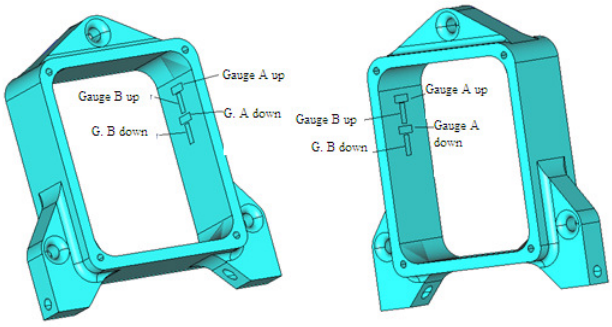

Figure 5.24. Gauges in the simulation model

The same load and angle cases of the experimental test, was simulated with RamSeries.

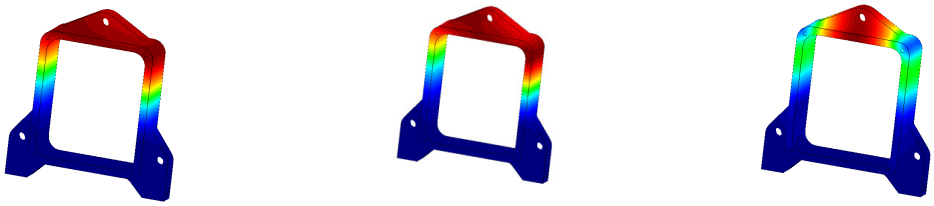

Load 4.5kN
Angle 29º

Load 2.25kN
Angle 13º

Load 2.25
Angle 0º

Figure 5.25. Some Ramserie's results

The results of displacements at the nodes of gauges are treated to obtain the strain of the gauges. The longitudinal strain of each side of the block is calculated like the longitudinal strain's average of the longitudinal gauges (gauges B).

The results of the experimental test and the results of the simulation are compared to validate the simulation and to validate the wireless system used to acquire the data. The numeration 1 and 2 in the following pictures indicate each side of the block.

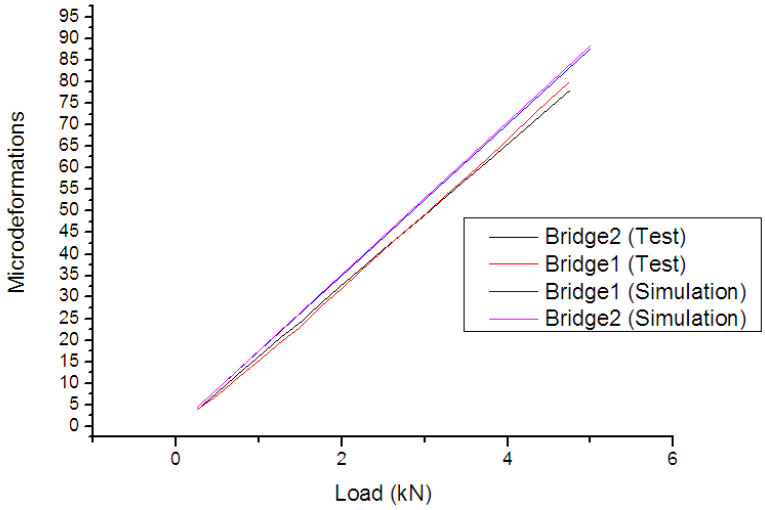

Figure 5.26. Relation between simulation results and test results, 0°

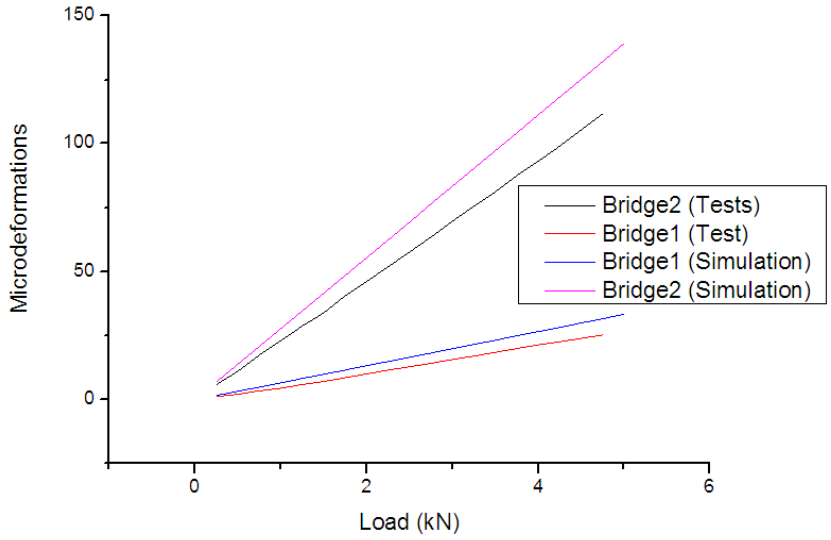

Figure 5.27. Relation between simulation results and test results, 13°

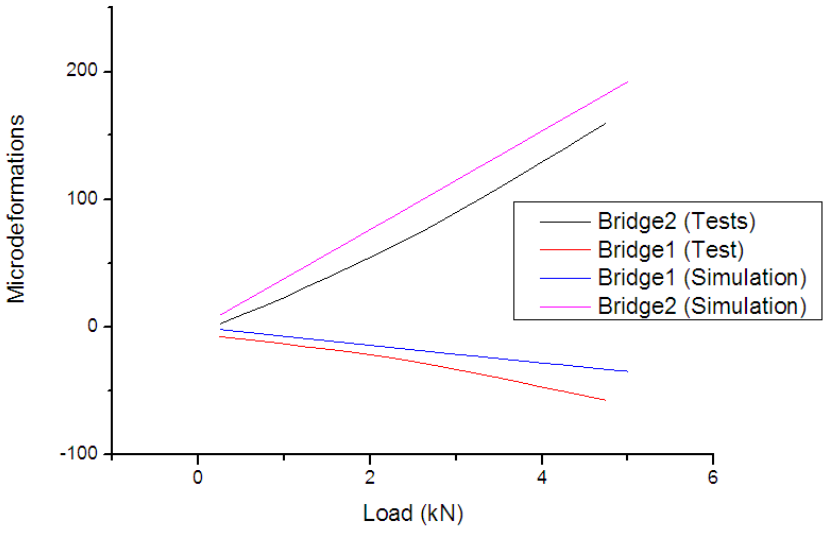

Figure 5.28. Relation between simulation results and test results, 29°

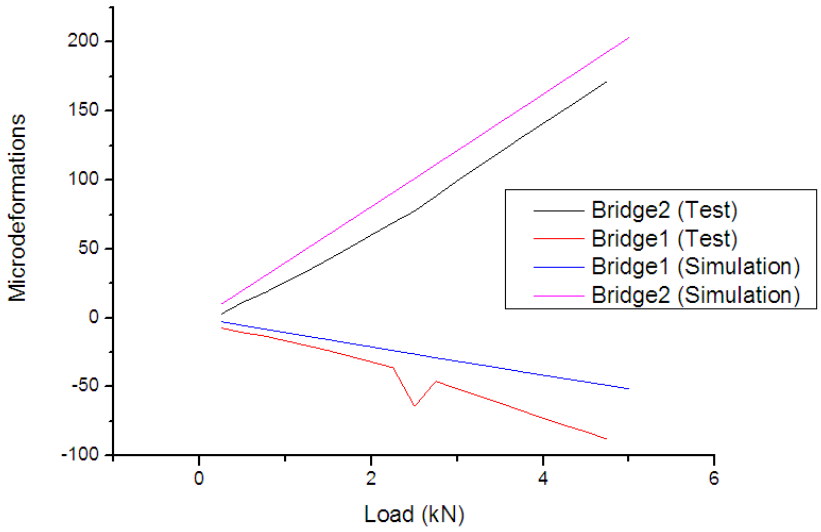

Figure 5.29. Relation between simulation results and test results, 33°

It is possible to observe a difference between the simulation results and the test results. This difference is attributed to the fact that during the test, the position of the gauges was not measured and therefore the virtual gauges was not located at the exact place. Moreover, it is necessary to mention the existence of non-lineal variations due to the rail deformation. Despite these differences, the behaviour of the gauges is quite similar in the experimental test and in the simulation, what proves the validity of the numerical analyses.

Once the preliminary computational results were validated, a wider simulation campaign was conducted. In order to obtain enough data, more cases with different loads and different angles were simulated. As was expected the relation load-strain is found to be linear, but the slope of this linearity depends on the angle of the sheet and the strain is thus not linearly dependent on the two parameters. This was the main reason to select an ANN to fit our data.

The ANN for our problem will be constitute by two inputs, strain of each side of the block and two outputs the load and the angle of the rope. This ANN has one hidden layer of neurons. As it was stated before it is possible to determine the optimal architecture of the ANN varying the number of neurons at the hidden layer.

For the validation task, 60% of the simulation data were selected randomly as training data, 20% of the simulation data were selected randomly as validation data and the other 20% of the data were used as testing data. The training and validation data are used to adjust the hidden internal parameters of the neural network. Once the neural network is adjusted to the data, it is executed with the inputs of the testing data, and these results are compared with the testing data results. The testing results and the neural network results are compared and a linear regression is adjusted. The optimal neural network will give a perfect linear regression with 1.0 slope and correlation coefficient. Linear regressions for three different configurations of neural network are showed in the following graphs.

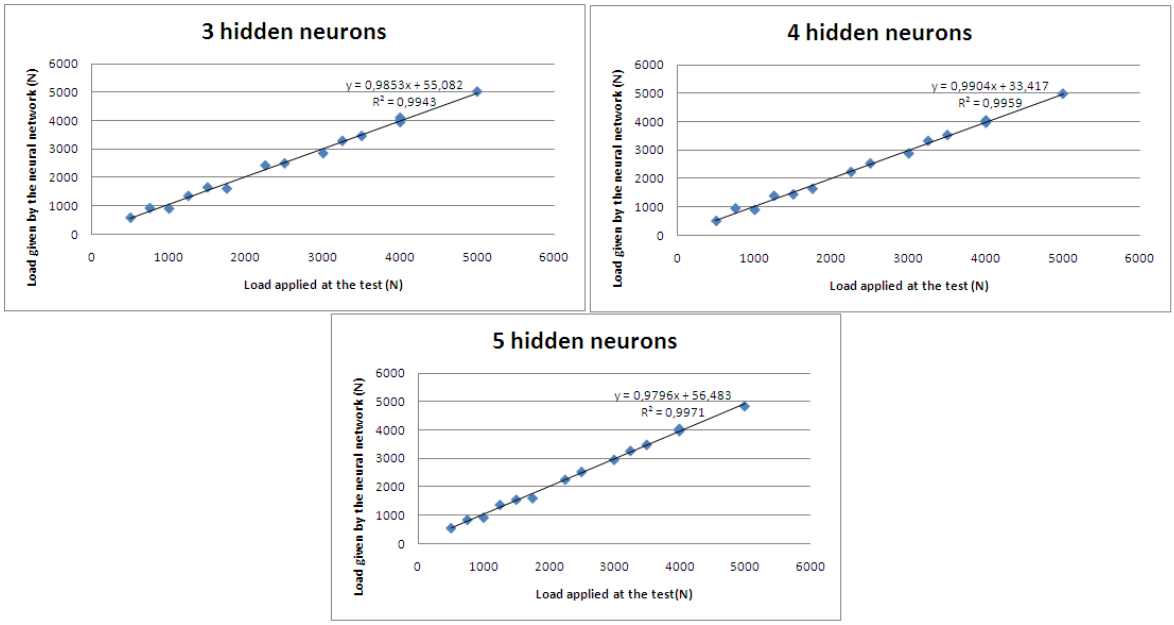

Figure 5.30. Results of the different configurations of neural networks

The best adjust is obtained with four neurons at the hidden layer, so the selected neural network configuration is the following:

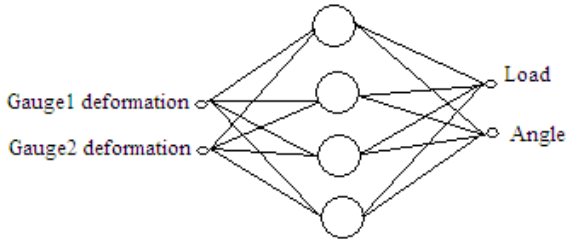

Figure 5.31. Neural network configuration

The wireless transmission data system used until this moment has been the V-Link Wireless Voltage Node. The battery's autonomy, reliability and dimensions of the V-Link node are main drawbacks of this device, which motivated us to look for an alternative wireless data transmission system. The intention was to find an electronic system with reduced dimensions and with battery autonomy of 4-5 days, or the possibility to use renewable energy using solar panels on the watertight lid.

After an evaluation of different available options, the platform Waspmote[20] (Was), developed by Libelium, was selected. Waspmote is a development platform with different commercial implementations, but unfortunately it did not provide any support for strain gauges. Therefore this support had to be developed for this project, including hardware strategies to increase the battery life to a maximum.

[20] It will be explained at Appendix D, but all the information can be found at the Libellium web page.

Using Waspmote technology has been possible to overcome the dimensional and autonomy drawbacks. The dimensions of Waspmote, 73.5 x 51 x 13 mm, have made possible to design a main traveler block smaller and with nicer forms. The following picture shows an updated design of the traveler block, using Waspmote technology.

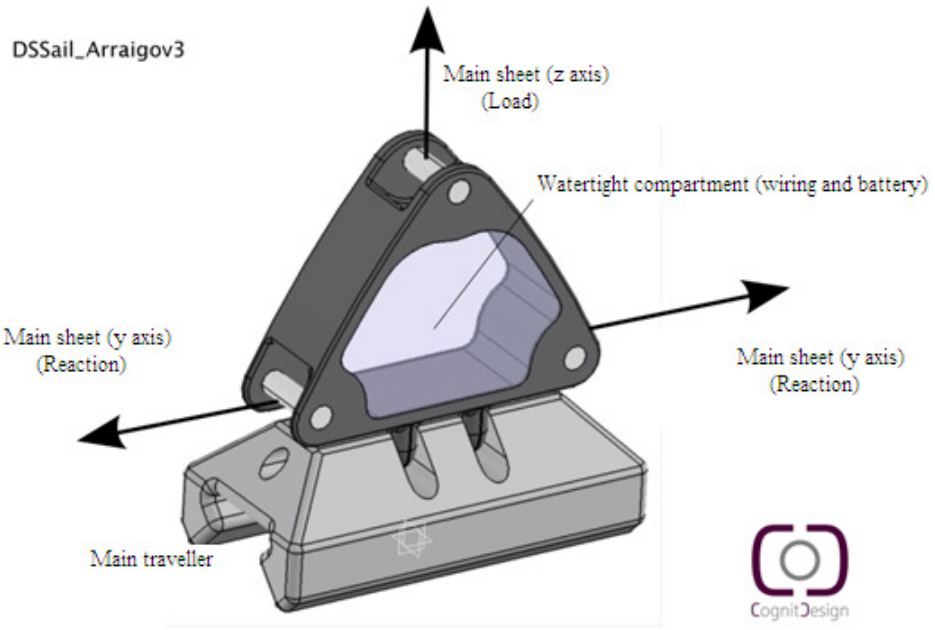

Figure 5.32. New main traveler

Until now, we have a sensorized main traveler to obtain three trim parameters, the load in the main sheet, the angle in the main sheet and the position in the traveller rail. But we still need to define a strategy to measure the rest of the trim parameters: the angle to the wind, load at back stay, load at forward stay, load at shrouds, load and angle at main sheet and load and angle at jib sheet. This fact was the reason to direct our design forward developing a flexible element, which could be incorporated at main traveler, jib traveler, stays and shrouds.

From now, the third phase of the process to develop a monitoring tool starts. During this phase a sensor was designed to be installed in every element of the boat to be monitorized. This new device is presented in the next section.

5.4 3D Remote Rigging Monitor

One of the basic requirements of the envisaged monitoring instrument was the flexibility. Up to now, we have just presented several options able to sensorize different elements of the rigging of a yacht. The next goal was to fulfil the flexibility requirement by developing an element to monitor any rope of the sailing yacht. It fact, the so called 3D Remote Rigging Monitor (3DRRM) has been designed to be adapted to any rope of the boat: main sheet, jib sheet, shrouds or stays.

Figure 5.33. 3DRRM design

Figure 5.33 shows the basic design of the block. This configuration is adequate for monitoring any rope of the yacht, but3DRRM can also be configured to monitor the mainsail traveler by means of an adaptation part, as shown in the following figure.

Figure 5.34. Adaptation part

Figure 5.35. Block for mainsail's traveler

The 3DRRM could be located at any rigging element of the yacht. As it will be presented in the next chapter, 3DRRM could be located in main traveler, in jib traveler, in shrouds and in stays. The data obtained by these 3DRRRM can be treated to obtain all the trim parameters required for our purposes.

The data acquired in each 3DRRM are the strains on the 3DRRM, but executing an adjusted Neural Network, it is possible to obtain the force and the angle at the rope. This information can be monitorized from a graphic user interface (GUI) developed for this purpose (see Figure 5.36).

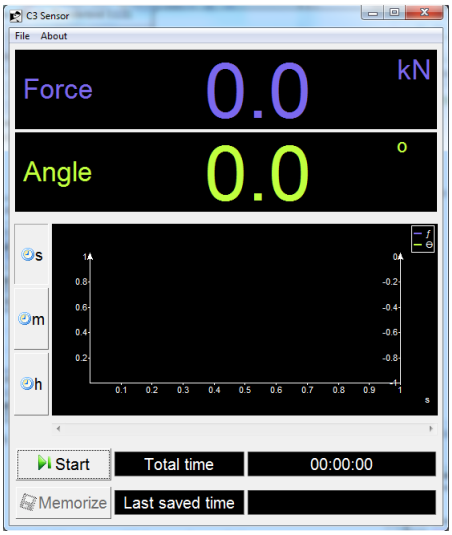

Figure 5.36. User interface of the acquisition data program

5.5 Conclusions

Our objective in this chapter has been to design an element for monitoring the rigging to obtain the different trim parameters.

First we proved the relation between the strains of a block and the load and angle of the rope joined in this block. It was the first step to obtain the desired trim parameters. Since, one of the most important trim parameters of the sails is the force and the angle at the main sheet, our first goal was to design a sensorized block for the main traveler. We first proved that was possible to obtain the force and the angle of the main sheet transforming the data of the sensors making use of an ANN.

Once the possibility of obtaining the trim parameters by the treatment of the data of the strain gauges located at the main traveller has been proved, a design of an element to monitor any rigging element of the yacht was developed. This device was “3D Remote Rigging Monitor” (3DRRM). The 3DRRM has been designed with the following advantages:

- It can be easily adapted to monitor any rope of the boat.
- It can monitor the force and the angle of the rope.
- It is a wireless system.

The idea and the system explained previously turned out to be many innovative, so it is in process to be patented.

Now we have an element to monitor any rigging element of the yacht, the 3DRRM. From now, we will study the different applications of the 3DRRM for obtaining all the desired trim parameters.

6 Integration of monitoring system with the coupled fluid-structure interaction algorithm

The main objective of this work is to develop a real-time simulation tool of the behaviour of sails and rigging, to help the crew to optimize the performance of the sailing yacht. There are two main ingredients of this simulation tool:

- The FSI solver able to compute the performance of a certain sail/rigging configuration, and
- The tool to monitor the different elements of the rigging.

To compute the performance of the yacht, it is necessary to virtually trim the CAE model as it is in the sailing yacht. For this purpose it is necessary to measure all the trim parameters: angle to the wind, load at back stay, load at forward stay, load at shrouds, load and angle at main sheet and load and angle at jib sheet.

The 3DRRM system, presented in the previous chapter, has been designed to obtain the above mentioned parameters. This chapter will introduce the different adaptations of the 3DRRM to measure those parameters. 3DRRM's acquired data have to be communicated in real time to the FSI solver. For this purpose a TCL interface has been developed. The main characteristics and functionalities of this interface will be presented. Finally, some auxiliary algorithms are presented.

6.1 Introduction

At the previous chapter we saw the possibility to acquire the load and the angle of the main sheet by the sensorized mainsail traveler. Data acquired by the sensors in this case is the traveler's block strain. We showed that adapting an ANN, it is possible to obtain the load and angle of the main sheet (trim parameters) from the measured data. In the following, we will study the different configurations of the 3DRRM and the data treatment necessary for each case, to obtain every trim parameter: angle to the wind, load at stern stay, load at forward stay, load at shrouds, load and angle at main sheet and load and angle at jib sheet. These parameters are complemented with the wind data (apparent wind angle and apparent wind velocity), obtained by specific sensors.

The practical applications of 3DRRM to be presented in this chapter, will be made in the rigging of a GP 42 [21], specifically in "Totalboats GP42" yacht (see http://www.youtube.com/watch?v=OLKEmI6cjMY). The sail plan of this Offshore Racing Congress (ORC) Grand Prix class, has the basic specifications that are shown in the next figures.

[21] For further information about the class, see the official web side. *www.**gp42**.net/*

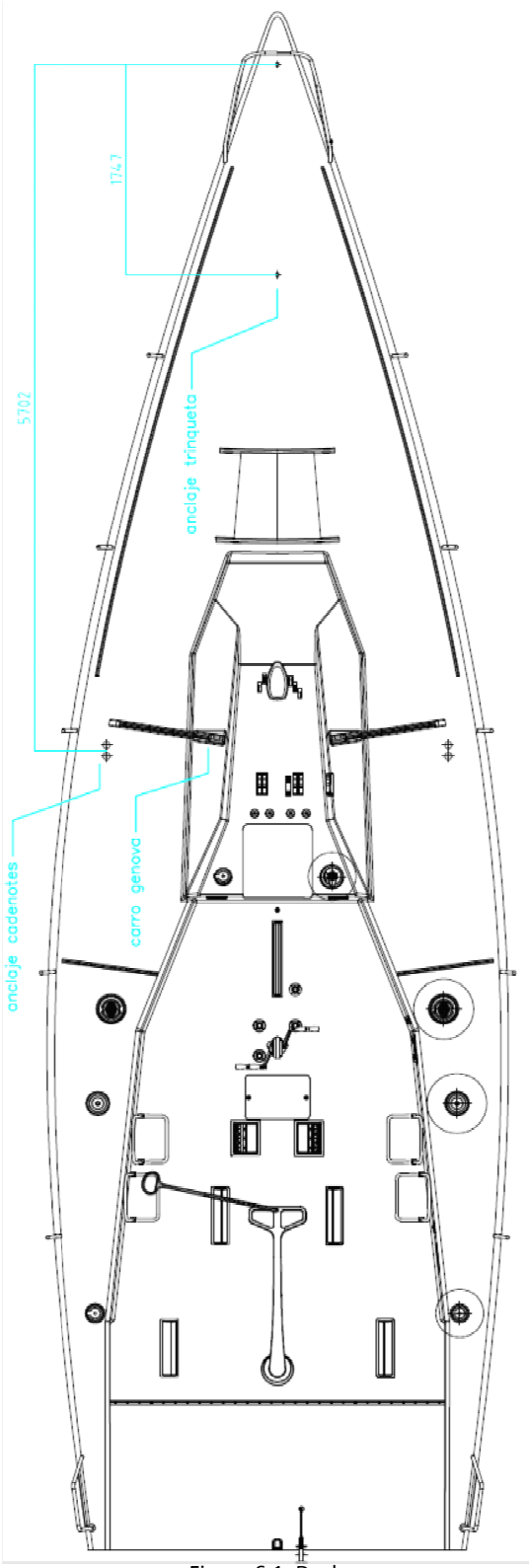

Figure 6.1. Deck

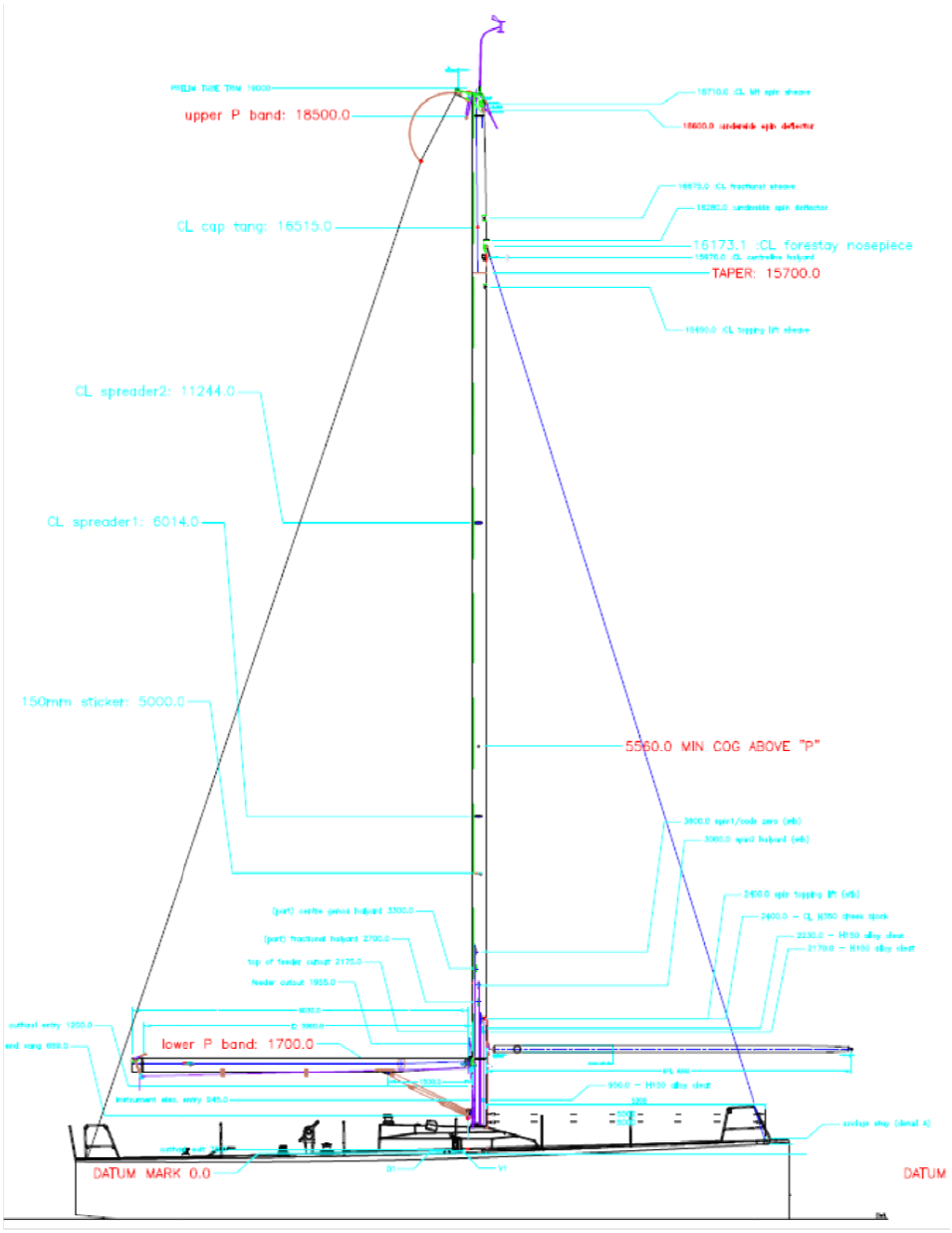

Figure 6.2. Sail Plane

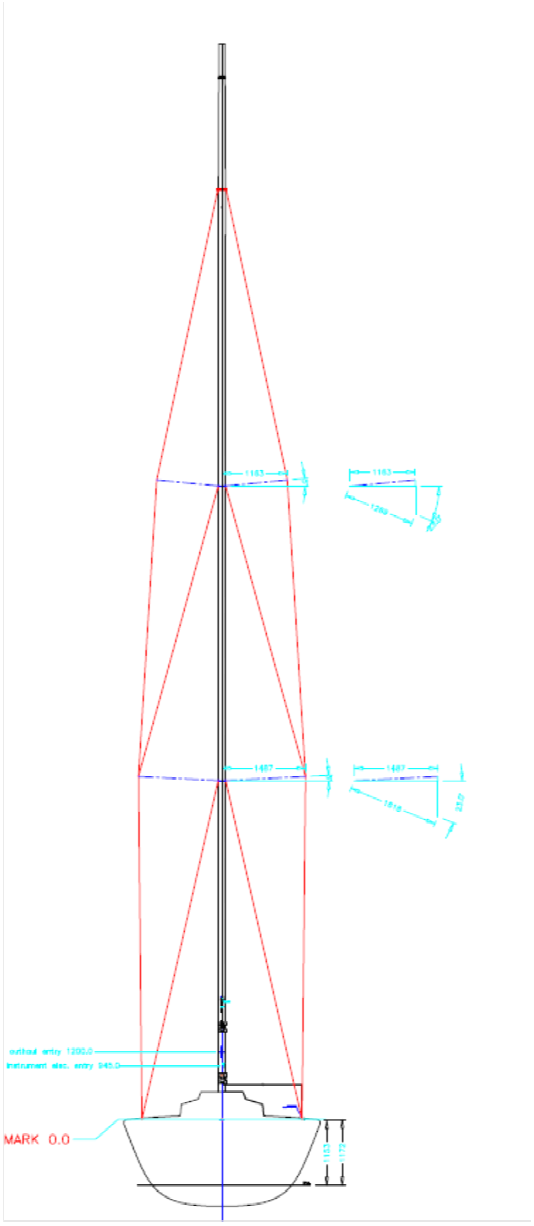

Figure 6.3. Rigging

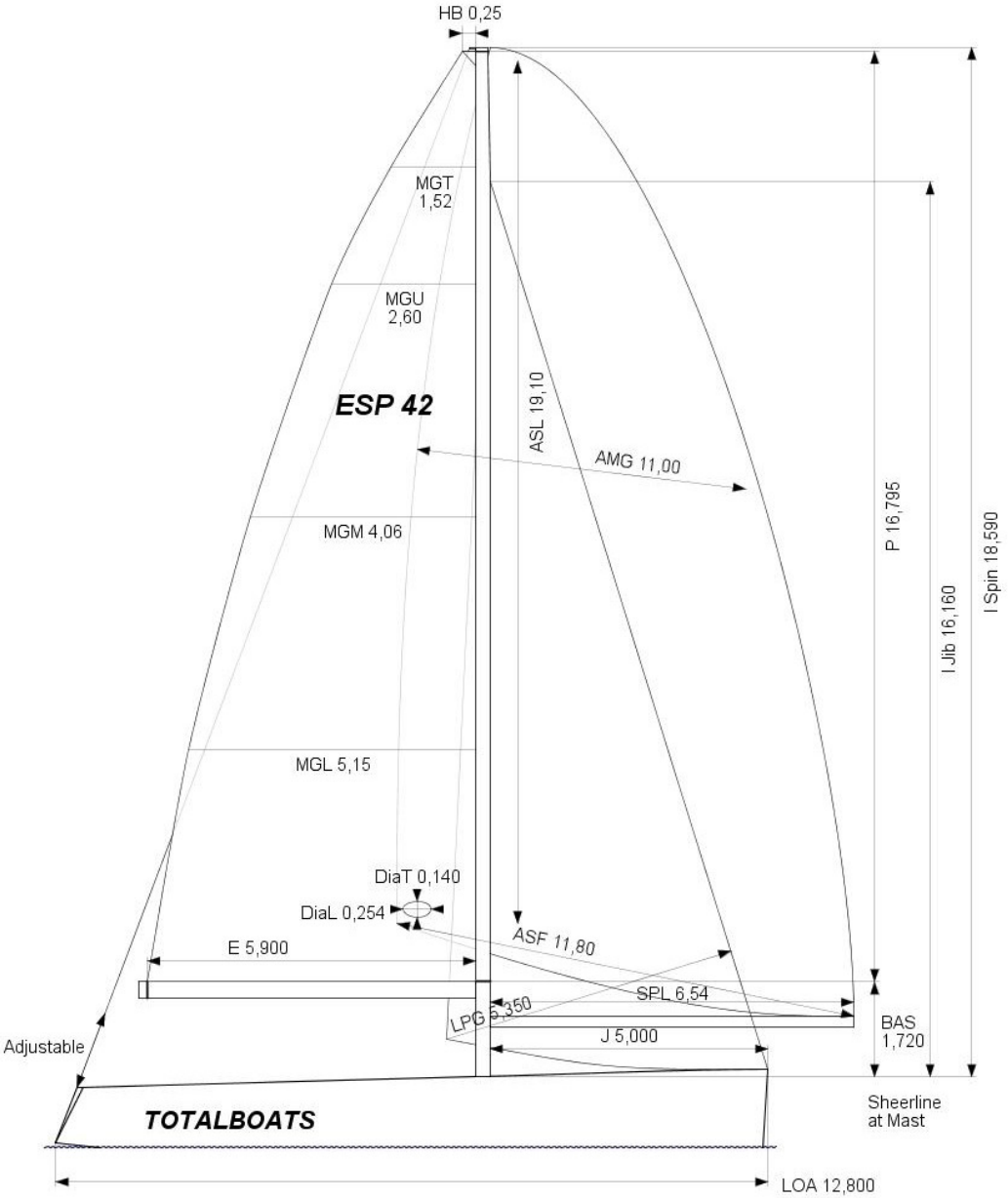

Figure 6.4. Totalboats. http://www.orc.org/gp42.htm

The coupled aerodynamics/structural calculation algorithm must be continuously connected with the Wireless Sensor Network WSN. The WSN will give us information about the forces acting on the ropes. We will use this information as inputs and boundary conditions to the calculation/simulation system. The data acquired by the WSN is transmitted to the aerodynamics/structural calculation via an interface programmed in C++ to interpret TCL [22]scripts.

[22] For further information see the web http://www.tcl.tk/

6.2 Monitoring the rigging and the sails

The trim of the sails is adjusted with the load on the different ropes of the boat (shrouds, main sheet, jib sheet and stays) and with the position of the main traveler and the jib traveler (if the boat has one). These factors, the loads of the ropes and the positions of the travelers and the direction of the sheets, are the parameters we want to know. For this purpose, factor we will monitor the different elements that are shown in the following figure.

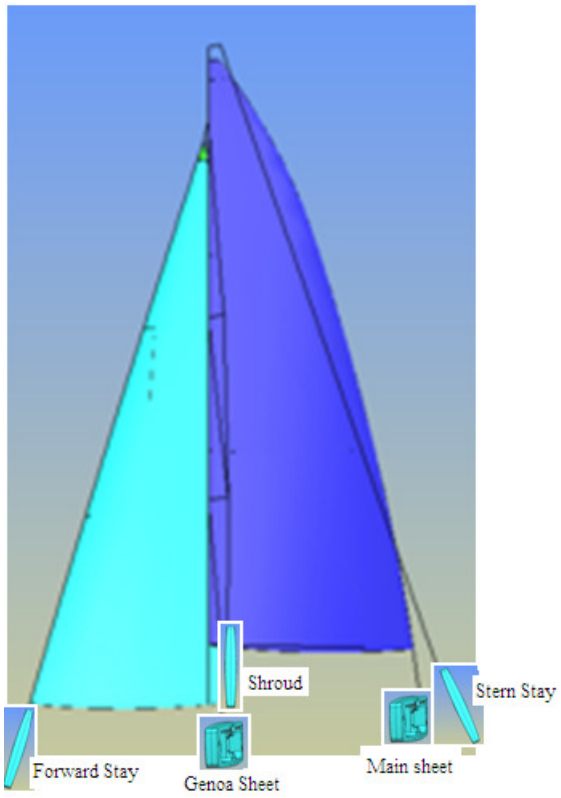

Figure 6.5. Monitoring Rigging

In the following, each configuration of the 3DRRM, back stay, forward stay, shrouds, jib sheet and main sheet, will be analyzed and an application to obtain the load and the angle on sheets will be presented. The same process will be repeated at each case:

1. The CAE model of the 3DRRM will be generated considering how the boat is oriented respect to the reference system at the FSI solver, and considering how the 3DRRM is set up on the boat.
2. The real constraints and boundary conditions of the 3DRRM will be studied, and applied to the CAE model.
3. The work range and directions of load, which are applied at the 3DRRM, will then be defined.
4. The relation between 3DRRM's strain and rope's load is obtained for every simulation case. These data are used to adjust a neural network, to obtain the load of the rope from the measured strain of the 3DRRM.

Once we have the load of stays, shrouds and sheets, the travelers position, the main sheet angle and the jib/genoa sheet angle, we have the necessary trim parameters for the FSI solver.

6.2.1 Main sheet and jib sheet.

The application of the 3DRRM to the main traveller was already presented in the previous chapter, so the same case has been reproduced with the new design. The problem will be the same for the main traveler as for the jib traveler, so it will be done just once.

CAE model

The CAE model has been generated as shown in the following picture.

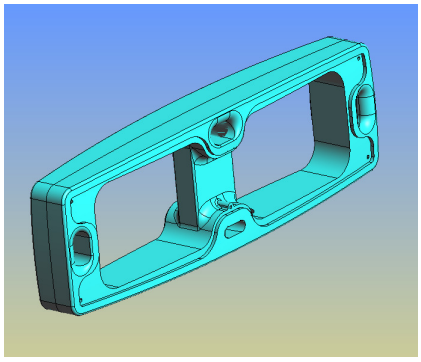

Figure 6.6. CAE model of the block

The two full Wheatstone bridges of the actual device have been defined in the geometry, to analyze the strain of the 3DRRM in the same conditions as in the reality.

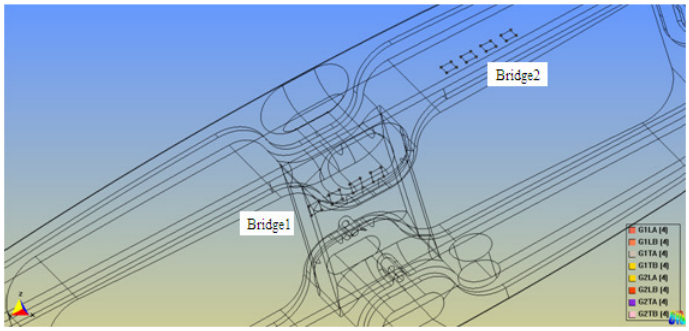

Figure 6.7. Strain gauges

Constraints and boundary conditions

The boundary conditions have been applied to reproduce the actual constraints, as explained in the following picture.

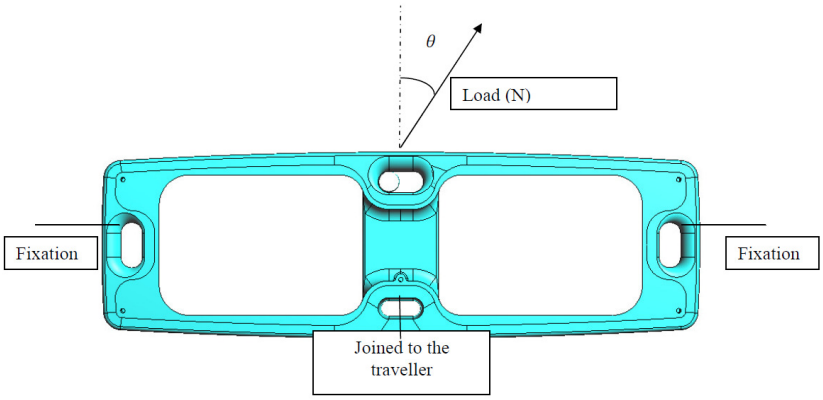

Figure 6.8. Real constraints

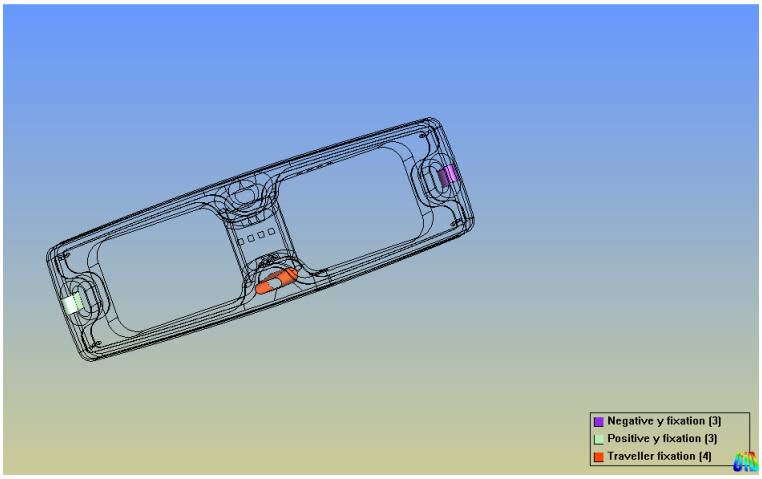

Figure 6.9. Fixed constraints

The fixation surfaces have restricted the movement in the longitudinal direction of the element (y axis) and the traveler fixation surface has restricted the movement in the vertical and transversal direction (x and z) axis.

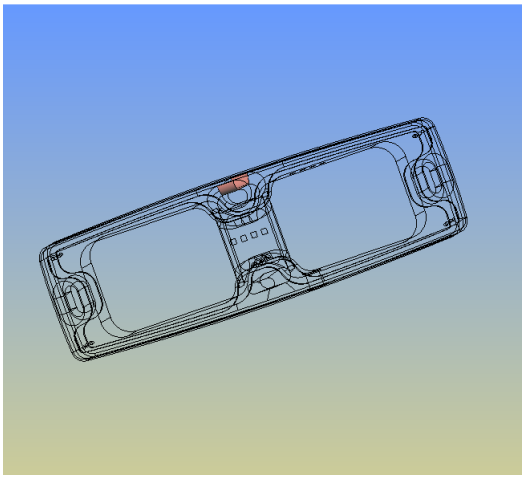

Figure 6.10. Surface where the load is applied

The surface with colour is where the load will be applied as a pressure.

Work range

The load has been varied from $1000N$ to $7000N$, with intervals of $1000N$, combined with the variation of the angle $0°, 20°$ and $40°$, resulting twenty-one simulated cases, that are presented below.

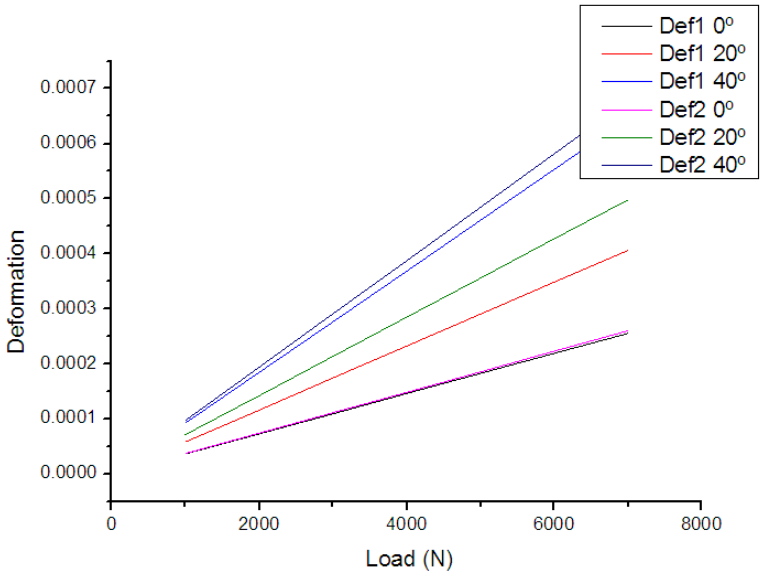

Figure 6.11. Load/Angle/Strain

Neural Network

With all these data, it is possible to adapt an ANN, to obtain the load and the angle of the sheet from the measured strain of the device.

In the following the results of three different configurations of ANNs are showed. We have been tried configurations with three neurons, four neurons and five neurons at the hidden layer. The graphs showed at Figure 6.12 and Figure 6.13 represents at abscissa axis the 'experimental' load or angle, and vertical axis shows the load or angle resulting from the neural network. The best adjustment of a neural network must give a perfect linear regression with unity slope.

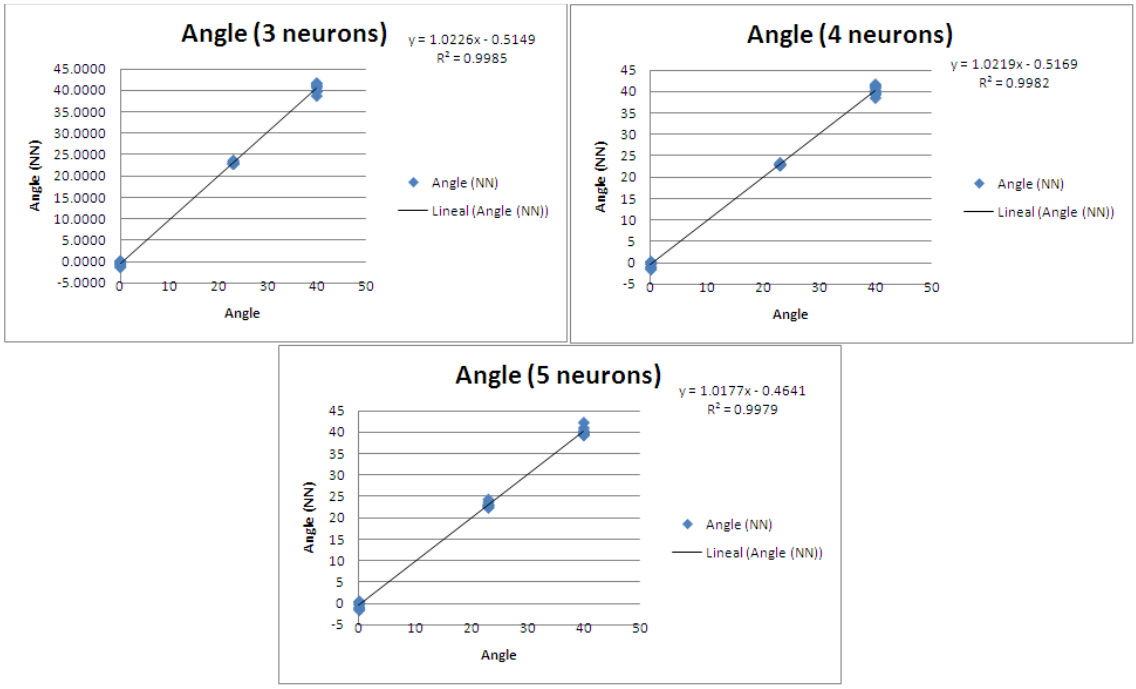

Figure 6.12. Neural Network Results for angle

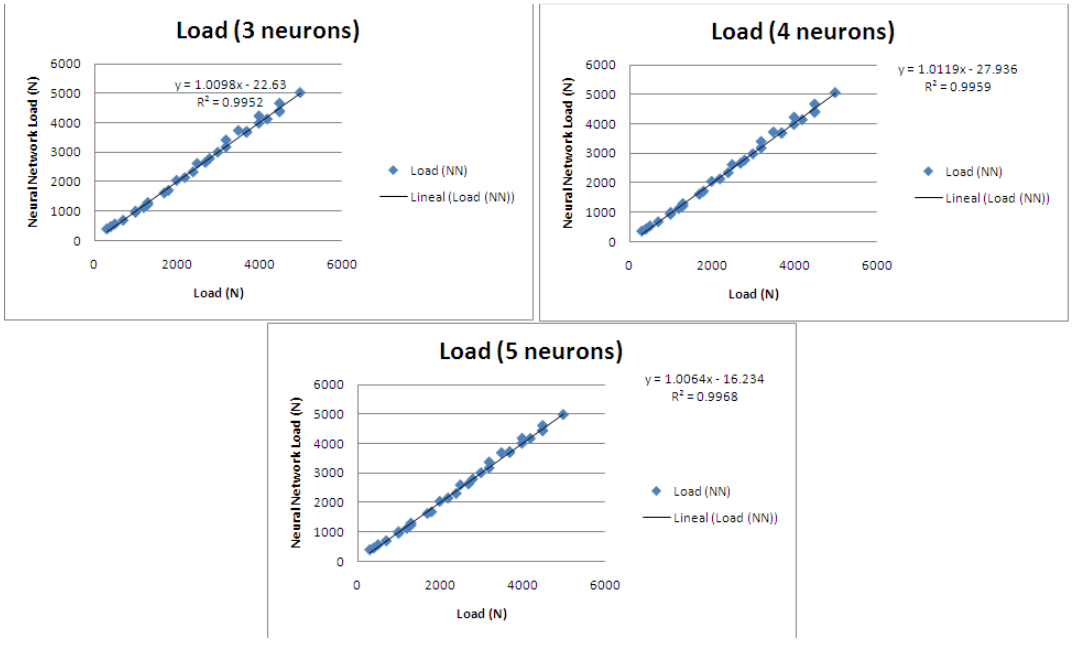

Figure 6.13. Neural Network for Load

The best neural network adjust is obtained with the configuration of five neurons at the hidden layer.

Waspmote has integrated a GPS which could be used to determine the traveler position, but it has not been proved. If this GPS will not be useful for this purpose, the position of the traveler could be determined by the angle of the sheet. Although, the position of the traveler will be introduced manually.

6.2.2 Back Stay, Forward Stay and Shrouds

In this section we will analyze the integration of the 3DRRM in the back stay, in the forward stay and in the shrouds. The CAE model and the boundary conditions are the same for the three positions, therefore only one case will be analyse as example, the case of the back stay.

CAE model

The CAE model is shown in Figure 6.14.

Real constraints and boundary conditions

It has been supposed that the 3DRRM of the back stay is fixed to the deck, so one side will be fixed and on the other side will be fixed to the stay.

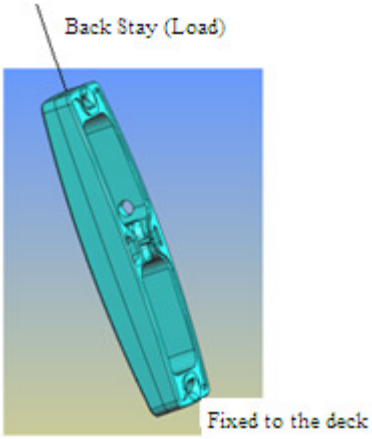

Figure 6.14. Real Constraints

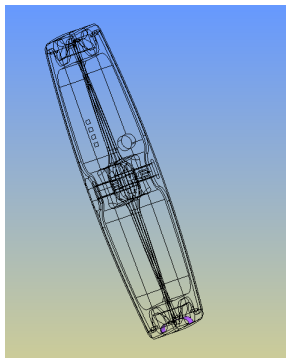

Figure 6.15. Fixed Constraint

The fixed surfaces have the movements restricted.

Work range

The stay will keep a constant angle, so the 3DRRM's strain will just change with the load of the stay. The load of the stay is determined by the type of boat. In our case,

we will use a reference value for a GP42 sailing yacht of $25kN$. The simulations have been made varying the load from 20kN to 30kN.

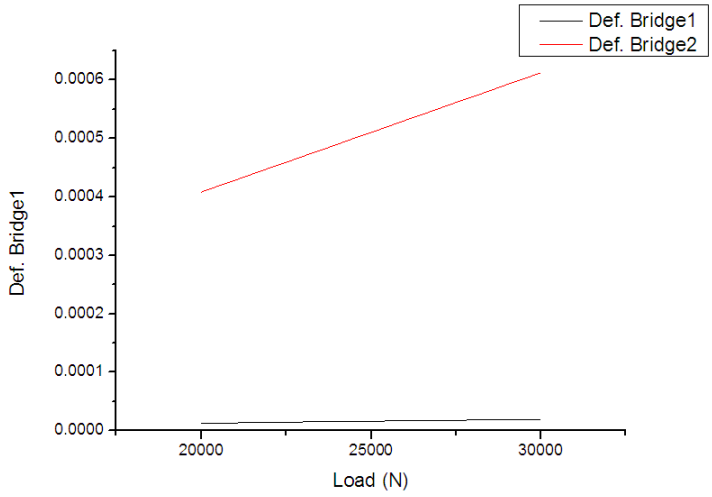

Figure 6.16. Relation between the 3DRRM's strain and the load of the stay

Neural Network

Once the results of the different studied cases are obtained, we can proceed with the fitting of the ANN, to obtain the load of the back stay from the 3DRRM's strain.

For this case, the strain of the 3DRRM is related only with the load. Figure 6.17 shows the relation between the strain and the load, and this relation is clearly lineal. As expected, the strains measured by the Bridge2 are bigger than the strains measured by the Bridge1. So it seems reasonable to use the results for Bridge2 to define a linear relation between the strain and the load.

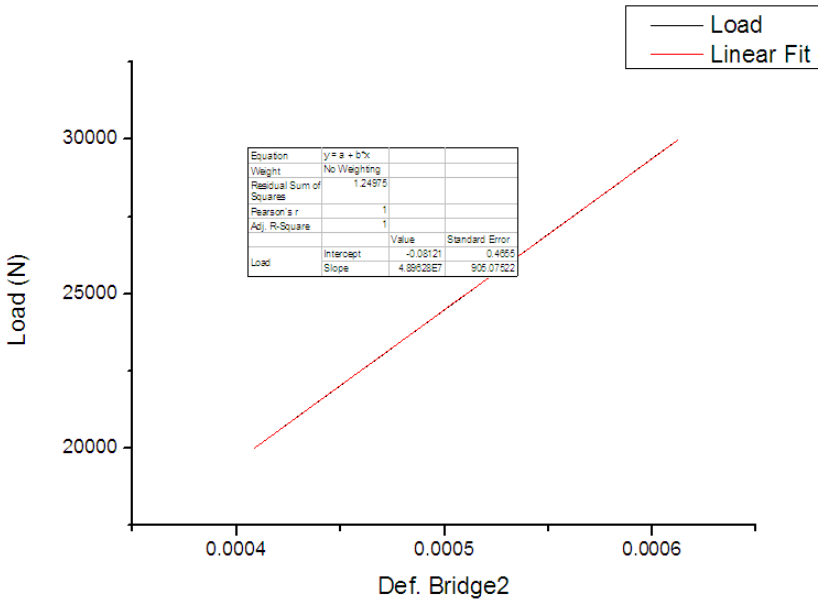

Figure 6.17. Formula to calculate the load through the strain of the bridge 2

Since the material is in linear elastic range, so this linear relation was an expected result. At this case this relation can be established easier than adapting a neural network. The resulting function is $y \approx 4.89 \cdot 10^7 x$, where y will be the load (N) and x the strain at bridge2 $\left(\Delta l/l\right)$.

This result has been obtained for the back stay, but considering that the material is working in its linear elastic range, the use of this linear function can be generalized for the forward stay and for shrouds.

6.3 Sensor and Software link

Our goal is to be able to calculate 'in real time' the response of the sails depending of the trim that the crew is applying and depending of the wind intensity and angle. The trim parameters and the wind speed and angle are the 'external' boundary conditions of the FSI program:

- Load in shrouds.
- Load in stays.
- Load and angle in main sheet
- Load and angle in jib sheet
- Position of the main traveler
- Position of the jib traveler

These parameters are obtained by the 3DRRM arranged to the boat.

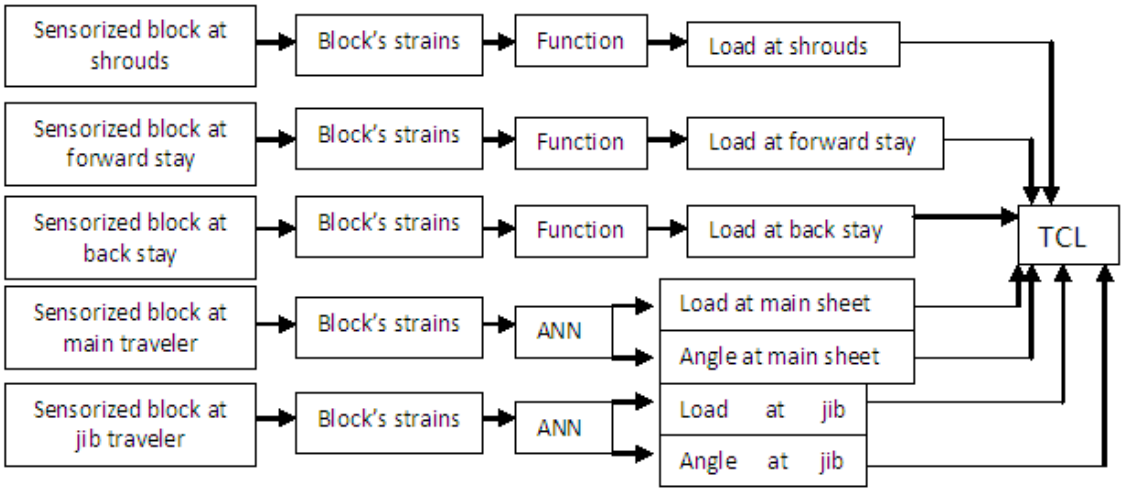

Figure 6.18. Treatment of the sensor data

These data are the 'external boundary conditions' of the FSI software and to insert these parameters in each new calculation of the program, a C interface for TCL[23] has been implemented.

6.4 TCL Interface

The resulting *Sailing* tool integrates three principal elements:

1) The GUI, based on GID system, presented at Appendix B, where the geometry and the boundary conditions of our sailing yacht can be defined.

2) The FSI solver to compute the performance of the sailing yacht configuration.

3) The WSN data, which are transformed by neural networks or by linear function to define the 'external boundary conditions' of the yacht rigging.

4) A communication interface for interfacing 3DRRM data with the calculation program.

The communication between the 3DRRM data with the calculation program is managed by a TCL script. In order to access to the FSI solver data structure from an external TCL script, a C interface has been implemented in the calculation code. This interface has the function of reading the 'external initial conditions' from a file named 'script.tcl' and changing the geometry how is appropriate. Furthermore, this script can access the 'real time' data obtained by the WSN, and update accordingly the geometry and external boundary conditions to be applied to the FSI solver by using predefined procedures.

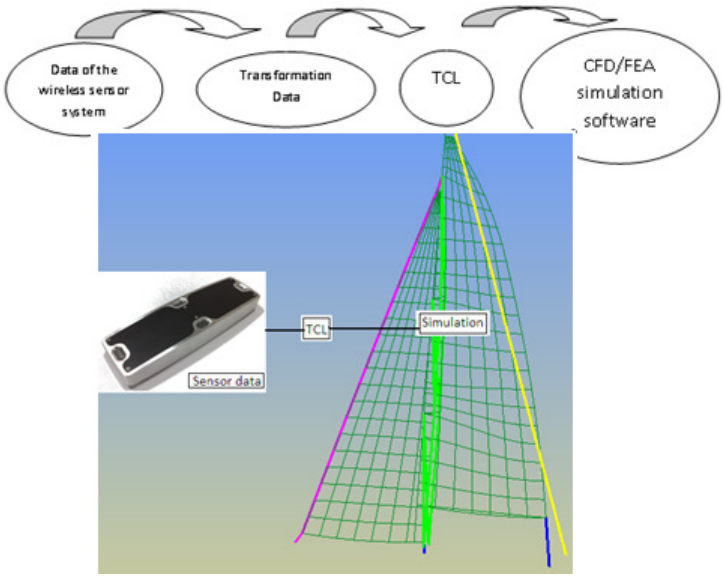

Figure 6.19. Calculation process

[23] TCL (Tool Command Language) is a dynamic programming language, suitable for a very wide range of uses.

An example of this file, 'script.tcl', is showed in the following:

```
proc TdynTcl_StartTimeStep {} {
global i
TdynTcl_SetTimeSteps 1
set i [TdynTcl_GetCurrentStep]
TdynTcl_Message "TdynTcl_StartTimeStep i= $i" notice
}

proc TdynTcl_StartPotential {} {
global i
TdynTcl_Message "TdynTcl_StartPotential i = $i" notice
TdynTcl_SetTimeSteps 1
TdynTcl_SetCurrentStep $i
TdynTcl_SetRotation 1
#First It is necessary to indicate the index of the nodes those
belong to the main traveller and to the jib traveller
TdynTcl_SetMainRailNode 1
TdynTcl_SetJibRailNode 32
# It is necessary to give the traveller position
TdynTcl_SetNewMainRailPosition 0.58763044 0.051409469 -0.01200894
TdynTcl_SetNewJibRailPosition 0.034940626 0.094158798 -0.16721009
#It is necessary to give the index of the nodes those belong to the
bottom and the upper side of the forward stay
TdynTcl_SetJibStayNode 392 195
#It is necessary to indicate the index of the node at the upper part
of the mast
TdynTcl_SetMastUpNode 442
}

proc TdynTcl_StartStructure {} {
global i
TdynTcl_SetTimeSteps 1
TdynTcl_SetCurrentStep $i
TdynTcl_SetRotation 1
TdynTcl_Message "TdynTcl_StartStructure i = $i" notice
#First It is necessary to indicate the index of the nodes those
belong to the main traveller and to the jib traveller
TdynTcl_SetMainRailNode 1
TdynTcl_SetJibRailNode 32
# It is necessary to give the traveller position
TdynTcl_SetNewMainRailPosition 0.58763044 0.051409469 -0.01200894
TdynTcl_SetNewJibRailPosition 0.034940626 0.094158798 -0.16721009
#It is necessary to give the index of the nodes those belong to the
bottom and the upper side of the forward stay
TdynTcl_SetJibStayNode 192 195
#It is necessary to indicate the index of the node at the upper part
of the mast
TdynTcl_SetMastUpNode 442
#It is possible to indicate the state of any rope of the sail yacht
TdynTcl_SetCableState 4 3 25000
TdynTcl_SetCableState 3 3 20000
TdynTcl_SetCableState 1 3 3500
TdynTcl_SetCableState 2 3 3200
TdynTcl_SetCableState 5 3 1200
}
```

The calculation algorithm is composed of two parts, the FS calculation and the SS calculation and these calculations can be made separately or jointly. Each part has a process to initialize, which is called when the execution of each part starts.

- proc TdynTcl_ StartTimeDtep : here it is necessary to indicate the number of calculations to do. The number of time steps must be indicated with the order

- proc TdynTcl_StartPotential: here it is necessary to indicate all the parameters related with the FS calculation: wind and angle velocity, position of the travelers, indexes of the nodes that define stays and the uppers node of the mast.
- proc TdynTcl_StartStructure: here it is necessary to indicate all the parameters related with the FEA calculation: position of the travelers, the indexes of the nodes that define stays, the uppers node of the mast and the load at the ropes.

6.4.1 TCL interface: commands

TdynTcl_SetTimeSteps totalsteps: fix the toal number of steps to execute.
Example: TdynTcl_SetTimeStep 2

TdynTcl_SetRotation 0/1: 0 if sails are fixed, 1 if the travellers move.
Example: TdynTcl_SetRotation 0

TdynTcl_SetMainRailNode index: fix the node index that correspont to the main traveller node. Example: TdynTcl_SetMainRailNode 164

TdynTcl_SetGenoaRailNode index: fix the node index that correspont to the jib traveller node. Example: TdynTcl_SetGenoaRailNode 165

TdynTcl_SetNewMainRailPosition CoorX CoorY CoorZ: fix the coordinates of the main traveller. Example: TdynTcl_SetNewMainRailPosition 6.22 -0.14 -0.59

TdynTcl_SetNewGenoaRailPosition CoorX CoorY CoorZ: fix the coordinates of the main traveller. Example: TdynTcl_SetNewGenoaRailPosition 0.45 -0.675 -0.50

TdynTcl_SetGenoaStayNode StayDown StayUp: fix the index of the nodes those correspond to the uppers and downest part of the forward stay.
Example: TdynTcl_SetGenoaStayNode 1060 1020

TdynTcl_SetMastUpNode MastUp: fix the index of the node that corresponds to the uppers part of the mast. Example: TdynTcl_SetMastUpNode 300

TdynTcl_SetWindvelocity Vx Vy Vz: fix the value of the vector wind components.
Example: TdynTcl_SetWindVelocity 3 -7.40 5

TdynTcl_SetCableState typeelement typestate statevalue: fix the stress state at the cable type (typeelement. Typeelement=1 is for indicating MainSheet. Typeelement=2 is for indicating JibSheet. Typeelement=3 is for indicating BackStay. Typeelement=4 is for indicating ForeStay. Typeelement=5 is for indicating Shrouds.), typestate can be 1, 2 or 3 dependig of the units of the state. Statevalue fix the value of the stress.
Example: TdynTcl_SetCableState 1 1 0.02

TdynTcl_SetCableAngle typeelement angle: fix the angle (in degrees) at the typeelement. (Typeelement=1 for indicating MainSheet and typeelement==2 for indicating JibSheet)
Example: TdynTcl_SetCableAngle 1 30

6.5 Trimming algorithm

Once the trimming parameters have been sent to the FSI solver, it is necessary to update the geometry according to these trimming parameters.
We have two types of trimming parameters, the loads and angles at the ropes and the position of the main and jib traveler. In the following sections we will introduce the procedure to apply the boundary conditions and constrains defined by those parameters.

6.5.1 Loads and angles

The load and angle at the ropes are comunicated directly to these elements, by the commands **TdynTcl_SetCableState** and **TdynTcl_SetCableAngle**. The command **TdynTcl_SetCableState** comunicate to our program *Sailing* the force at the different cables, whose have been taken by the 3DRRM. And the command **TdynTcl_SetCableAngle** comunicates the angles at the main sheet or at the jib sheet.

6.5.2 Rotation algorithm

The crew move the travelers, main traveler and jib traveler, depending of the aparent angle of the wind. Our program is thought to be used during navigation, so then, these movements must be reproduced ‘virtually’ in our geometry.
In order to introduce in *Sailing* the capability of adapt the position of the sails, an algorithm has been introduce into the FSI solver to move the sails as the sailing yacht.
A simplified process has been selected, following the line presented by Graft and Renzsch(Graf, 2006). A particular trim of the sail is carried out by rotating the jib around the forward stay and the main sail around the mast.

6.6 An application case

To finish the chapter, we will present an example of application to the Totalboats GP42 yacht, where the 3DRRM has been integrated.

Figure 6.20. GP42 yacht, where 3DRRM will be implemented

The geometry of the sail plan and rigging of this boat has been reproduced into *Sailing*.

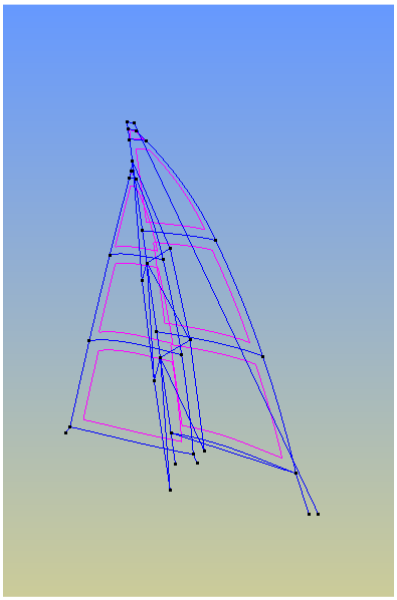

Figure 6.21. Model of the GP42 yacht in Sailing

Therefore, we will assume a starting state of the rigging defined by the following parameters.

- Initially, the velocity of the apparent wind is 8 m/s and the apparent angle is 15º.
- The main traveler is located at the point (6.22,0.34,-0.59). It is, the trim angle of the main sail is $\delta_M = 3.25°$.
- The jib traveler is located at the point (0.41,0.88,-0.50). It is, the trim angle of the jib is $\delta_J = 8.9°$.
- The load in the main sheet and jib sheet is 1500 N and 700 N respectively..
- The load in the back stay is 10000 N.
- The load in the fore stay is 20000 N.
- The load in the shrouds is 1000 N.

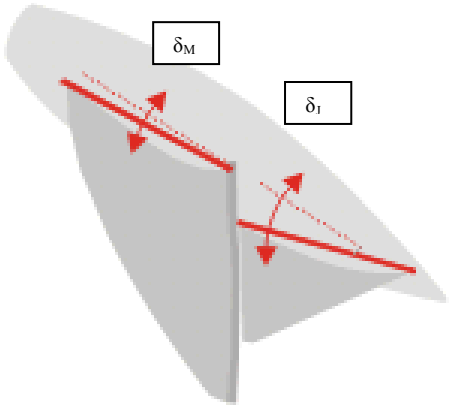

Figure 6.22. Trim angles

In Figure 6.23 we can see the results for an apparent wind angle of 15°. It is necessary to emphasize the areas where the pressure coefficient has an abnormal value, a negative value. This abnormal value can be attributed to two reasons: the flow is turbulent or separate in these areas or these areas are flapping.

To study the effect of the apparent wind angle, it is increasing to 20°. The response of the previous structure is shown in the Figure 6.24. It is possible to see the change in the pressure coefficient and the areas with the abnormal value in the pressure coefficient.

The separated or turbulent flow in the head of the sails is related with the effect of the trim angle of the jib δ_J and the trim angle of the main δ_M. Marchaj (Marchaj, 2003) suggest that the best position for the foresail relative to the main and its trim angle, is different depending on the apparent wind angle. At various times, the correct close-hauled angle of trim of the foresail has been recommended as being anything from $7° < \delta_J < 20°$. He made different tests in the wind tunnel at Southampton University, and proved that to obtain a high aerodynamic efficiency, the flow on the leeward side of the sail must be attached and steady. These tests demonstrated that at the small apparent wind angle of 20°, when $\delta_J = 10°$ and $\delta_M = 5°$, attached flow occupies the major part of the both sails and. When the apparent wind angle increase to 25° and the trim angles are the same, $\delta_J = 10°$ and $\delta_M = 5°$, the regions with turbulent flow and separated increases.

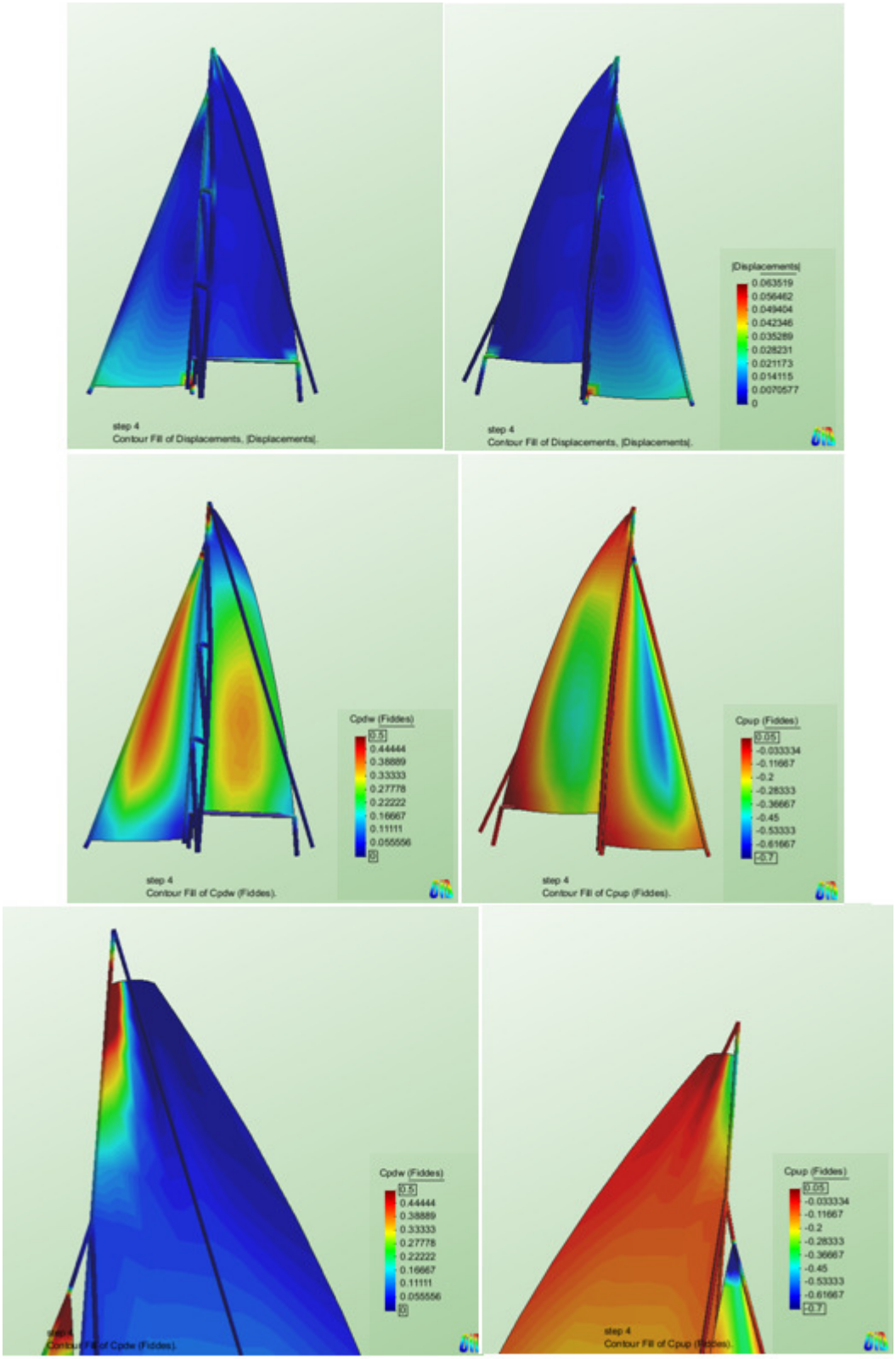

Figure 6.23. Displacements, Cp and abnormal area for an apparent wind angle of 15º

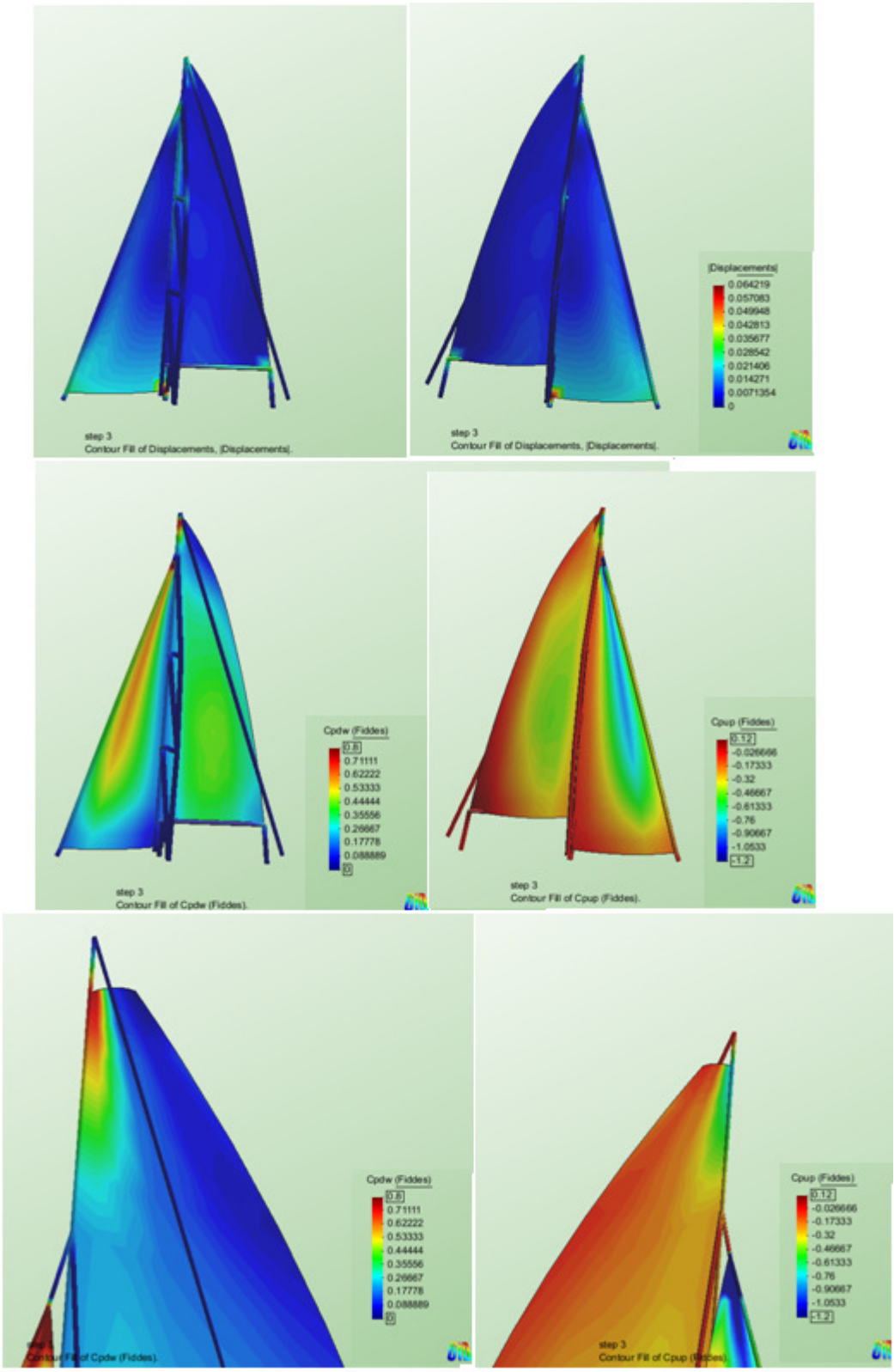

Figure 6.24.Displacements, Cp and abnormal area for an apparent angle of 20º

Now, the wind condition change, therefore the crew trim the sails. These new trim parameters are detected by the integrated 3DRRM, and they are:

- Apparent wind condition 10 m/s and 20º.
- New main traveler position (6.22, 0.63, -0.59).
- The new position of the jib traveler is (0.37, 1.095, -0.5).
- Load of the shrouds 1200 N.
- Load in the back stay 15000 N.
- Load in the fore stay 22000 N.
- Load in the main sheet 2000N.
- Load in the jib sheet 1000 N.

These changes are introduced into Sailing by the TCL interface and the 'virtual geometry' is adjusted to these trim parameters.

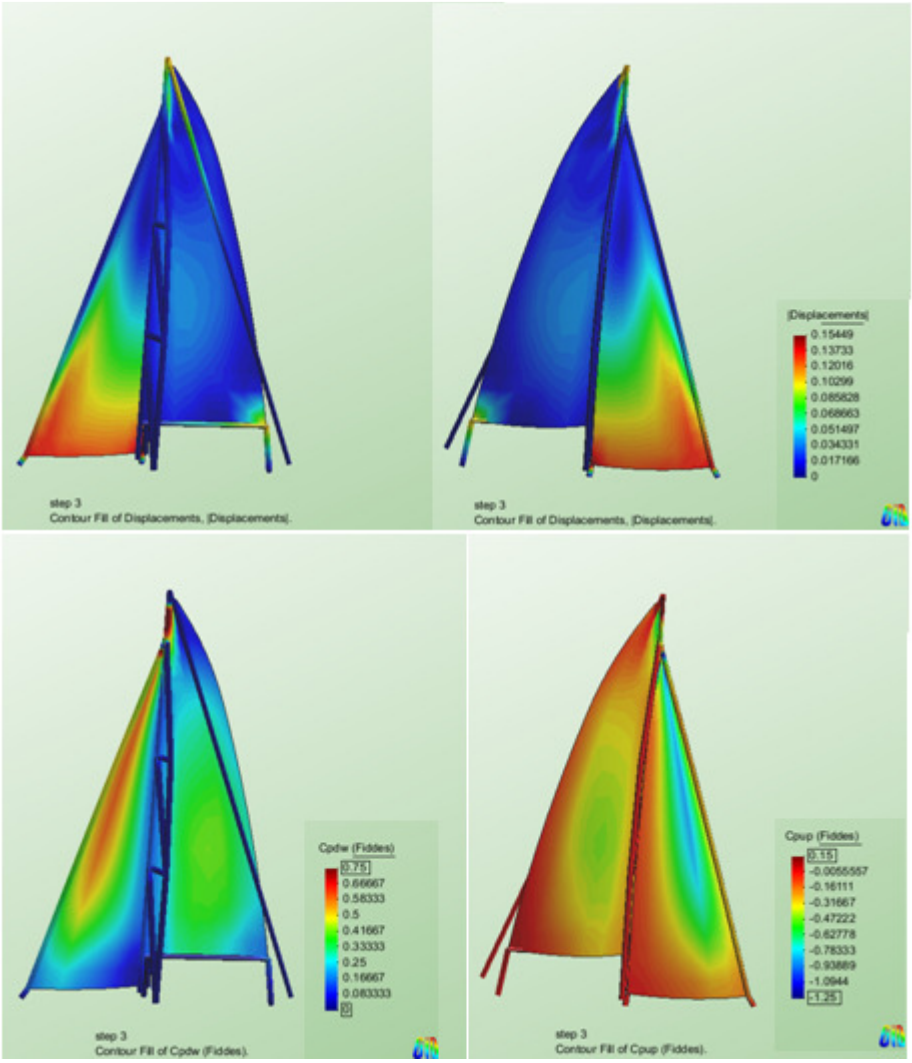

Figure 6.25. Displacements and Cp for and apparent wind angle of 20º

As in the previous case, it is possible to study the influence of the apparent wind angle in the displacements and Cp of the structure. The following images show the different results for the same structure for an apparent wind angle of 25° and 30°.

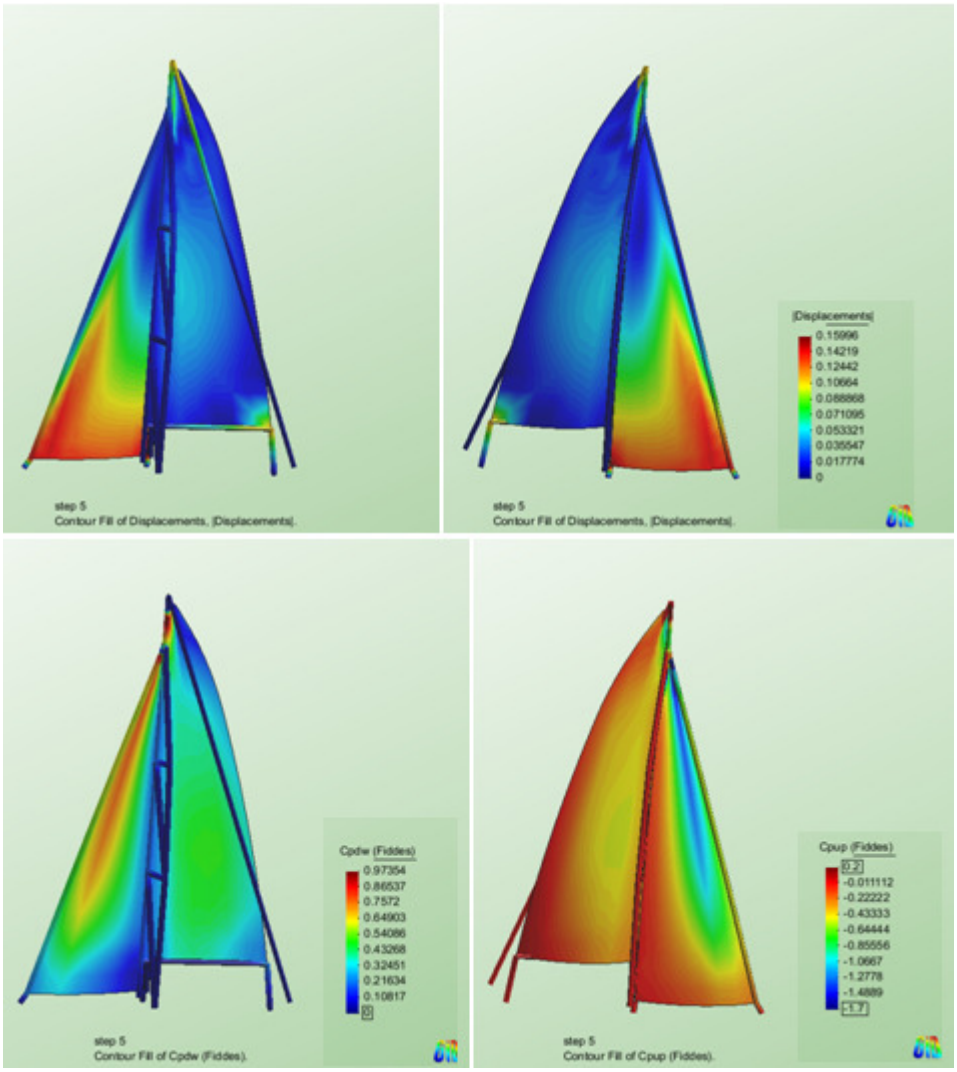

Figure 6.26. Displacements and Cp for an apparend wind angle of 25º

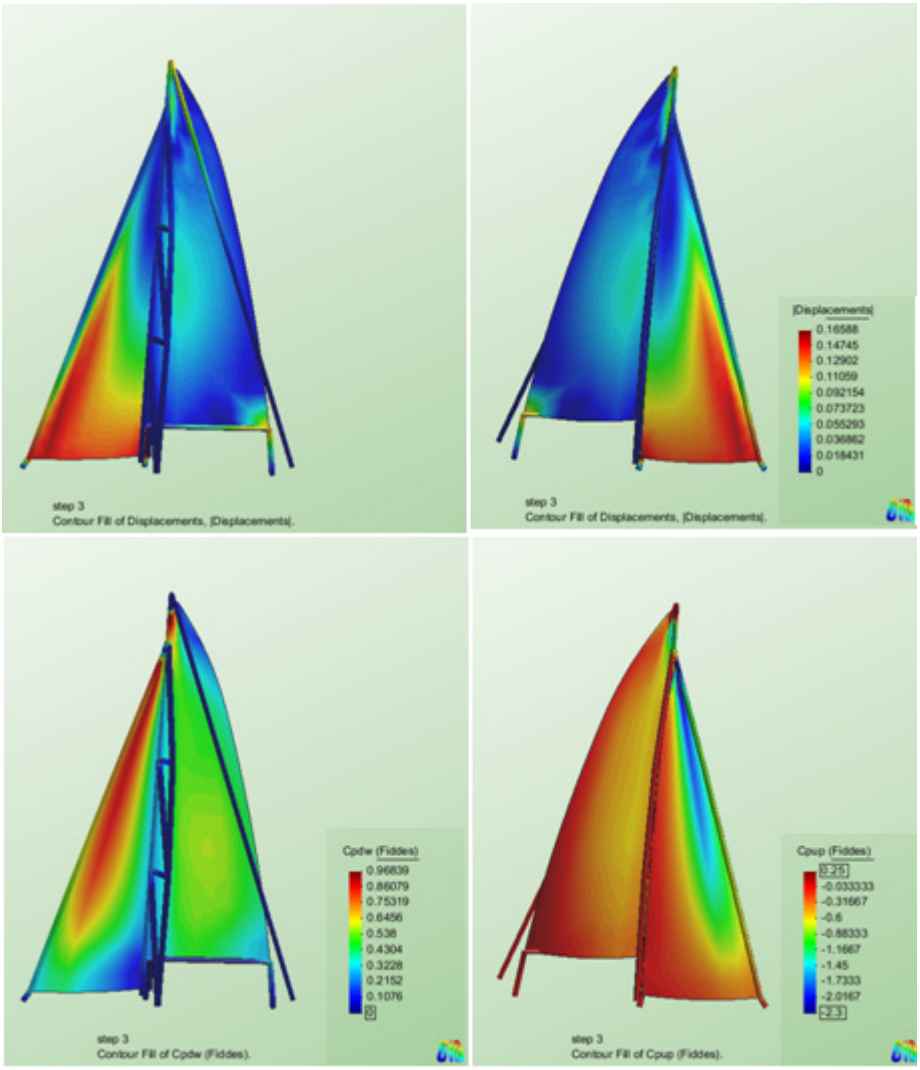

Figure 6.27. Displacements and Cp for an apparent wind angle of 30º

6.7 Conclusions

Here, the versatility of the 3DRRM has been proved. The different configurations (shrouds, back stay, fore stay, main sheet and jib sheet) has been presented and analyzed to obtain the load at each one of them, by the strain of the 3DRRM. Therefore, all the rigging elements can be monitored.

The data obtained by the 3DRRM are communicated through the TCL interface, and the geometry can be trimmed virtually. The calculation of the FSI software can be executed with the new parameters and can be determined if these trimming parameters are then appropriate.

The integration of the FSI solver and the TCL interface, presented at this chapter, make up the program named *Sailing*. The user guide of the program is presented at Appendage B.

7 Conclusions

The main objective of this thesis is to develop a simulation program of the behaviour of sails and rigging, to help the crew to optimize the performance of the sailing yacht in real time. For this purpose, we have developed *Sailing,* integrating a Fluid Solver, a Structural Solver and a TCL communication interface with a rigging monitoring system, which is able to compute the performance of a particular sail/rigging configuration. Since the crew dynamically trims the rigging and sails, in order to evaluate the performance of the actual configuration, a tool to monitor the rigging and sails has been developed, 3DRRM. The crew manoeuvre is simulated communicating the integrated 3DRRM with *Sailing.* Once the sail/rigging configuration has been adapted 'in real time' to the actual one, the performance of this new configuration can be computed.

First, the FSI solver has been presented and validated. This FSI solver is able to compute the performance of a given rigging/sail configuration. Following this, the developed device (called 3DRRM) to monitor any rope or cable of the sailing yacht was presented and validated. With the data acquired from this tool, it is possible to obtain all the trimming parameters, treating the data obtained at each sensorized element of the sailing yacht as it is necessary. Integrating these tools it is possible to monitor the rigging and sails and compute the performance of the rigging/sail configuration during the sailing, taking into account the trim introduced by the crew.

3DRRM are integrated in the boat and they communicate the trimming parameters to *Sailing*. *Sailing* trims the geometry as the crew trim the real geometry and calculate the performance of this trim in near-time. It is necessary to remark that the standard calculations times ranges from a few minutes of a netbook Atom N450 processor to a few seconds of a workstation. A future work regarding this matter is the implementation of GPU solvers to reduce the calculation time. Though, it is necessary to consider the fact that, when the crew trim the sails, these pass of an equilibrium state to other state, and this new state need a time to be a new equilibrium state. So then, we can consider that *Sailing* is able to give information in 'real time' (aerodynamic coefficients) to the crew for deciding if the trimming is adequate. This monitoring in real time is an innovation for navigation, especially for the races.

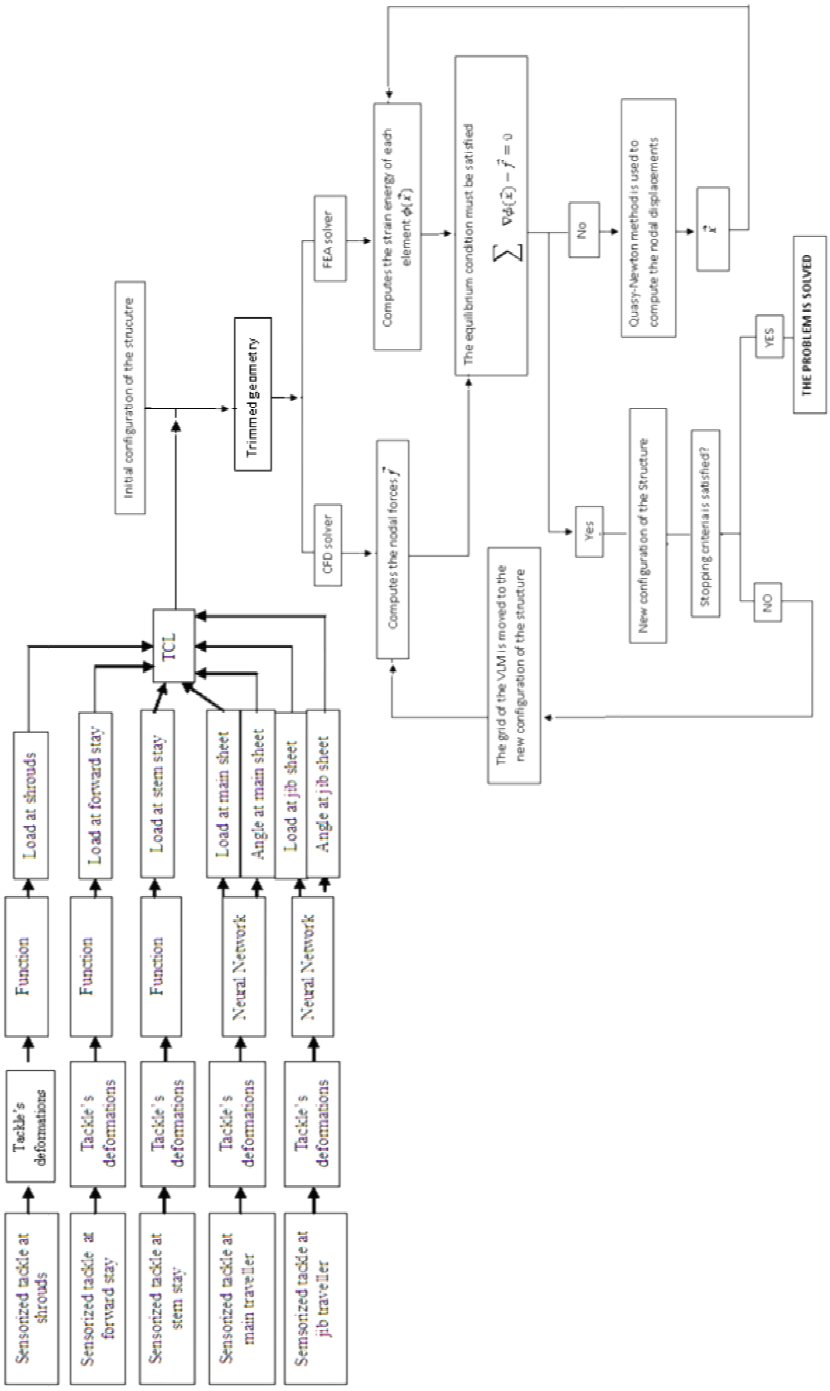

Figure 7.1. Scheme of the integration of all the elements that make up our software.

The original aspects of this thesis are:

- The communication between the sensors and the FSI algorithm. The sensors capture the trim parameters and they are communicated to the FSI algorithm to adjust the structure to these trim parameters. That is, there is a consideration 'in real time' of the manoeuvre parameters into the analysis of the fluid structure interaction. The parameters to consider will be: angle to

the wind, foresail sheet's stress and position, mainsail sheet's stress and position, stress at the stays and shrouds.

- The development of a tool to work in real time, which allows establish the coupled behaviour of the flow and the structure. This tool can be very useful for the crew during the navigation to known, the efficiency of their trim and to know the state of the rigid structure to avoid problems as the breakage of the mast.
- The concept of a new kind of wireless and adaptable sensor. Since now, all the sensors developed for a sailing yacht are thought for a specific yacht. Our innovation is the versatility of our monitoring tool.

The performance of the software cannot be validated with experimental data, because these are very scarce. This is mainly due to two factors: (a) the difficulty of measuring the deformed shape of a sail and the wind pattern producing the strain and (b) the transient character of the phenomena involved, which makes the measurement of the exact instantaneous sail shape/wind pattern difficult. Performing full scale test of sail and rigging is out of the question due to the dimensions necessary for the wind tunnel: on the other hand, model test would not be reliable for extrapolation at full scale due to the difficulty of simulating the elasticity of sail and rigging. Thus, the validation done in this work with several benchmarks is the only possibility. This validation work has shown that the accuracy of the simple model proposed could be enough for practical purposes.

In spite of considering this program to be a fast and sufficiently accurate tool, it is possible to improve it. So, the following are the possible improvements that could be introduced, which will be considered as future work.

- The sailing vessel is not manoeuvrable with the sails alone, because it is not sufficient to drive the boat in any desired direction. Sailboats overcome this by using the physical portion of the boat that is below the water, and that can be regarded as functioning as a 'second sail'. Having two surfaces against the wind and water enables the sailor to travel in almost any direction and to generate an additional source of lift from the water. The flow of water about the underwater hull portions creates a hydrodynamic force. The combination of the aerodynamic force from the sails and the hydrodynamic force from the underwater hull section allows motion in almost any direction. So, the consideration of hull interaction will be an implementation to consider in the future.
- Wind shear affects sailboats in motion by presenting a different wind speed and direction at different heights along the mast. Wind shear occurs because of friction above the water surface slowing the flow of air. Thus, a difference in true wind creates a different apparent wind at different heights. Sailors may also adjust the trim of the sail to account for wind gradient. It will be possible to consider the logarithmic distribution of the wind velocity to increase the accuracy of the predictions.

- The flow considered is steady and the sail operates in a natural environment characterized by unsteadiness and complex perturbations (atmospheric turbulence and complete motions of the yacht caused by sea-wave excitation). The unsteady computation of flows around sails assumes rigid motions of the structures. Nevertheless, shape variations and elastic strains of the sail can strongly affect the complete dynamic of system, but the resolution of the interaction involves many geometrical difficulties connected to the large displacements and nonlinearities.
- It would be possible to consider the viscosity of the flow. A simple strip-based integral boundary layer method could be used to give some estimate of the profile drag levels on the sails.
- The heel angle modifies the lift coefficient, and if the heel angle is monitored, could be possible to insert this effect in the numerical model.
- *Sailing* does not consider the separation of the flow, so it could be used by boats which have been optimized for upwind performance, at typical angles of 35° to the true wind. Actually, the implemented FS tool is only valid for upwind sails and the extension to analyse downwind sails is a pending work.
- The tool presented in this work could be the aerodynamic part of a Velocity Prediction Program (VPP). Most VPP use wind tunnel test data made with the different sail/rigging configurations to calculate the sail-force coefficients. For this application, the combined tool will be an interesting innovation, because it will be able to calculate the sail-force coefficients for the sail/rigging configuration 'in real time'. This tool could calculate these coefficients for any boat, using the rigging structure and the basic sail shape (the shape given by the designer).

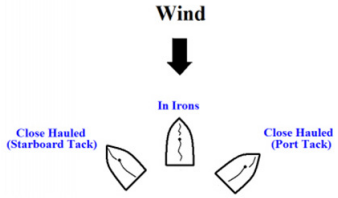

Figure 7.2. Close hauled navigation

- It had been presented before the capacitive differential pressure transducer, suitable to be implemented in a wireless sensor network for wind sail monitoring. The network is aimed at sensing the pressure field acting on the surface of a sail by means of instrumented battens, providing the real-time differential pressure map over the sail surface. This technology would be a good complement for our rigging monitoring system.
- Finally, one of the main future actions is the exhaustive testing and evaluation of the system in real applications. Currently, an implementation of Sailing is being installed and tested in the GP42 yacht presented in previous chapters.

Appendix A: Potential Flow

A.1 Governing equations

The equations that govern any material state that can be considered continuous are based in empiric conservation laws of continuity, moment and energy. The velocity of the flow around the sails is relatively slow, so the fluid can be considered incompressible.

To develop the mathematical equations that govern these flows and the tools that will be necessary to solve the equations, it is necessary to study rotation in the fluid and to demonstrate its relationship to effects of viscosity.

The mass conservation equation that governs a fluid is:

$$\left.\begin{cases} \frac{D\rho}{Dt} + \rho\nabla\cdot\vec{V} = \frac{\partial\rho}{\partial t} + \vec{V}\cdot\nabla\rho + \rho\nabla\cdot\vec{V} = 0 \\ \frac{D\rho}{Dt} = 0, incompressible\ fluid \end{cases}\right\} \nabla\cdot\vec{V} = 0 \qquad \text{A. 1}$$

The moment conservation equation is:

$$\frac{D\vec{V}}{Dt} = -\frac{\nabla p}{\rho} + \upsilon\nabla^2\vec{V} \qquad \text{A. 2}$$

Outside the boundary layer the viscous effects are negligible so, the moment equation will be:

$$\frac{D\vec{V}}{Dt} = -\frac{\nabla p}{\rho} \qquad \text{A. 3}$$

The movement of a fluid element has three components, translation, rotation and strain.

$$\vec{V} = (u, v, w) \quad \vec{w} = \frac{1}{2}\nabla\times\vec{V} \qquad \text{A. 4}$$

The vorticity is defined so two times the angular velocity

$$\vec{\Omega} = 2\vec{w} = \nabla\times\vec{V} \qquad \text{A. 5}$$

If is considered an open surface, which has a closed curve C has his boundary. With the use of the Stoke theorem the vorticity on the surface can be related to the line integral around C.

$$\int_S \nabla\times\vec{V}\cdot\vec{n}\,dS = \int_S \vec{\Omega}\cdot\vec{n}dS = \oint_C \vec{V}\cdot d\vec{l} \qquad \text{A. 6}$$

The vector is normal to the surface *S*. The integral on the right-hand side is called the circulation and denoted by Γ.

$$\Gamma = \oint_C \vec{V}\cdot d\vec{l} = \int_S \nabla\times\vec{V}\cdot\vec{n}dS = \int_S \vec{\Omega}\cdot\vec{n}dS \qquad \text{A. 7}$$

Circulation is the vorticity net flow through a surface described by a close curve.

Considering the shear forces in the fluid very large, the fluid turns like a solid body, in this case and the fluid is called rotational. However, if the shear forces in the fluid are negligible, and the fluid will not be rotated by shear force of the neighbouring fluid element, , then the flow is considered to be irrotational.

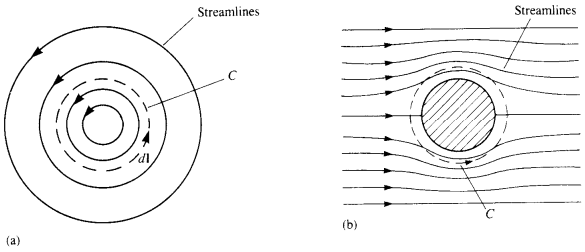

Figure A. 1 Flow field with (a) and without (b) circulation

The divergence of the vorticity is zero since the divergence of the curl of any vector is identically zero.

$$\nabla\cdot\vec{\Omega} = \nabla\cdot\nabla\times\vec{V} = 0 \qquad \text{A. 8}$$

Considering, at any instant, a region space *R* enclosed by a surface *S*. An application of the divergence theorem yields

$$\int_S \vec{\Omega}\cdot\vec{n}dS = \int_R \nabla\cdot\vec{\Omega}dV = 0 \qquad \text{A. 9}$$

At some instant in time draw a vortex tube in the flow.

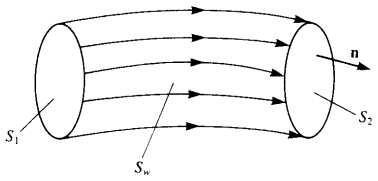

Figure A. 2. Vortex tube

Apply the last equation to the region enclosed by the wall of the tube S_w and the surfaces S_1 and S_2. Since on S_w the vorticity is parallel to the surface, the contribution of S_w vanishes.

$$\int_S \vec{\Omega}\cdot\vec{n}\,dS = \int_{S_1} \vec{\Omega}\cdot\vec{n}\,dS + \int_{S_2} \vec{\Omega}\cdot\vec{n}\,dS = 0 \rightarrow$$
$$\rightarrow \int_{S_1} \vec{\Omega}\cdot\vec{n}\,dS = \int_{S_2} \vec{\Omega}\cdot\vec{n}\,dS = const. \qquad \text{A. 10}$$

S_1 and S_2 are closed curves that surround the tube and lies on its wall, the circulation around these sections will be equal, so the circulation is constant along the tube.

$$\Gamma = \int_{S_1} \vec{\Omega}\cdot\vec{n}\,dS = \int_{S_2} \vec{\Omega}\cdot\vec{n}\,dS = const. \qquad \text{A. 11}$$

Applying it to a vortex filament and $\vec{n}$ is a unitary in the direction of the filament, the circulation of the vortex filament is constant along the filament. A consequence of this result is that the vortex filament cannot start or en in the fluid.

Based on these results, Hermann von Helmholtz (1821-1894) developed his vortex theorems for inviscid incompressible flow:

- The strength of a vortex filament is constant along its length.
- A vortex filament cannot start or end in a fluid, it must form a closed path or extend to infinity.
- The fluid that forms a vortex tube continues to form a vortex tube and the strength of the vortex tube remains constant as the tube moves about.

A.1.1 Kelvin's Theorem

Considering the circulation around a fluid curve of an incompressible inviscid flow with conservative body forces acting. The time rate of change of the circulation of this fluid curve C is given as

$$\left.\begin{array}{l} \dfrac{D\Gamma}{Dt} = \dfrac{D}{Dt}\oint_C \vec{V}\cdot d\vec{l} = \oint_C \dfrac{D\vec{V}}{Dt}\cdot d\vec{l} + \oint_C \vec{V}\cdot\dfrac{D}{Dt}d\vec{l} \\ \dfrac{D\vec{V}}{Dt} = \vec{a} \qquad \dfrac{D}{Dt}d\vec{l} = d\vec{V} \end{array}\right\} \frac{D\Gamma}{Dt} = \oint_C \vec{a}\cdot d\vec{l} \qquad \text{A. 12}$$

From the Euler equation, valid for incompressible, inviscid fluids $\frac{D\vec{V}}{Dt} = \vec{f} - \frac{\nabla \mathrm{p}}{\rho}$ the acceleration can be obtained $\vec{a} = -\nabla\left(\frac{p}{\rho}\right) + \vec{f}$. With these result can be demonstrated that the circulation of a fluid curve remains constant, knowing that the close integral of a perfect differential is zero and the work done by a conservative force around a close path is zero.

$$\frac{D\Gamma}{Dt} = \oint_C -\nabla\left(\frac{p}{\rho}\right)\cdot d\vec{l} + \oint_C \vec{f}\cdot d\vec{l} = -\oint_C d\left(\frac{p}{\rho}\right) + \oint_C \vec{f}\cdot d\vec{l} = 0 \qquad \text{A. 13}$$

This result is a form of angular momentum conservation known as *Kelvin's Theorem*, which states that: The time rate of change of circulation around a closed curve consisting of the same fluid element is zero.

Considering an airfoil, which prior was at rest and then at *t*>0 was suddenly set into a constant forward motion. As the fluid moves through the fluid a circulation $\Gamma_{airfoil}$ develops around it. In order to complain with Kelvin's theorem a starting vortex Γ_{wake} must exist such the total circulation around a line surrounding the airfoil and the wake remains unchanged.

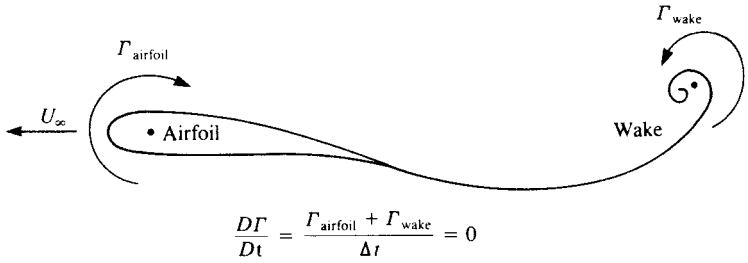

Figure A. 3. Circulation caused by an airfoil

$$\frac{D\Gamma}{Dt} = \frac{1}{\Delta t}\left(\Gamma_{airflow} + \Gamma_{wake}\right) = 0 \qquad \text{A. 14}$$

This is possible only if the starting vortex circulation equals the airfoil's circulation, but rotating in the opposite direction. So to take the wake into consideration is necessary to solve the dynamic problem of a fluid where is submerged a solid body

A.1.2 Laplace Equation

The vorticity in high Reynolds number is confined to the boundary layer and wake regions where the influence of viscosity is not negligible and so it's appropriate to assume an irrotational as well as inviscid flow outside these confined regions.

Consider a line integral in a simply connected region, along the line C:

$$\oint \vec{V}\cdot d\vec{l} = \int_C udx + vdy + wdz \qquad \text{A. 15}$$

If the flow is irrotational in this region, $udx + vdy + wdz$ is an exact differential of a potential that is independent of the integration path and is a function of the location of the point $P(x, y, z)$:

$$\phi(x,y,z) = \int_{P_0}^{P} u\,dx + v\,dy + w\,dz \qquad \text{A. 16}$$

Where P_0 is an arbitrary point of reference, ϕ is called the velocity potential, and the velocity at each point can be obtained as its gradient.

$$\vec{V} = \nabla\phi \qquad \text{A. 17}$$

This relation can be applied in the continuity equation of an incompressible fluid, $\nabla\vec{V} = 0$, it leads to the *Laplace Equation*

$$\nabla\vec{V} = \nabla \cdot \nabla\phi = \nabla^2\phi = 0 \qquad \text{A. 18}$$

For an irrotational, incompressible and inviscid fluid, the velocity field can be obtained as solution of the *Laplace Equation* for the velocity potential.

The *Laplace Equation* is a form of the incompressible continuity equation of an irrotational fluid. The *Laplace Equation* is a linear differential equation. Since the fluid's viscosity is neglected, the no-slip boundary condition on a solid-fluid boundary cannot be enforced and only the condition of zero normal velocity can be enforced. The boundary condition states that the normal component of the relative velocity between the fluid and the solid surface is zero on the boundary:

$$\vec{n} \cdot \left(\vec{V} - \overrightarrow{V_B}\right) = 0 \qquad \text{A. 19}$$

A.2 General solutions for the potential flow equations

For most engineering applications the problem requires a solution in a fluid domain V that usually contains a solid body. If the flow in the fluid region is considered to be incompressible and irrotational, the continuity equation is the Laplace.

$$\nabla^2\phi = 0 \qquad \text{A. 20}$$

For a submerged body in a fluid, the velocity component normal to the surface of the body must be zero.

$$\nabla\phi \cdot \vec{n} = 0 \qquad \text{A. 21}$$

$\nabla\phi$ is measured in a frame of reference attached to the body. Also, the disturbance created by the motion should decay far.

$$\lim_{r\to\infty}\left(\nabla\phi - \vec{V}\right) = 0 \qquad \text{A. 22}$$

Where $\vec{V}$ is the relative velocity between the undisturbed fluid and the body.

Because of the linear nature of the potential flow problem, the differential equations do not have to be solved individually for flow fields having different geometry at their boundaries. Instead, the elementary solutions will be distributed in a manner that will satisfy each individual set of geometrical boundary conditions.

The solution of *Laplace Equation* can be obtained by distributing elementary solutions (sources and doublets) on the problem boundaries (body surface S_B and wake surface S_W). These elementary solutions automatically fulfil the boundary conditions.

The general solution requires the integration of these basic solutions over any surface S containing these singularity elements because each element will have an effect on the whole fluid field.

The solution of a fluid dynamic problem is now reduced to finding the appropriate singularity element distributions over some know boundaries, so that the boundary conditions will be fulfilled. When the potential is specified on the problem boundaries then this type of mathematical problem is called the *Dirichlet Problem*.

A more direct approach to the solution, from the physical point of view, is to specify the zero normal flow boundary condition on the solid boundaries. This problem is known as the *Newman Problem* and in order to evaluate the velocity field the potential is differentiated

$$\nabla\phi = -\frac{1}{4\pi}\int_{S_B}\sigma\nabla\left(\frac{1}{r}\right)dS + \frac{1}{4\pi}\int_{S_B+S_W}\mu\nabla\left[\frac{\partial}{\partial n}\left(\frac{1}{r}\right)\right]dS + \nabla\phi_\infty \qquad \text{A. 23}$$

Now the different basic solutions will be presented.

A.2.1 Point Source

One of the basics solutions is the source/sink. The potential of such a point source element, placed at the origin of a spherical coordinate system, is $\phi = -\frac{\sigma}{4\pi r}$. And the velocity due to this element will result in a velocity field with radial component only, $\vec{q} = \nabla\phi = \frac{\sigma}{4\pi}\frac{\vec{r}}{r^3}$.

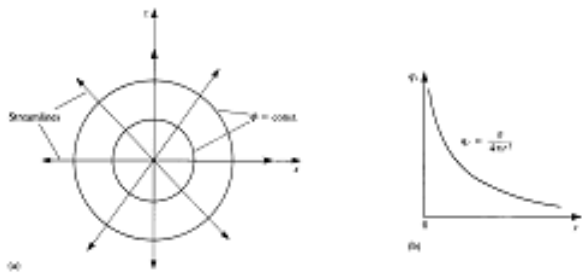

Figure A. 4. (a) Streamlines and equipotential lines due to source element at the origin, as viewed in the x-z plane (b) Radial variation of the radial velocity component induced by a point source

A.2.2 Point Doublet

The second basic solution is the doublet.

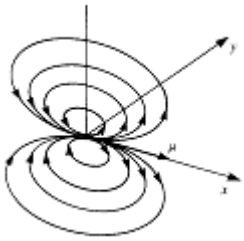

Figure A. 5. Sketch of the streamlines due to a doublet pointing in the x direction

$$\phi = \frac{\mu}{4\pi}\vec{n}\cdot\nabla\left(\frac{1}{r}\right) \quad \text{A. 24}$$

$$\phi(x,y,z) = \frac{\mu}{4\pi}\vec{n}\cdot\nabla\left(\frac{1}{|\vec{r}-\vec{r}_0|}\right) = \frac{\mu}{4\pi}\frac{\partial}{\partial n}\left(\frac{1}{|\vec{r}-\vec{r}_0|}\right) = \frac{\mu}{4\pi}\begin{pmatrix}\frac{\partial}{\partial x}\\ \frac{\partial}{\partial y}\\ \frac{\partial}{\partial z}\end{pmatrix}\left(\frac{1}{|\vec{r}-\vec{r}_0|}\right) \quad \text{A. 25}$$

The differentiation will be done depending of the direction of the doublet.

A.2.3 Vortex

To illustrate a flow field frequently called a two-dimensional vortex consider a two-dimensional rigid cylinder of radius R rotating in a viscous fluid at a constant angular velocity of ω_z .

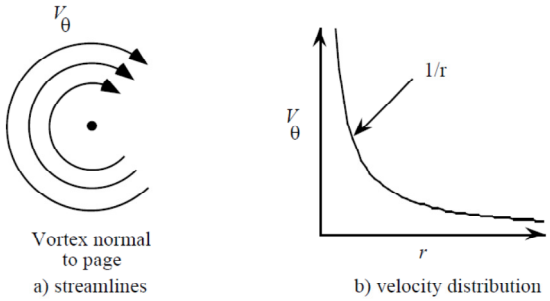

Figure A. 6. Two dimensional flow field around a cylinder core rotating as a rigid body

This motion results in a flow with circular streamlines and therefore the radial velocity component is zero. Consequently the continuity equation in the $r-\theta$ plane becomes

$$\frac{\partial V_\theta}{\partial \theta} = 0 \rightarrow \ Integrating \rightarrow V_\theta = V_\theta(r) \quad \text{A. 26}$$

The Navier-Stokes equation in the r direction, after neglecting the body force terms, becomes

$$-\rho \frac{V_\theta^2}{r} = -\frac{\partial p}{\partial r} \quad \text{A. 27}$$

The velocity V_θ is a function of r only, and because of the radial symmetry of the problem, the pressure must be either a function of r or a constant. Therefore, its derivative will not appear in the momentum equation in the θ direction.

$$\begin{aligned} 0 = \mu\left(\frac{\partial^2 V_\theta}{\partial r^2} + \frac{1}{r}\frac{\partial V_\theta}{\partial r} - \frac{V_\theta}{r^2}\right) \rightarrow 0 = \mu\left(\frac{\partial^2 V_\theta}{\partial r^2} + \frac{d}{dr}\left(\frac{V_\theta}{r}\right)\right) \\ \rightarrow Integration\ with\ respect\ r\text{:}\ \frac{dV_\theta}{dr} + \frac{V_\theta}{r} = C_1 \rightarrow \frac{1}{r}\frac{d}{dr}(rV_\theta) \\ = C_1 \rightarrow After\ an\ adition\ integration\text{:}\ V_\theta = \frac{C_1}{2}r + \frac{C_2}{r} \end{aligned} \quad \text{A. 28}$$

And the boundary conditions are

$$At\ r = R \rightarrow\ V_\theta = -R\omega_z \qquad and\ at\ r = \infty\ \rightarrow\ V_\theta = 0 \quad \text{A. 29}$$

The velocity becomes $V_\theta = -\frac{R^2\omega_y}{r}$.

The circulation has the same sign as the vorticity, and is therefore positive in the clockwise direction. The circulation around the circle of radius r concentric with the cylinder is:

$$\Gamma = \oint_C \vec{V} \cdot d\vec{l} = \int_{2\pi}^{0} V_\theta r d\theta = 2\omega_y \pi R^2 \quad \text{A. 30}$$

The circulation is constant and the tangential velocity can be rewritten us.

$$V_\theta = -\frac{\Gamma}{2\pi r} \quad \text{A. 31}$$

The velocity distribution is shown in Fig. 1.7b and is called vortex flow. If $r \rightarrow 0$ then the velocity becomes very large near the solid core.

Integrating the velocity in a clockwise direction, and recalling that $V_r = 0$.

$$\oint \vec{V} \cdot d\vec{l} = 0 \cdot \Delta r + \frac{\Gamma}{2\pi(r+\Delta r)}(r+\Delta r)\Delta\theta - 0 \cdot \Delta r - \frac{\Gamma}{2\pi r} r\Delta\theta = 0 \qquad \text{A. 32}$$

This indicates that this vortex flow is irrotational everywhere, excluding the rotating cylinder at the boundary of which all the vorticity is generated. When the core size approaches zero $(R \to 0)$ then this flow is called an irrotational vortex (excluding the core point, where the velocity approaches infinity).

A.3 The Biot-Savart Law

We have an incompressible fluid for which the continuity equation is $\nabla\vec{V} = 0$, and were the vorticity $\vec{\Omega}$ can exist, and the problem is to determine the velocity field as a result of a known vorticity distribution. We may express the velocity field as the curl of a vector field $\vec{B}$, $\vec{V} = \nabla \times \vec{B}$. Since the curl of a gradient vector is zero , $\vec{B}$ is indeterminate to within the gradient of a scalar function of position and time, and $\vec{B}$ can be selected such that $\nabla \cdot \vec{B} = 0$.

The vorticity then becomes

$$\vec{\Omega} = \boldsymbol{\nabla} \times \vec{V} = \boldsymbol{\nabla} \times \left(\boldsymbol{\nabla} \times \vec{B}\right) = \boldsymbol{\nabla}\left(\boldsymbol{\nabla} \cdot \vec{B}\right) - \nabla^{\boldsymbol{2}}\vec{B} = -\nabla^{\boldsymbol{2}}\vec{B} \qquad \text{A. 33}$$

$\vec{B}$ has been chosen with gradient equal to zero, so the equation of the vorticity will become to the Poisson equation for the potential vector $\vec{B}$.

$$\vec{\Omega} = -\nabla^2\vec{B} \qquad \text{A. 34}$$

The solution of this equation using Green's theorem is

$$\vec{B} = \frac{1}{4\pi}\int_{\boldsymbol{V}} \frac{\vec{\Omega}}{|\overrightarrow{\boldsymbol{r_0}} - \vec{\boldsymbol{r}}_{\boldsymbol{1}}|} dV \qquad \text{A. 35}$$

$\vec{B}$ is evaluated at point P (which is a distance $\vec{r}_0$from the origin) and is a result of integrating the vorticity $\vec{\Omega}$ (at point $\vec{r}_1$) within the volume V. The velocity fiel is then the curl of $\vec{B}$.

$$\vec{B} = \frac{1}{4\pi}\int_V \nabla \times \frac{\vec{\Omega}}{|\vec{r}_0 - \vec{r}_1|} dV \qquad \text{A. 36}$$

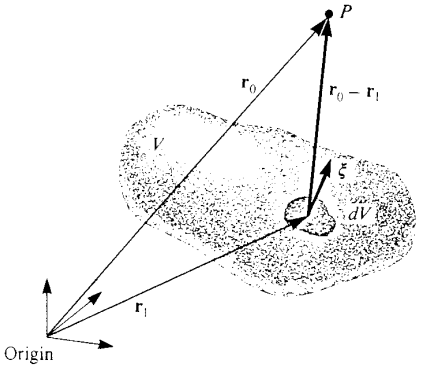

Figure A. 7. Velocity at point P due to a vortex distribution

Let us consider an infinitesimal piece of the vorticity filament $\vec{\Omega}$.

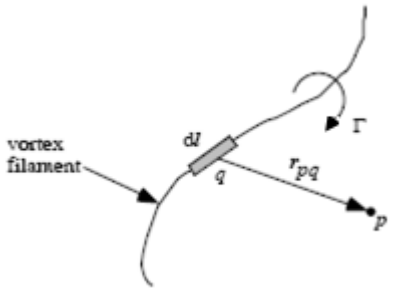

Figure A. 8. The velocity at point P induced by a vortex segment

The cross-sectional area is selected such that it is normal to $\vec{\Omega}$, and the direction $d\vec{l}$ on the filament is $d\vec{l} = \frac{\vec{\Omega}}{\Omega}$, $\vec{r}_{pq} = \vec{r}_0 - \vec{r}_1$, $\vec{r}_0$ is the position vector of the point P and $\vec{r}_1$ is the position vector of the filament $d\vec{l}$. Also the circulation is $\Gamma = \Omega dS$ and $dV = dS \cdot dl$ so that

$$\nabla \times \frac{\vec{\Omega}}{|\vec{r}_0 - \vec{r}_1|} dV = \nabla \times \Gamma \frac{d\vec{l}}{|\vec{r}_0 - \vec{r}_1|} = \Gamma \frac{d\vec{l} \times (\vec{r}_0 - \vec{r}_1)}{|\vec{r}_0 - \vec{r}_1|} \qquad \text{A. 37}$$

And the velocity induced by a vortex filament $d\vec{l}$ of with circulation Γ will result.

$$\vec{V} = \frac{1}{4\pi}\int_V \nabla \times \frac{\vec{\Omega}}{|\vec{r}_0 - \vec{r}_1|} dV = \frac{\Gamma}{4\pi}\int \frac{d\vec{l} \times (\vec{r}_0 - \vec{r}_1)}{|\vec{r}_0 - \vec{r}_1|^3} = \frac{1}{4\pi}\int_V \frac{\vec{\Omega} \times (\vec{r}_0 - \vec{r}_1)}{|\vec{r}_0 - \vec{r}_1|^3} dV \quad \text{A. 38}$$

Have been explained that one of the computational methods commonly used to predict the flow over sails is the vortex lattice method. In these methods, sails are discretized in quadrilateral elements with vorticity, so each element is a ring of vorticity segments. It is known the velocity induced by a vortex filament $d\vec{l}$ and it is easy to deduce the velocity induced by a straight vortex segment, which is necessary to evaluate the velocity induced by a ring of vorticity elements.

It is clear that a vortex line cannot start or end in a fluid, and the following discussion is aimed at developing the contribution of a segment that is section of a continuous vortex line. The vortex segment is placed at an arbitrary orientation in the (x, y, z) frame with constant circulation Γ. The velocity induced by this vortex segment will have tangential components only. The distance $|\vec{r}_0 - \vec{r}_1|$ between the vortex segment and the point P is $\vec{r}$.

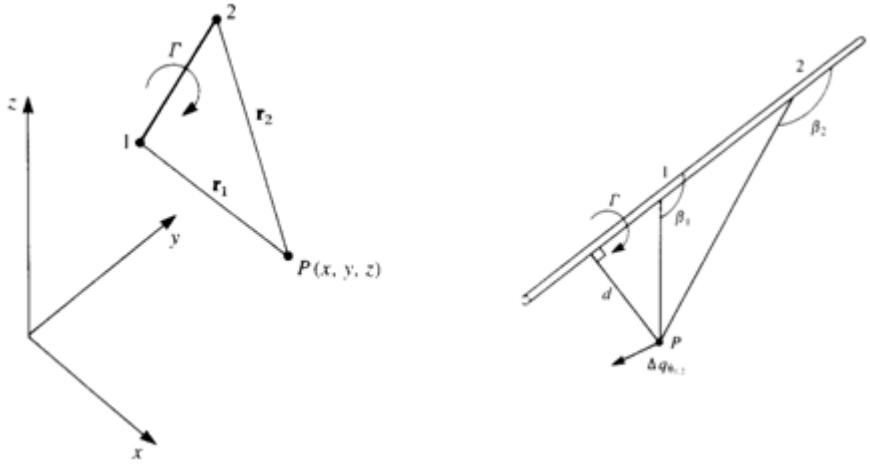

Figure A. 9. Velocity induced by a straight vortex segment

According to the Biot-Savart law the velocity induced by a segment $d\vec{l}$ is

$$\Delta\vec{V} = \frac{\Gamma}{4\pi}\frac{d\vec{l} \times (\vec{r}_0 - \vec{r}_1)}{|\vec{r}_0 - \vec{r}_1|^3} \quad \text{A. 39}$$

It is know that the induced velocity will have tangent components only, so the velocity can be rewritten in scalar form $\Delta V_\theta = \frac{\Gamma}{4\pi}\frac{sin\beta}{r^2}dl$.

$$d = r\,sin\beta \qquad \tan(\pi - \beta) = \frac{d}{l} \rightarrow l = \frac{-d}{\tan\beta} \rightarrow dl = \frac{d}{\sin^2\beta}d\beta \quad \text{A. 40}$$

Substituting in the equation of the velocity and integrating over a section $(1 \rightarrow 2)$ of the straight vortex segment:

$$(V_\theta)_{1,2} = \frac{\Gamma}{4\pi d}\int_{\beta_1}^{\beta_2} sin\beta\ d\beta = \frac{\Gamma}{4\pi}(cos\beta_1 - cos\beta_2) \qquad \text{A. 41}$$

For the general three dimensional case the two edges of the vortex segment will be located by $\vec{r}_1$ and $\vec{r}_2$, and the vector connecting the edges is $\vec{r}_0 = \vec{r}_1 - \vec{r}_2$.

$$d = \frac{|\overrightarrow{r_1} \times \overrightarrow{r_2}|}{|\overrightarrow{r_0}|}$$

$$cos\beta_1 = \frac{\overrightarrow{r_0} \cdot \overrightarrow{r_1}}{|\overrightarrow{r_0}| \cdot |\overrightarrow{r_1}|}$$

$$cos\beta_2 = \frac{\overrightarrow{r_0} \cdot \overrightarrow{r_2}}{|\overrightarrow{r_0}| \cdot |\overrightarrow{r_2}|}$$

The direction of the velocity $\vec{V}_{1,2}$ is normal to the plane created by the point P and the vortex edges 1,2 and is given by $\frac{\overrightarrow{r_1}\times\overrightarrow{r_2}}{|\overrightarrow{r_1}\times\overrightarrow{r_2}|}$.

So, we get an induced velocity of

$$\vec{V}_{1,2} = \frac{\Gamma}{4\pi}\frac{\overrightarrow{r_1} \times \overrightarrow{r_2}}{|\overrightarrow{r_1} \times \overrightarrow{r_2}|^2}\ \overrightarrow{r_0} \cdot \left(\frac{\overrightarrow{r_1}}{r_1} - \frac{\overrightarrow{r_2}}{r_2}\right) \qquad \text{A. 42}$$

Appendix B: *Sailing*

This software has been designed to analyze the sails and rigging performance of a boat. So, the first necessary step is the geometry to analyze. The initial sail geometry must be, the geometry designed by the designer, and so on for the rigging. A graphic interface (GUI) based on GID[24] has been developed to create or import the structure (sail and rigging) and to define the different elements of the structure.

B.1 Basic structure

The geometry can be created with GID, or can be imported. In order to carry out the requests of the program, some considerations must be fulfilled during the definition of the geometry.

- The base of the mast must be collocated in the coordinate origin.
- The axis of symmetry of the yacht must be parallel to the $\boldsymbol{x}$ axis, with the jib in the negative part and the main in the positive part.
- The initial sail geometry, the designed geometry, must be bended to starboard, is it, to the positive part of the $\boldsymbol{y}$ axis.
- It is necessary make sure to point normals, of the surfaces, toward the positive direction of the $\boldsymbol{y}$ axis.

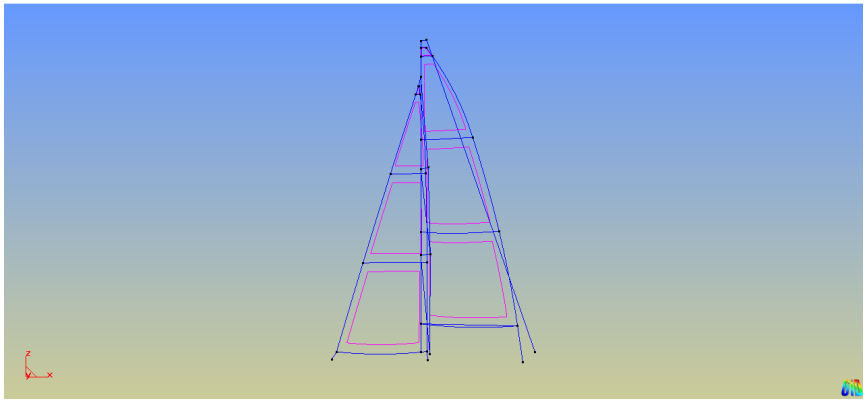

Figure B. 1. Placing of the geometry

B.2 Structural constrains

B.2.1 The base of the mast

The base of the mast is embedding in the desk of the sail boat. So the displacements and the rotations of this point must be fixed.

[24] GiD is a universal, adaptive and user-friendly pre and postprocessor for numerical simulations in science and engineering. It has been designed to cover all the common needs in the numerical simulations field from pre to postrocessing: geometrical modelling, effective definition of analysis data, mesh generation, transfer data to analysis software and visualisation of results. GID is developed at CIMNE (International Centre on Numerical Methods applied at Engineering).

Into the option DATA of the main menu, select the option CONDITIONS. Into the submenu, select the option STRUCTURAL and select the option of the POINT. Into the down menu select DISPLACEMENTS.

DATA/CONDITIONS/STRUCTURAL/POINT/DISPLACEMENTS

and

DATA/CONDITIONS/STRUCTURAL/POIT/ROTATION

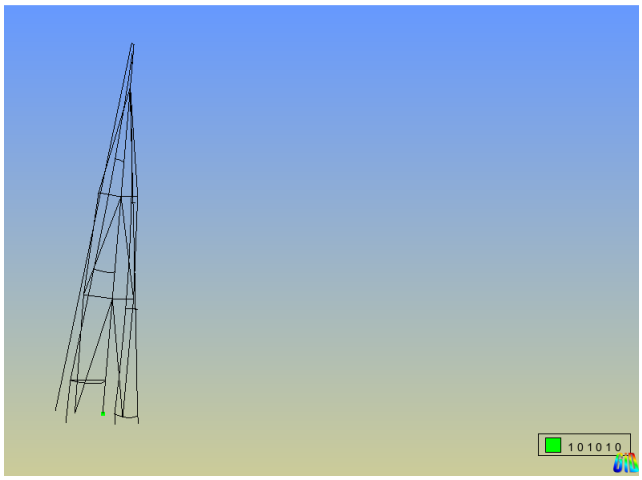

Figure B. 2. Constrains in the base of the mast

B.2.2 Stays, sheets and shroud.

Stays, sheets and shrouds are fixed on the desk of the sail boat, so the displacements of these nodes must be fixed to zero.

DATA/CONDITIONS/STRUCTURAL/POINT/DISPLACEMENTS

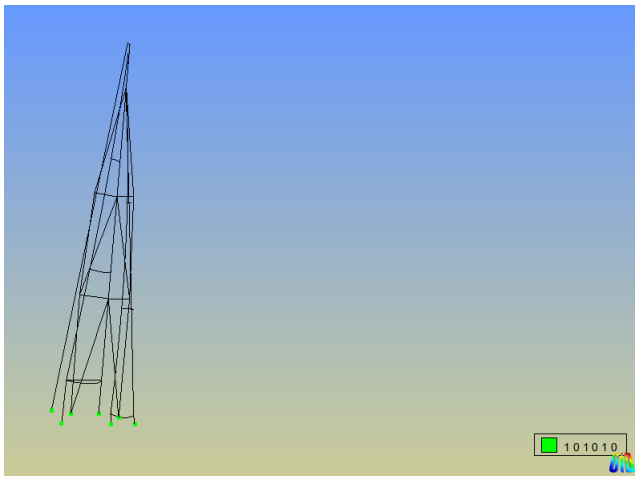

Figure B. 3. Constrains in stays, clews and battens.

B.2.3 Joint mast-boom

The boom can rotate around the mast. The mast is located in the z axis, so it is necessary to release the degrees of freedom of the rotation around the z axis, in this node.

DATA/CONDITIONS/STRUCTURAL/POINT/FREE ROTATION

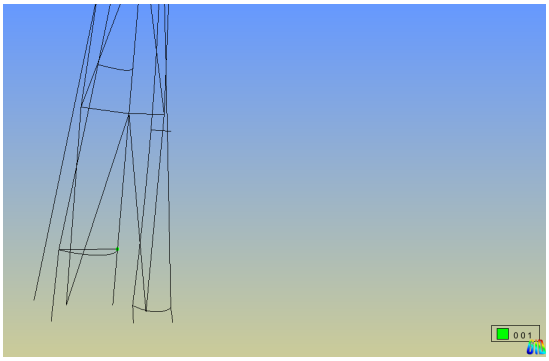

Figure B. 4. Joint mast-boom

B.2.4 Stress of the cables

An important point, is to indicate the stress in the different cables that make up the rigging of the sailboat.

The stress can be indicated of three different ways.

1- It is possible to indicate the stress (N/m^2) in the cables. (State 1)
2- It is possible to indicate the force (N) in the cables. (State 3)
3- It is possible to indicate the cut in a cable. This way is thought to be used only in the sheets, and these must be meshed with an element. (State 2)
4- If the cable is not stressed. (State 0)

DATA/CONDITIONS/STRUCTURAL/LINE/STATE

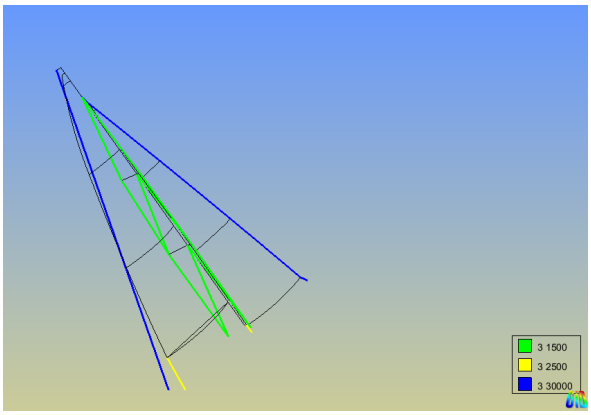

Figure B. 5. Stress in the cables

In the next chapter will be explained the way to adjust this parameters to real values, in real time.

B.3 Constraints for the FS

B.3.1 Trailing Edges

DATA/CONDITIONS/CFD/LINE/TRAILING EDGES

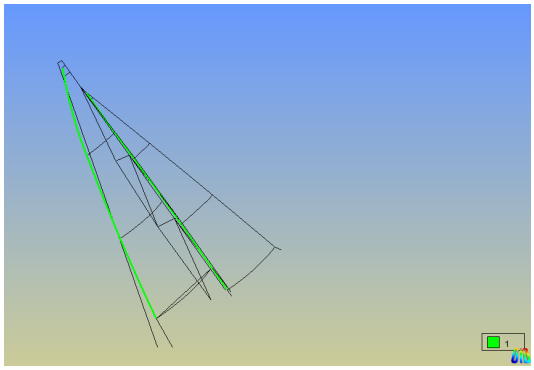

Figure B. 6. Trailing edges

B.3.2 Leading Edge

DATA/CONDITIONS/CFD/LINE/LEADING EDGES

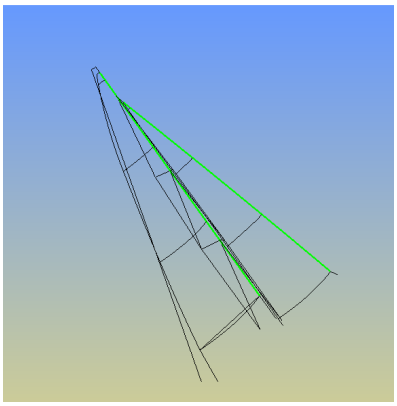

Figure B. 7. Leading Edges

B.3.3 Thin Body

The sails are consider as surface, so it is necessary to indicate that it is a thin body.

DATA/CONDITIONS/CFD/SURFACE/BODY SURFACE

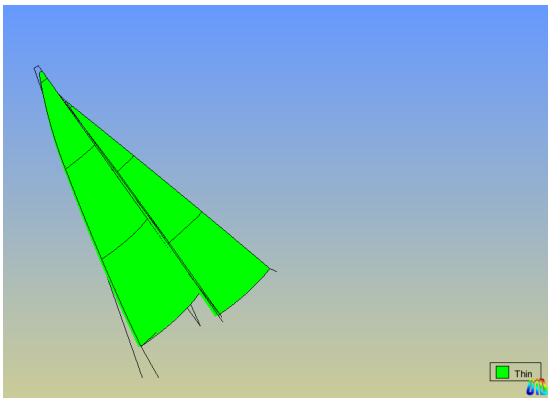

Figure B. 8. Thin Body

B.3.4 Aero Surface

It is necessary to indicate that sails are aerosurfaces, and what is the foresail and what is the mainsail.

DATA/CONDITIONS/CFD/SURFACES/AERO SURFACE

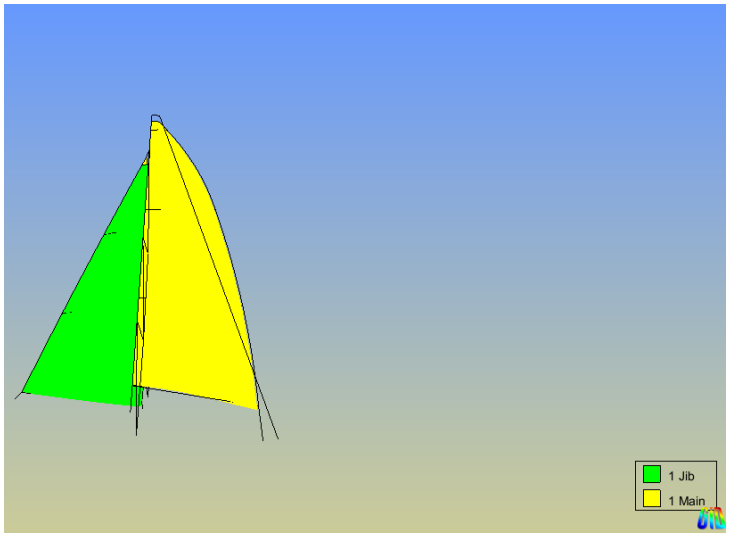

Figure B. 9. Aerosurface (main and jib)

B.4 Properties of the materials

The structure consists on a joint of different elements, sails, mast, boom, shrouds, spreaders, main sheet and foresail sheet. All these elements have different mechanical properties and it is necessary to consider these properties for the structural analysis.

B.4.1 Beams

The data of the beams must be in local axis. The local axis are always defined with the x axis longitudinal direction of the beam. y and z axis are defined in the

tangential directions to the section of the beam. It is possible to visualize local axis, to indicate correctly the inertia moments I_z and I_y.

DATA/CONDITIONS/BEAM SECTION

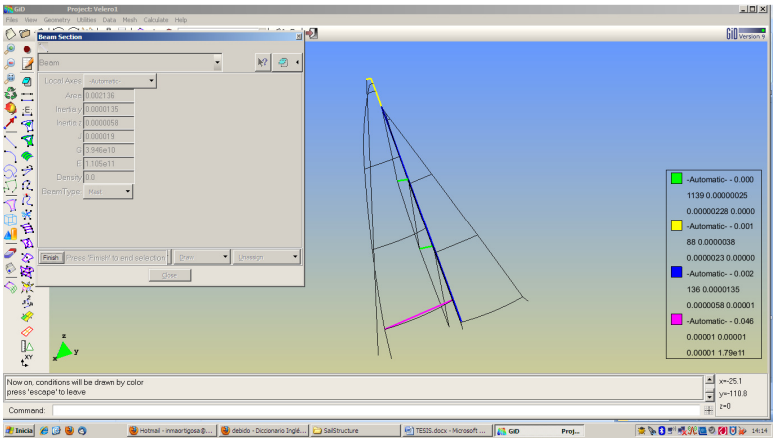

Figure B. 10. Properties of the Beams

B.4.2 Cables

DATA/CONDITIONS/CABLE SECTION

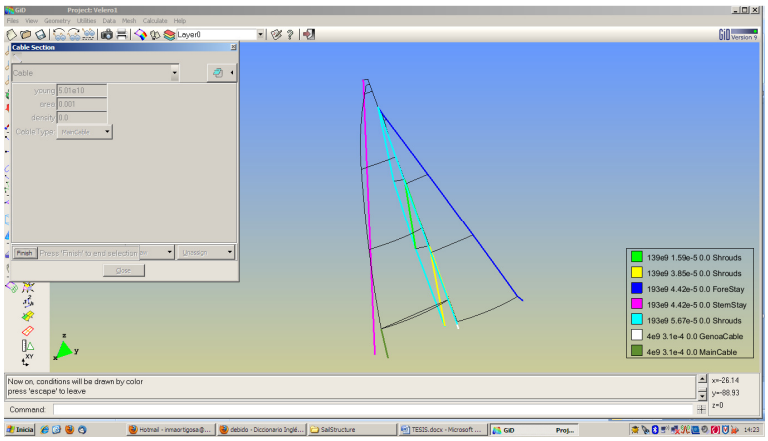

Figure B. 11. Properties of the cables

B.4.3 Membranes

DATA/CONDITIONS/MEMBRANE

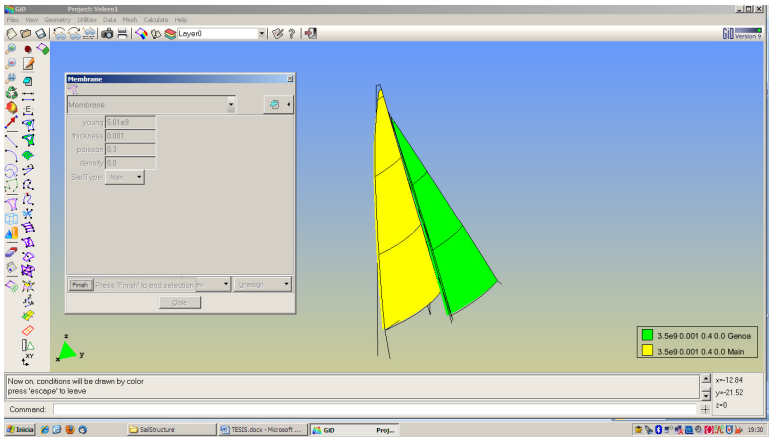

Figure B. 12. Properties of the sails

B.5 Structural, Potential or Couple Problem

Has been explained that the software has a Finite Element Analysis for the sail and rigging structure and a Computational Fluid Dynamic model for the aerodynamic field, these are combined and iteratively solved to compute the actual flying shape of the sail. So it is possible to do three types of calculations:

- It is possible to calculate the mechanical response of a structure subjected to some actions, using the finite element analysis. (Structural Problem)
- It is possible to calculate the aerodynamic field around a thin airfoil, using the computational fluid dynamic model. (Potential Problem)
- It is possible to calculate the response of a structure to the action of the airflow around this structure. In this case, the FEA and the FS model are combined and iteratively solved. (Coupled Problem)

B.5.1 Structural Problem

The structural part of the method is based on Finite Element representation of the sail and the rigging. Minimization of the total potential energy function using a quasi Newton type method is carried out to calculate the displacements of the structure under aerodynamic loads. Stable equilibrium configuration of the structure is calculated from the minimum condition of the total potential energy.

DATA/PROBLEM DATA/GENERAL DATA

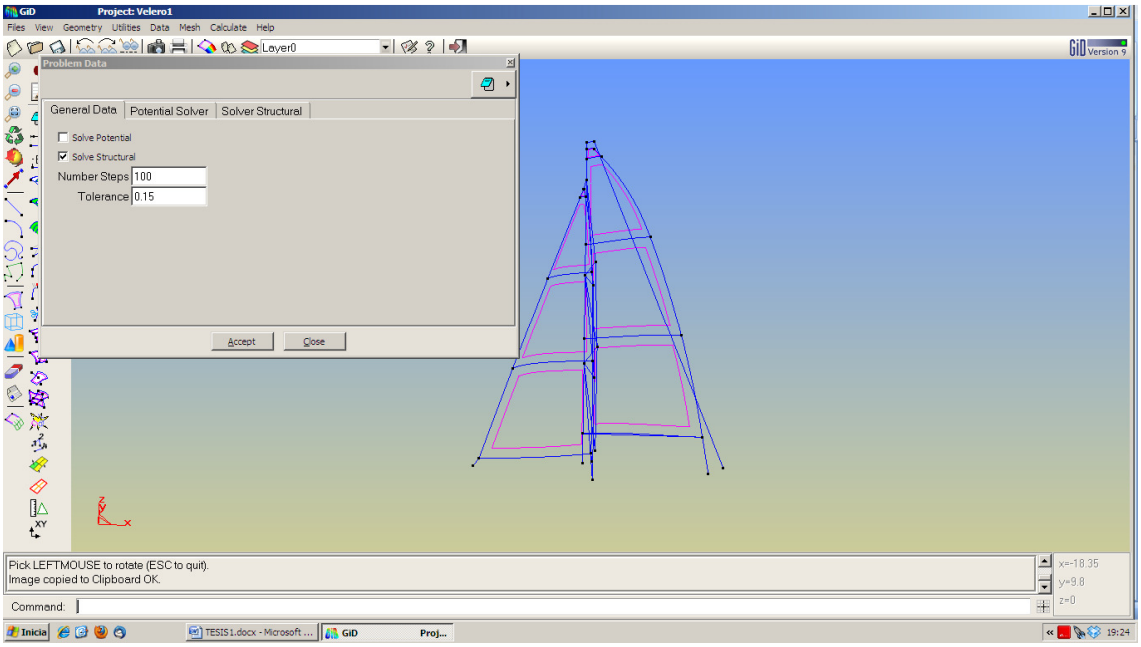

Figure B. 13. Structural problem selection

It is necessary to select the option of the structural problem in the software when it is desired to execute the structural calculation.

The number of steps is a necessary definition when the problem is a coupled problem, Structural Problem and Potential Problem.

The unconstrained minimization of the smooth nonlinear real-valued function, is solved by a Quasi Newton and line search with cubic interpolation. Descriptions of these methods can be found in the next references,(Nocedal, 1999) and (Luenberger, 1984).

DATA/PROBLEM DATA/SOLVER STRUCTURAL

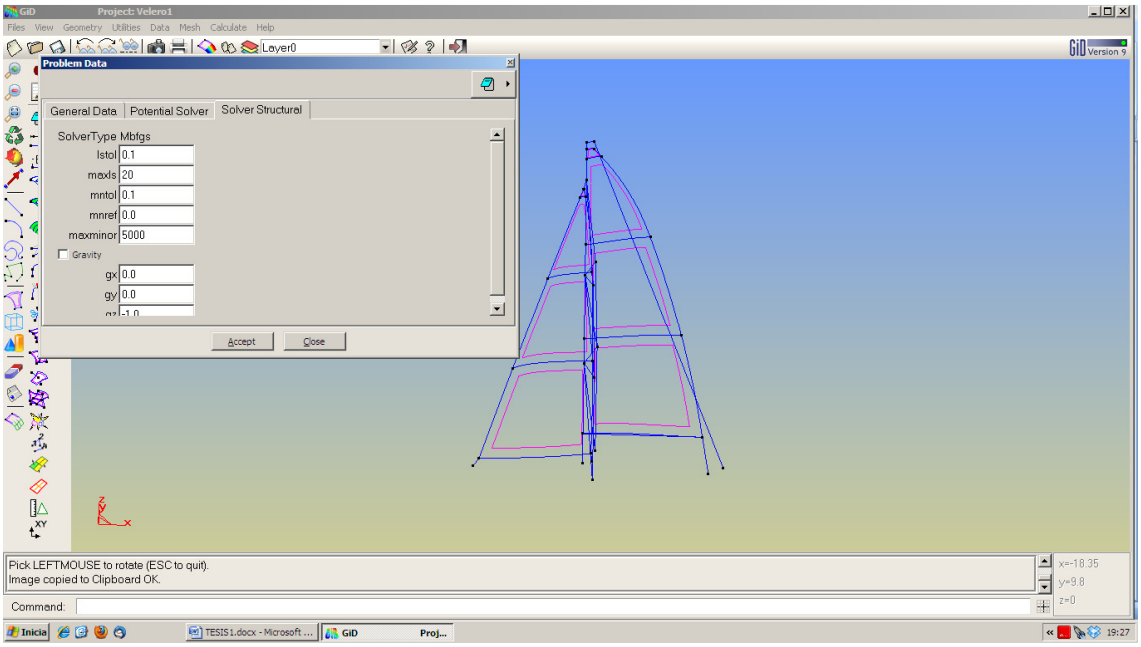

Figure B. 14. Structural parameters

Parameters:

- Lstol: Controls the accuracy of the search. It must lie in the range $0 \leq lstol < 1.0$. Decreasing this value tends to increase the accuracy of the search. It is usually 0.1.
- Maxls: The maximum number of cubic interpolations allowed. It must be greater than one. It is usually 20.
- Mntol: The iterative procedure has stopping criteria that the residuum has decreased sufficiently. The residuum is $R = \sum_{elements} \nabla\phi\,(x) - f$, and it is necessary to decrease it until $mntol * mnref$. If the problem is a structural problem alone, the usual value of this parameter is 0.001, but if the problem is a coupled problem, structural and potential, the usual value is 0.1.
- Mnref: Must be a positive value. If it is specified like 0.0, it is replaced by the infinite norm of the gradient, evaluated at the starting point.
- Maxminor: The maximum number of iterations allowed. It must be greater than zero. It is usually 10*N, where N is the number degrees of freedom. A good approximation will be 10*3*n, where n is the number of nodes.

B.5.2 Potential Problem

A computational fluid dynamic based in boundary elements, the panel method, is used to solve the flow around the sail set.

Solutions of this calculus are lifting coefficient, drag coefficient and the pressure flow forces distributed on the vertices of the surface mesh of the sail.

The first step is to select the option of potential problem in the software. The number of steps is a necessary definition when the problem is a coupled problem, Structural Problem and Potential Problem.

DATA/PROBLEM DATA/GENERAL DATA

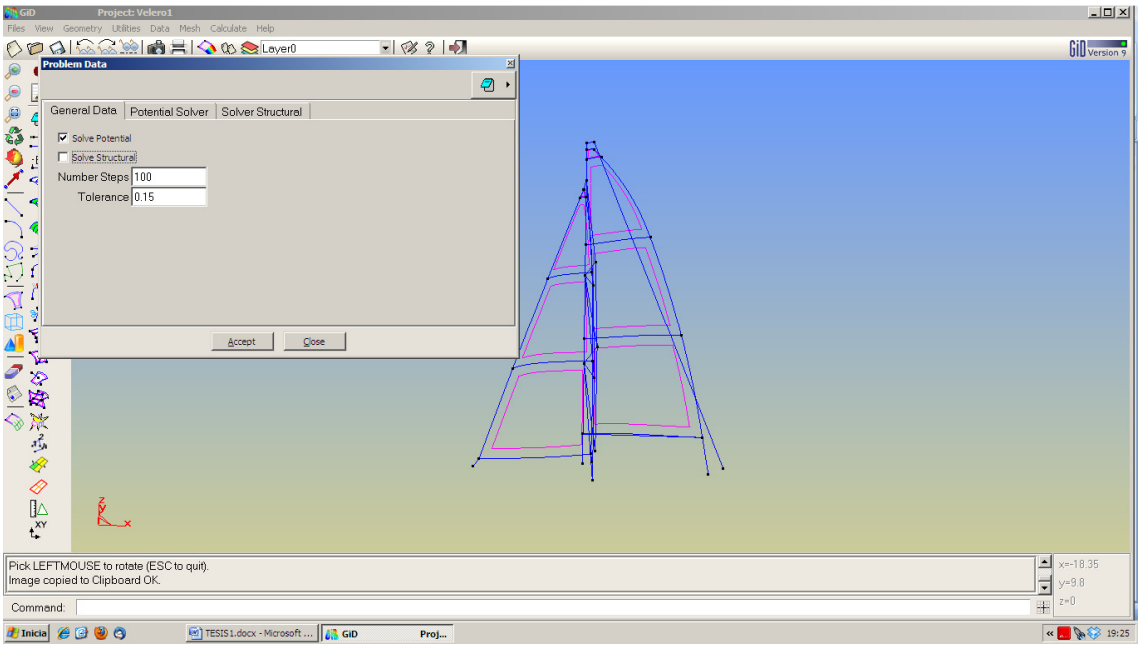

Figure B. 15. Potential Problem Selection

To solve the flow around the sails it is necessary to indicate the apparent wind speed. The medium chord of the sails is necessary to generate the wake.

It is possible to select a Far Field approximation. Considering numerical efficiency, the computation of the influence coefficients is elaborated. Many methods divide such calculation treats the element as a point singularity, and not as a surface distribution. Typically, the near field is assumed if the distance to a point is less than 2.5-5 times the largest diagonal of the panel.

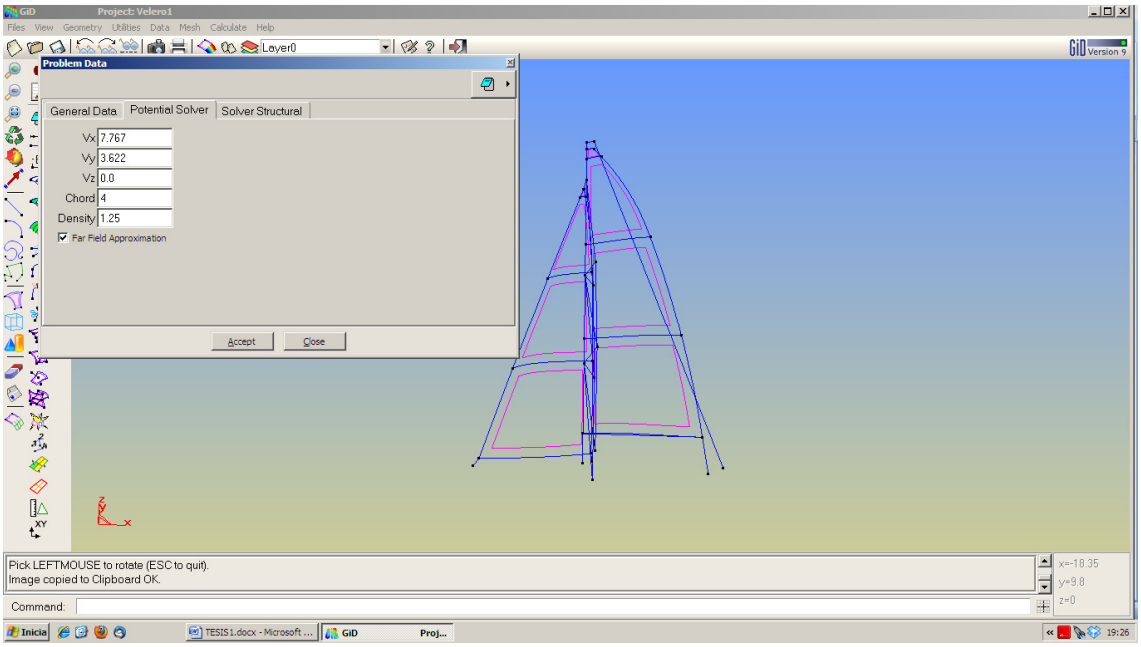

Figure B. 16. Potential Problem Parameters

B.5.3 Coupled Problem

A coupled problem involves a fluid/structure analysis, so the Structural Problem and the Potential Problem must be activated in the software.

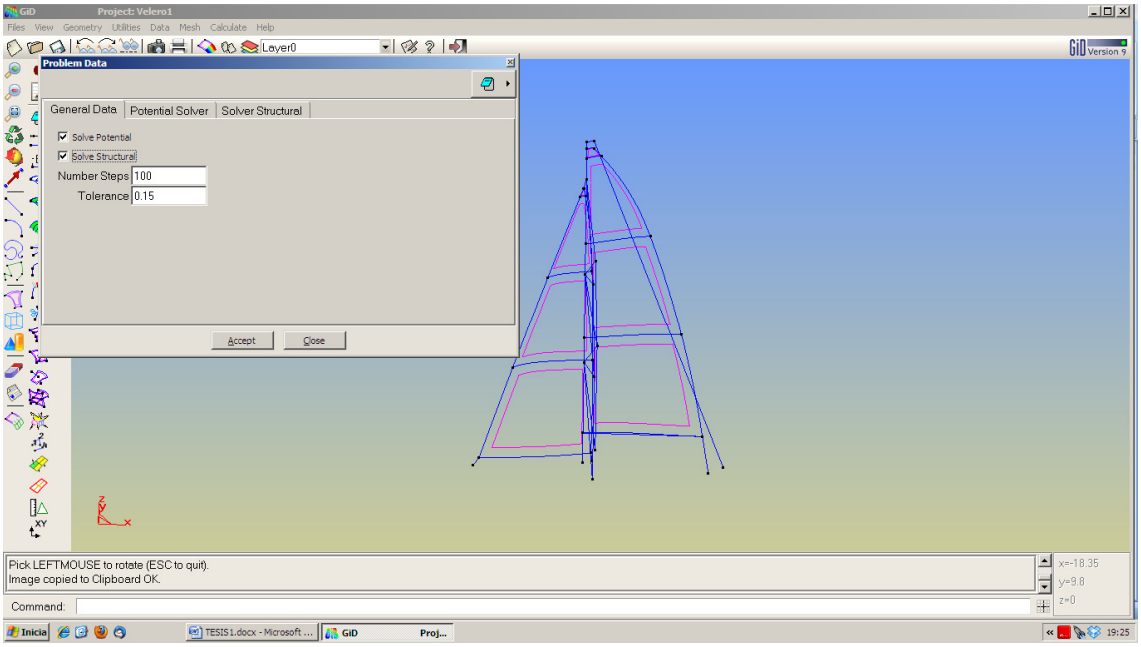

Figure B. 17. Potential Problem and Structural Problem activation

In this type of problems, the iterative procedure between the two methods starts with the calculation of the pressures forces that the flow applies on the structure. The structural problem uses these forces to calculate the displacements of the nodes and the new aerodynamic forces are computed. This iterative procedure is repeated

until the stopping criteria are reached. The parameter *Number of Steps* indicates the maximum number of iterations between the potential and the structural calculation. And the parameter tolerance refers to the stopping criteria for the iteration problem.

$$\forall\ node\ \frac{\left|\vec{f}_{k+1} - \vec{f}_k\right|}{\vec{f}_k} < tol$$

B.6 Mesh generation

Once the problem has been defined, it is necessary to generate the mesh. The elements to mesh are the lines and the surfaces. The mesh generated at the surface must be a structured mesh with quadrilateral elements.

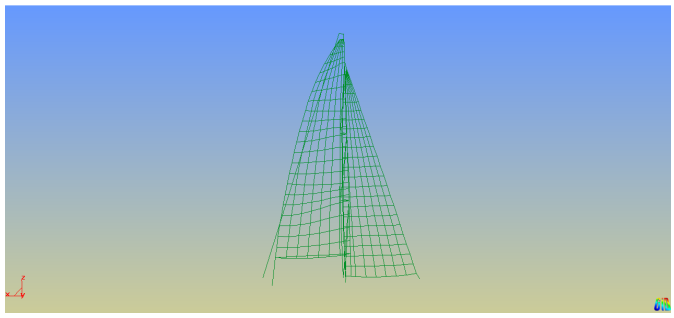

Figure B. 18. Mesh

The potential calculation needs these quadrilateral elements on sails surfaces, but the structural calculation on the sails uses triangular elements. So, the program generates internally two meshes, one for the potential calculation and another for the structural calculation. The triangular elements are generated by dividing the quadrilateral elements in two triangular elements.

Appendix C: Wireless Technology

C.1 V-link Wireless Voltage Node

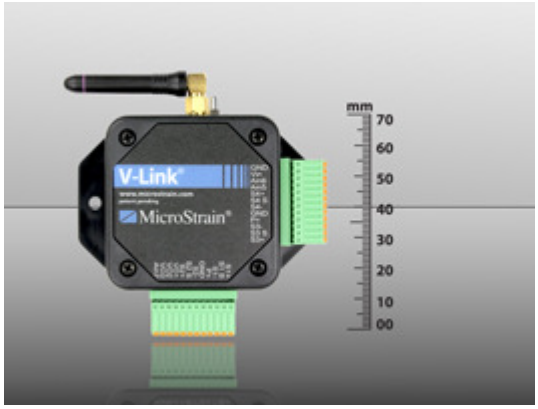

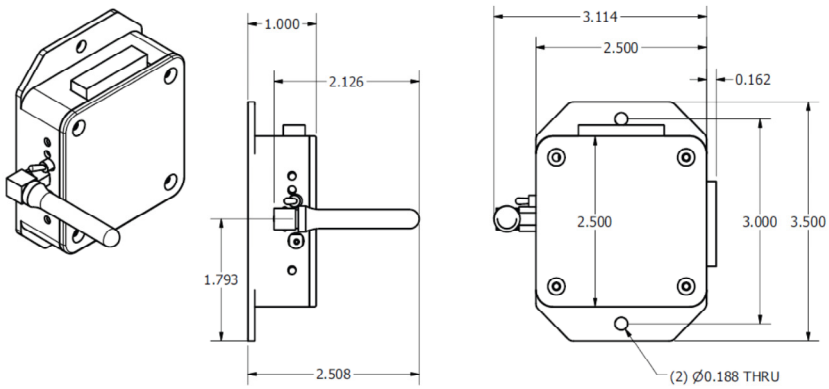

Figure C. 1. . V-Link dimensions

The V-link is a wireless voltage node and is a specialized member of MicroStrain's Agile-Link wireless data acquisition system. The Agile-Link system comprises 3 main components: 1) wireless sensor nodes which acquire and transmit strain, 2) base stations which receive and pass the data to a host, and 3) software which operates the system.

The V-link provides 7 external measurement channels, being 4 differential input channels (strain channels) primarily designed to support strain gauges of 350 ohm resistance or greater, and 3 single ended input channels (analog channels) designed to support 0-3 volt sensors. The combination of the 7 measurement channels supports a wide range of Wheatstone bridge type and sensors including strain gauges.

The V-link employs a 12 bits A/D converter to digitize the voltage on the differential input, single ended input and temperature channels. The digital data is passed to the

onboard microprocessor, processed with the embedded algorithm, and in turn either passed to its radio for immediate transmission.

Host computer software displays the data, provides analysis tools, records the data to file and allows the user to configure and actuate the system.

The V-Link may be deployed up to 70 meters (line-of-sight) from its base station, and 100 meters or more with added antenna options.

The base station selected to our work was the USB base station.

Figure C. 2. USB base station

The transceiver base station attaches to your host computer and provides communication between the software and the node, V-link.

The V.link has four differential input channels. These channels are designed to accommodate strain gauges with 350 ohm resistance or greater. The V´link by default is configured to support a full Wheatstone bridge installation. The V-Link can also be ordered from the factory configured to support half and quarter bridge installations.

The V-link powers the differential input channel with +3 volts DC at up to 50mA for bridge excitation. Programmable gain is user-adjustable and allows the bridge circuit to be amplified to suit the characteristics of the particular strain gauges in use. Programmable offset is also user-adjustable and allows for the ‘zeroing’ of strain gauge output. Strain gauge bridges can have significant offset due to a number of factors including initial holmic error in the gauge itself, installation of the gauge on a non-flat surface, initial offset error in the electronics, and small errors in the bridge completion resistors.

The 3 volt signal is digitized by the V-link’s 12-bit A/D converter, creating a 0 to 4096 ‘bit’ digital range. The Agile-Link system operates digitally by resolving all sensor voltages to ‘bits’, transmitting the bits by radio to the base station, carrying the bits into host software, and finally returning these bits to volts at the software level. Agile-Link software further provides an on-board function which allows engineering units to be output and displayed directly from the software.

A full bridge was used and the connection was

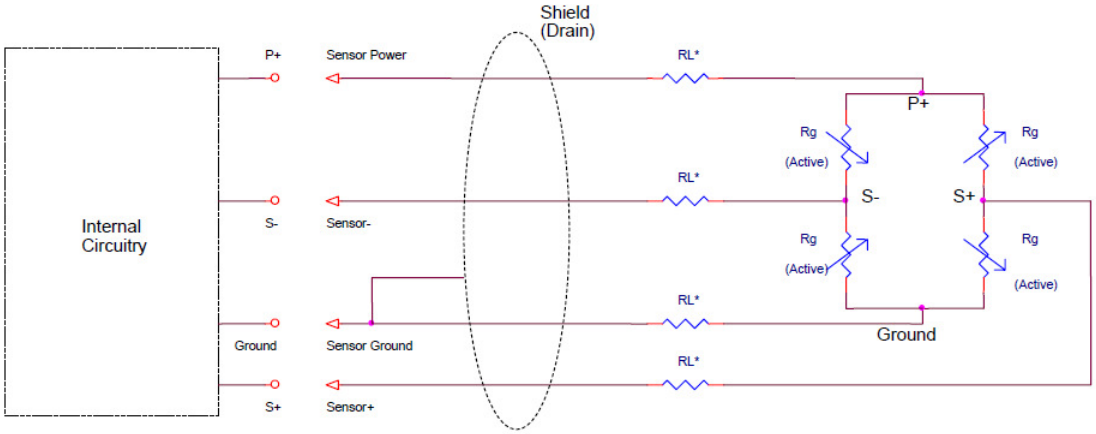

Figure C. 3. Full Bridge

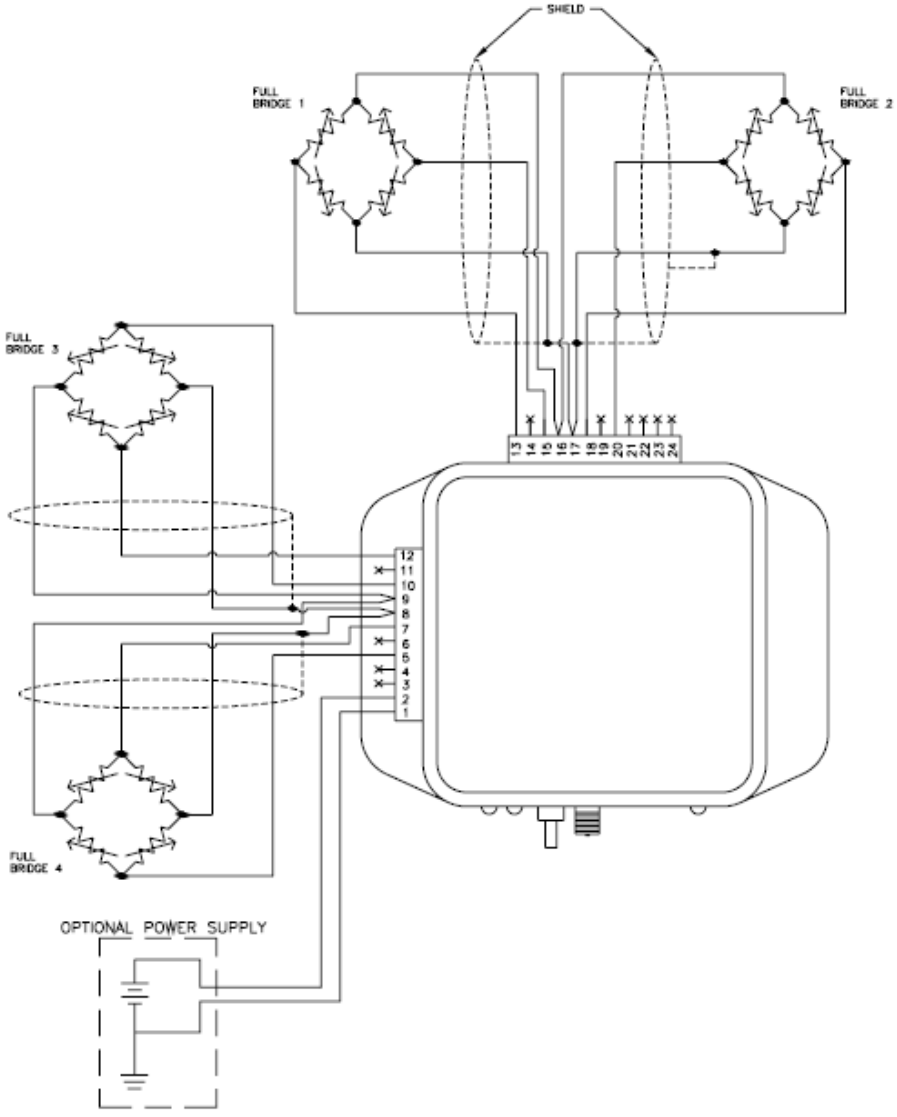

Figure C. 4. Full bridge connection

The V-Link should be fully charged before each use. Charging may take up to several hours depending on battery depletion. An example battery life calculation will be: streaming with one 350 ohm strain gauge consumes $\sim 33mA$. If the V-Link battery capacity is $600\ mAh$, the device will stream for $\sim 18\ hours$ before recharging is required. If we consider the use of a full bridge that consists of four strain gauges the battery's life will be less than 18 hours.

C.2 Waspmote

Waspmote is a sensor device specially oriented to developers. It works with different protocols (ZidBee, Bluetooth, GPRS) and frequencies being capable of getting links up to 12km. It counts with an hibernate mode of 0.7µA which allows to save battery when it is not transmitting. More than 50 sensors already available and a complete open source IDE (API libraries plus compiler) made really easy to start working with the platform.

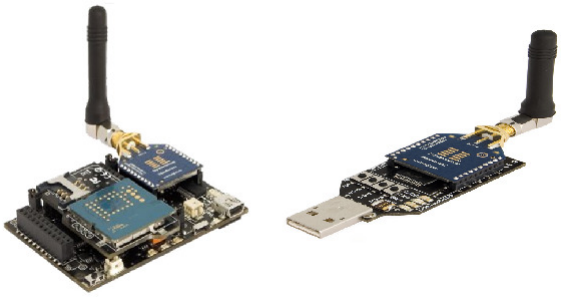

Figure C. 5. Waspmote

The general characteristics of Waspmote are:

- Weight 20 gr.
- It has the possibility to store values permanently in a 2GB SD card.
- Dimensions 73.5 x 51 x 13 mm. These dimensions are smaller than V-Link®.
- The consumption during the running is $9mA$. It has the possibility of an hibernate mode that consumes $0.7\mu A$.
- Waspmote can communicate with other external devices through the using different input/output ports, digitals, analogical and USB.
- The battery included with Waspmote is a Lithium-ion battery (Li-Ion) with 3.7V nominal voltage. Solar panels up to 12V are allowed. The maximum charging current through the solar panel is 240mA.

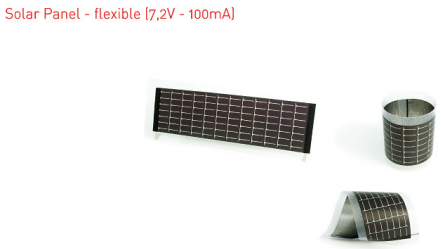

Figure C. 6. Solar panel

- There are sensors connected to Wapmote, a temperature sensor, acceleration sensor. The Waspmote design is aimed at easing integration of both input (sensors) and output (actuators) wich allow expansion of the already wide range of mote responses.

Waspmote is joined with a sensor board. This sensor board has been generated by the team of the project. This board has different functions like to switch on, to turn off the sensors, the fitting-out of the signal and to digitalize the signal.

The sensor board is connected to the strain gauges and to Waspmote, it transmits the strains of the tackle. Strain gauges can be connected to the sensor board by means of two different ways. One way is a full bridge connection and the other way is two half bridges, those have less sensibility that the full bridge.

Waspmote receives the data of the sensor board and it can generate three types of response: storage of collected data (on SD card), wireless transmission of data (using a radiofrequency signal through the XBee module or through the mobile communications network using the GRPS module) or automatic activation through an actuator directly controlled by the microprocessor's output signals or through a switch or relay.

The module used at this project has been XBee module. The XBee modules integrated in Waspmote include RPSMA antenna connectors. These modules connect the sensor reading with the software of the PC. The software to interpret the Waspmote information has been developed by Compass Ingeniería y Sistemas[25] using Libelium libraries.

[25] Compass Ingeniería y Sistemas is a consulting services company specialized in the engineering design, as well as in the development of software for calculation and information management in technology.

References

Andrei N. A scaled nonlinear conjugate gradient algorithm for unconstrained optimization. Optimization, 2008. Vol. 57(4). pp. 549-570.

Antman S.S. Nonlinear problems of elasticity. Springer-Verlag, 1995.

Arcaro V.F. A simple procedure for analysis of cable network structures [http://www.arcaro.org/tension/main.hm]. UNICAMP/FEC, 2004(b).

Arcaro V.F. A simple procedure for shape finding and analysis of fabric structures [http://www.arcaro.org/tension/main.htm]. UNICAMP/FEC, 2004(a).

Arcaro Vinicius F. http://www.arcaro.org/tension/index.htm 2010/2011.

Barnes M. Form finding and analysis of tension structures by dynamic relaxation. International Journal of Space Structures, 1999. Vol. 14. pp.89-105.

Bower Allan http://solidmechanics.org 2010/2011.

Ciortan C. and Guedes Soares, C. Computational study of sail performance in upwind Condition. Ocean Engineering, 2007. Vol. 34. pp. 2198-2206.

Codeluppi R., Golfarelli, A., Rossetti, A., Pholi, Talamelli, A. and Tartagui, M. A sensor network for real-time windsail aerodynamic control. 52nd International Symposium Electronics in Marine. 2010.

Collie S.J., Gerritsen, M. and Jackson, P. A Review of Turbulence Modelling for Use in Sail Flow Analysis. Auckland, New Zealand : School of Engineering Report nº 603, 2001.

Cook R.D., Malkus, D.S., Plesha, M.E. and Witt, R.J. Concepts and applications of finite element analysis. Wisconsin : John Wiley & Sons, 2002. ISBN 0-471-35605-0.

Cook Robert D. Finite Element Modeling for Stress Analysis. New York : John Wiley & Sons, 1995. ISBN: 0-471-107743.

Couser P. Computational methods for investigating sail forces - a case study. Proceedings of Yacht Vision. Auckland, New Zealand . 1998.

Couser P. Prediction of aerodynamic sail forces for upwind yacht velocity prediction programs. Proceedings of the 1st Australian Sailing Science Conference, Tasmania, Australia. 1998.

DeJarnette F.R. Arrangement of Vortex Lattice on Subsonic Wings. Vortex Lattice Workshop. NASA SP, 1976. Vol. 405.

Fiddes S.P. and Gaydon, J.H. A new vortex lattice method for calculating the flow past yacht sails. Journal of Wind Engineerin and industrial Aerodynamics. 1996. Vol. 63. pp. 35-60.

Flay R. Special Issue on Sail Aerodynamics. Journal of Wind Engineering and Industrial Aerodynamics, 1997. Vol. 63.

Fukasawa T., Katori, M. Numerical approach to aeroelastic response of three-dimensional flexible sails. 11th Chesapeakes Sailing Yacht Symposium. 1993.

García J. and Oñate E. An Unstructured Finite Element Solver for Ship Hyddrodynamics Problems. Journal of Applied Mechanics, 2003. Vol. 70 (1). pp. 18-26.

García J., Valls A. and Oñate E. ODDLS: A new unstructured mesh finite element method for the analysis of the free surface problems. International Journal for Numerical Methods in Engineering, 2008. Vol. 76(9). pp. 1297-1327.

Gentry A.E. A Review of Modern Sail Theory. Proceedings of the 11th AIAA Symposium on Sailing. Seattle, Washington. 1981.

Gentry A.E. The Aerodynamics of Sail Interaction. Proceedings of the Third AIAA Symposium on the Aero/Hydronautics of Sailing. Redondo Beach, California. 1971.

Gentry A.E. The Application of Computational Fluid Dynamics to Sails. Proceedings of the Symposium on Hydrodynamic Performance Enhancement for Marine Aplication. Newport, Rhode Island, 1988.

GIDhome http://gid.cimne.upc.es.

Gill P.E. and Murray, W. Newton type methods for unconstrained and linearly constrained optimization. Mathematical Programming, 1974. Vol. 7. pp. 311-350.

Graf K., Renzsch, H. RANSE Investigation of Downwind Sails and Interaction into Sailing Yacht Design Processes. 2nd High Performance Yacht Design Conference. Auckland, 2006.

Greeley D.S, Kirkman, K.L., Drew, A.L. and Cross-Wither, J. Scientific sail shape design. Proc. SNAME 9th Chesapeake Sailing Yacht Symposium. Annapolis, Maryland. 1989.

Grennhalgh S. Curtiss H. C., Smith B. Aerodynamic Properties of a Two-Dimensional Inextensible Flexible Airfoil. AIAAJ, 1984. Vol. 22. pp. 865-876.

Hazen G.S. A model of sail aerodynamic for diverse rig types. Proceedings of New England Sailing Yacht Symposium. 1980.

Hedges K.L. Computer Modelling of Downwind Sails. New Zealand : ME Thesis, University of Auckland, 1993.

Hedges K.L., Richards, P.J. and Mallison, G.D. Computer modelling of downwind sails. Journal of Wind Engineering and Industrial Aerodynamics, 1996. Vol.63. pp. 95-110.

Hess J.L. and Friedman, D.M. An Improved High-Order Panel Method for Three-Dimensional Lifting Flow. NADC-79277-60 : Douglas Aircraft Co., 1981.

Hess J.L. and Smith, M.O. Calculation of nonlifting potential flow about arbitrary three-dimensional bodies. Journal of Ship Research, September 1964. pp. 22-45.

Hess J.L. Calculation of potential flow about arbitrary three-dimensional lifting bodies. Long Beach, California : Final Techanical Report MDC J5679-01, McDonnell Douglas, 1972.

Hess J.L. The problem of three-dimensional lifting potential flow and its solution by means of singularity distribution. Computer Methods in Applied Mechanics and Engineering, 1974. Vol. 4. pp. 283-319.

Hess J.L., and Smith, A.M.O. Calculations of Non-Lifting Potential flow About Arbitrary Three dimensional Bodies. Journal of Ship Research, 1964. Vol. 8. pp. 22-64.

Hirsch C. Numerical Computation of Internal and External flows. Wiley, 1988. Vol. 1.

Hirsch C. Numerical Computation of Internal and External Flows. Wiley, 1990. Vol. 2.

Hough G.R. Remarks on vortex-lattice methods. Journal Aircraft, 1973. Vol. 10. pp. 314-317.

Jackson P.S. A simple Model of Elastic Two-Dimensionals Sails. AAIAJ, 1983. Vol.21. pp. 153-155.

Jackson P.S. and Christie, G.W. Numerical analysis of three-dimensional elastic membrane wings. AIAA Journal, 1987. Vol. 25(5). pp. 676-682.

Jackson P.S. and Fiddes, S.P. A new view of the vortex lattice method. Bristol : University of Bristol. Department of Aerospace Engineering, 1995. Report No. 724.

Jackson P.S. and Fiddes, S.P. Two-dimensional viscous flow past flexible sail sections close to ideal incidence. Aeronautical Journal, 1995. Vol. 99. pp. 217-225.

Jackson P.S. Modelling the aerodynamics of upwind sails. Journal of Wind Engineering and Industrial Aerodynamics, 1996. Vol. 63. pp. 17-34.

Jackson P.S. The Analysis of Three-Domensional Sails. University of Western Ontario : Proc. CANCAM, 1985.

Jackson S P The analysis of three-dimensional sails. Proceedings of the 10th Canadian Congress of Applied Mechanics. Ontario : Technical Report. University of Western Ontario, 1985.

James R.M. On the remarkable accuracy of the vortex lattice method. Computational Methods Appl. Mech. Eng., 1972. Vol. 1. pp. 59-79.

Johnson F.T. A General Panel Method for the Analysis and Design of Arbitrary Configurations in Incompressible Flows. Seattle, Washington : NASA, Scientific and Technical Information Office, 1980.

Jones R.T. and Cohen, D. High speed wing theory. Princeton University Press : Princeton Aeronautical Paperback, 1960.

Katz J. and Plotkin A. Low-Speed Aerodynamics. New York : Cambridge University Press, 2006.

Kerwin J.E. A Velocity Prediction Program for ocean racing yachts. MIT Irving Pratt Ocean Race Handicapping Project, 1978.

Kerwin J.E., Kinnas, S.A., Lee, Jin-Tae and Shih, Wei-Zen A surface Panel Method for the Hydrodynamic Analysis of ducted propellers. SNAME Transactions. 1987. Vol. 95.

Krebber B., Hockirch, K. Numerical Investigation on the effects of trim for a yacht rig 2nd High Performance Yacht Design Conference. Auckland, 2006.

Lainè Robert http://www.sailcut.com/Sailcut_CAD, 2010.

Lamb H. Hydrodynamics. Cambridge : Cambridge Engineery University Press., 1932.

Lan C.E. A quasi-vortex-lattice method in thin wing theory. Journal Aircraft, 1974. Vol. 11. pp. 518-527.

Lock R. C. and Williams, B.R. Viscous-inviscid interactions in external aerodynamics. Progress in Aerospace Science, 1987. Vol. 24. pp. 51-171.

Lopez R. Flood 2 User's Guide. CIMNE, 2008-2010. www.cimne.com/flood.

Luenberger david G. Linear and nonlinear programming. Addison-Wesley, 1984. ISBN 0-201-15794-2.

Marchaj C.A. Sail Performance. techniques to Maximise Sail Power. Adlard Coles Nautical, 2003. ISBN 0-7136-6407-X.

Marchaj C.A. The aerodynamic characteristics of a 2/5th scale Finn sail and its efficiency when sailing to windward. Advisory Committe for Yacht Reserach Report, 1969.

Masuyama Y. Tahara, Y., Fukasawa, T., Maeda, N. Database of Sail Shape vs- Sail Performance and Validation of Numerical Calculation for Upwind Condition. Proceedings of the 18th Chesapeake Sailing Yacht Symposium. Annapolis, Maryland, 2007.

MicroStrain http://www.microstrain.com/v-link.aspx.

MicroStrain. Little Sensors, Big Ideas Web of the company MicroStrain. 2009-2011. http://www.microstrain.com.

Milgram J.H. Effects of mast on the aerodynamics of sail sections. Marine Technology , 1978. Vol. 15(1). pp. 35-42.

Milgram J.H. The aerodynamics of sails. Proceedings of the Seventh Symposium of Naval Hydrodynamic. 1968. pp. 1397-1434.

Milgram J.H. The analytical design of yacht sails. Trans. Society of Naval Architects and Marine Engineers. 1968. VOl. 76. pp. 118-160.

Miyata H. and Lee Y.W. Application of CFD simulation to the design of sails. Journal of Marine Science and Technology, 1999. VOl. 4. pp. 163-172.

Murayama H., Kageyama, K., Nasure, H., Shimada, A. and Uzawa, K. Application of Fiber-Optic Distributed Sensors to Health Monitoring for full-scale composite structures. Journal of Intelligent Material System and Structures, 2003. Vol. 14.

Muttin F. Structural and analysis of sails. European Journal of Mechanics, A/Solids, 1991. Vol. 10 (5). pp. 517-534.

Nielsen J.N. Theory of Flexible Aerodynamic Surfaces. ASME, J. Appl. Mech., 1963. Vol. 30. pp. 435-442.

Nocedal J. and Wright, S.J. Numerical optimization. Springer-Verlag, 1999.

Oñate E., Garcia, J., Idelshon, R.I. and Del Pin, F. FIC formulations for finite element analysis of incompressible flows Eulerian ALE and Lagrangian approaches. Computational Methods in Applied Mechanics and Engineering, 2006. Vol. 195. pp. 3001-3037.

Oñate E., Valls, A. and García, J. Modeling incompressible flows at low and high Reynolds numbers via a finite calculus-finite element approach. Journal of Computational Physics, 2007. Vol. 224. pp. 332-351.

Oñate E. Introduction to the finite element method fos structural analysis. Linear static. Barcelona : Springer and CIMNE, 2009. Vol. 1.

ORACLE Web http://www.oracle.com/us/corporate/newsletter/database-insider/apr-10-bmw-184175.html.

Ortigosa I. and Garcia, J. A calculation/simulation system of sails communicated in real time with wireless sensors. MARINE 2009. Trondheim, Norway, 2009(a). ISBN 978-84-96736-66-5.

Ortigosa I. and Garcia, J. Prediction of total resistance coefficients using neural networks. Journal of Maritime Research, 2009(b). Vol. 6 (3).

Ortigosa I., López, R. and Garcia, J. A Neural Networks approach to residuary resistance of sailing yacht prediction. Computational Methods in Marine Engineering II. - Barcelona, 2007. ISBN: 978-84-96736-19-1.

Pauletti R.M, Mariani Guninardi, D. and Camilo Deifeld, T.E. Argyris Natural Membrane Finite Element Revisited. Barcelona : STRUCTURAL MEMBRANES CIMNE, 2005.

Querard A.B.G., Wilson, P.A. Aerodynamic of Modern Square Head Sails: a Comparative Study Between Wind-Tunnel Experiments and Rans Simulations Proceedings of the Modern Yacht. Southampton, UK , 2007.

Rangogni R. amd Reali, M. The coupling of the finite difference method and the boundary element method. Applied Mathematical Modelling, 1982. Vol. 6. pp. 233-236.

Renzsch H., Müller, O. and Graft, K. FlexSail: A fluid-structure interaction program for the investigation of spinnakers. Proc. Intl. Conference on Innovetions in High Performance Sailing Yachts. Lorient (France), 2008.

Richter H.J., Horrigan, K.C. and Braun, J.B Computational Fluid Dynamics for Downwind Sails. Proceedings of the 16th Chesapeake Sailing Yacht Symposium. Annapolis, 2003.

Rossetti A., Codeluppi, R., Golfarelli, A., Zagnoni, M., Talamelli, A. and Tartagni, M. Design and characterization of polymeric pressure sensors for wireless wind sail monitoring. Sensors ans Actuators A, 2011. Vol. 167. pp. 162-170.

Schlichting Hermann Boundary Layer Theory . 1979.

Schoop H. Structural and aerodynamic theory for sails. European Journal of Mechanics, A/Solids, 1990. Vol. 9 (1) . pp. 37-52.

Schoop H., Bessert, N. Instationary aeroelastic computation of yacht sails International Journal for numerical methods inengineering, 2001. Vol. 52. pp. 728-803.

Sriram Jameson, A. and Gerritsen, M.G. Numerical Analysis and Design of Upwind Sails. 21st AIAA Applied Aerodynamics Conference. Orlando : AIAA, 2003.

Taylor R.L. Finite Element Analysis of membrane Structures. Berkeley : Department of Civil and Enviromental Engineering. University of California, 2001.

Thwaites B. The Aerodynamic Theory of Sails, I. Two Dimensional Sails. Proc. R. Soc., 1961. VOl. 261. pp. 402-422.

Timoshenko S.P and Woinowsky-Krieger, S. Theory of Plates and Shells. McGraw-Hill, 1959.

Trower Gordon Sails & Rigging. London : Helmsman Books, 1996. ISBN 1 85223 853 4.

Viola I.M. Numerical and Experimental Flow Dynamics applied to Sailing Yacht Dynamic. Milan : Ph.D. Thesis, Politecnico di Milano, 2008(b).

Viola I.M., Ponzini, R., Rocchi, D. and Fossati, F. Analysis of Aerodynamic Indices for Racing Sailing Yachts: a Computational Study and Benchmark on up to 128 CPU's Lecture Notes in Computational Science and Engineering,1, Parallel Computational Fluid Dynamics, 2008(a). Vol. 74 (2). pp. 61-70.

Waspmote http://www.libelium.com/products/waspmote.

Weber J. The calculation of the pressure distribution on thick wings of small aspect ratio at zero lift in subsonic flow. London : Rep. Mem. Aero. Res. Coun. Lond., 1954. Vol. 2993.

Wikipedia http://en.wikipedia.org/wiki/Sailing.

Woodward F.A. Analysis and design of wing-body combinations at subsonic and supersonic speeds. Journal of Aircraft, 1968. Vol. 5.

Yoo J. and Kim, H.T. Computational and experimental study on performance of sail of a sailing yacht. Ocean Engineering, 2006(a). Vol. 33. pp. 1322-1342.

Yoo J., Kim, J., Park, I. Ahn, H. and Van, S- CFD C on the Sail Like Three Dimensional Airfoilslation. Proceedings of the Second High Performance Yacht Design Conference. Auckland, New Zealand , 2006(b).

Zienkiewicz O.C. El método de los elementos finitos. Barcelona : Reverte, 1982.

Zienkiewicz O.C. The finite element method in engineering Science. Mc Graw Hill, 1977.